The effects of dynamic ship deflections on friction in monopile seafastening systems

Investigating friction as a method for longitudinal seafastening of monopiles subjected to ship-induced loads and loss of contact

MSc Thesis

Saskia Walgaard

TU Delft

ROLL GROUP

Thesis for the degree of MSc in Marine Technology in the specialisation of Ship and Offshore Structures

The effects of dynamic ship deflections on friction in monopile seafastening systems

Investigating friction as a method for longitudinal seafastening of monopiles subjected to ship-induced loads and loss of contact

by

Saskia Walgaard

at

Roll Group

This thesis (**MT.24/25.022.M**) is classified as confidential in accordance with the general conditions for projects performed by the TU Delft.

08-01-2025

Company supervisors	
Responsible supervisor:	Thomas Nierop
Daily supervisors:	Thomas Nierop, Patrick van der Slot
Thesis exam committee	
Chair/Responsible professor:	Dr. Apostolos Grammatikopoulos
Staff member:	Christof van Zijl
Staff member:	Dr. Alessandro Cabboi
Company member:	Thomas Nierop
Company member:	Patrick van der Slot
Author details	
Author:	Saskia Walgaard
Studynumber:	5655560
Cover:	Internal image Roll Group
Style:	TU Delft Report Style, with modifications by Daan Zwaneveld
Electronic version:	`http://repository.tudelft.nl/`

Preface

Dear reader,

This thesis on ”The effect of friction on monopile seafastening systems during ship motions” finalizes the master *Marine Technology* at Delft University of Technology. The research was conducted at Roll Group, which takes care of heavy cargo both on land and at sea.

In 2019, during a symposium of my HBO Marine Technology study association, I listened to Patrick van der Slot, who talked about all aspects of heavy transport within Roll Group. From that moment, my interest was piqued. I started my third-year internship within Roll Group and started working there as a job student. Over the years, I had a glimpse behind the scenes, and my interest in heavy transport continued to grow. After completing my bachelor’s degree, I decided to continue my studies at TU Delft while continuing to work at Roll Group with great enthusiasm.

In my master’s, I specialized in ’Ship and Offshore Structures,’ so I knew I wanted to do something with this specialization, preferably in combination with heavy transport. This was realised when Thomas and Patrick offered me a graduation topic related to my master’s track and heavy transport. I want to thank Thomas and Patrick for this opportunity and their supervision. Especially Thomas, who was always willing to help me, and I want to thank him for the feedback he provided during the whole process. Besides them, I would like to thank my other colleagues from engineering, with whom I had a lot of fun every day and who supported me during my graduation process.

I want to continue by expressing my gratitude to my supervisors from the TU Delft: Christof van Zijl, Apostolos Grammatikopoulos, and Alessandro Cabboi. Thanks to Christof, who was always available for questions or discussions, and Apostolos for helping me focus on the right direction within my research and for all the other help they both provided me. I also want to thank Alessandro for his help and expertise in the tests I executed and for the feedback he provided me.

Finally, I want to thank my family and friends for all the support during my studies and thesis. In particular, I would like to thank my parents, who always supported me, showed interest in my studies, and stood behind my choices, as well as Jeroen for reading this whole report and providing me with valuable feedback.

Saskia Walgaard
Capelle aan den IJssel, December 2024

Summary

The offshore wind market is expanding rapidly due to the growing demand for offshore wind energy. This drives the development of larger, more advanced wind turbines and increases the diameter of monopiles. Transporting these massive monopiles presents challenges, particularly in ensuring secure seafastening. Traditional seafastening systems rely on mechanical support to prevent motion, such as saddles for the transverse direction and lashing wires for the longitudinal direction. With the increasing weight of monopiles, these solutions are becoming increasingly impractical, heavy and costly.

During monopile transportation, waves cause the vessel to move and deflect, with the saddles moving accordingly. The monopile, which has separate stiffness properties, experiences different deflections and displacements. Due to these different deflections and displacements, the vertical forces exerted by the monopile on the individual saddles are not distributed equally. In the least favourable conditions, this can result in loss of contact, also called intermittent contact. Longitudinal vessel accelerations generate forces in the monopile's longitudinal direction, where friction between the monopile and saddles opposes these forces. However, as friction depends on the contact pressure, any reduction of the vertical force, and so the contact force, affects the friction force.

Seafastening arrangements are designed according to DNV-ST-N001 Marine Operations and Marine Warranty standards. Seafastening requirements are based on seafastening design loads calculated for each shipment and cargo item. DNV-ST-N001 set a minimum seafastening capacity based on cargo weight, not considering friction. The latest update (December 2023) allows cargo transport without seafastening if the friction capacity is at least twice the seafastening design loads. Otherwise, seafastening capacity defaults to a weight-based function, creating a gap between the minimum seafastening capacity and calculated seafastening design loads.

Roll Group's current seafastening designs do not incorporate friction to prevent longitudinal motion, leading to conservative seafastening systems with high equipment- and installation costs. Therefore, there is growing interest within Roll Group in whether accounting for friction between the monopile and the saddles could reduce the required seafastening arrangement, potentially leading to more efficient and cost-effective designs. This knowledge gap leads to the following research question:

"How does friction between a monopile and its saddles affect the seafastening arrangement of a monopile?"

This research aims to determine the friction resistance between the monopile and the saddles when the vessel is exposed to waves, including cases with intermittent contact of the saddles. Based on this information, the seafastening arrangement can be defined when friction is included in the seafastening calculations.

For this research, a coupled fluid-ship model from another research is revised and used to calculate the forces between the saddles and the monopile. This calculation is based on the vertical displacements of the vessel and monopile for all wave heights that can occur during monopile transport. As a result, the loss-of-contact cases were defined. Since this coupled fluid-ship model only focuses on the vertical displacements of the monopile, a longitudinal monopile model is developed. The longitudinal monopile model focuses on the relative horizontal displacement of the monopile caused by heave and pitch motions. This model is a mass-spring system where the monopile represents the mass, behaving as a rigid body to prevent axial vibrations.

An in-depth analysis of the longitudinal monopile model is done for a case excluding friction and a case including friction. The analysis of the longitudinal displacement of the monopile with lashing wires, but without considering friction, resulted in a seafastening arrangement consisting of sixteen lashing wires to prevent all longitudinal motions of the monopile for all wave heights. When friction is considered, the analysis shows that the total friction capacity remains sufficient for all wave heights to prevent the longitudinal motion of the monopile without applying lashing wires.

In this research case, the total friction capacity of the saddles is at least twice the design loads during the whole wave cycle for all wave heights. Based on this, DNV can agree that meeting only the minimum seafastening capacity requirements is acceptable. The last step of executing a friction-based seafastened monopile transport is getting permission from the marine warranty surveyor and the captain.

Contents

Nomenclature

Abbreviations

Abbreviation	Definition
FloFlo	Float on - Float off
GHS	General HydroStatics
LoLo	Lift on - Lift off
MWS	Marine Warranty Surveyor
RoRo	Roll on - Roll off

Symbols

Symbol	Definition	Unit
A	Area	[m^2]
a_x	Acceleration in x-direction	[m/s^2]
E	Young's modulus	[GPa]
F	Force	[N]
F_k	Kinetic friction force	[N]
F_N	Normal force	[N]
F_s	Static friction force	[N]
G	Shear modulus	[Pa]
H_s	Wave height	[m]
h	Height	[m]
I	Moment of inertia	[m^4]
K_e	Stiffness element matrix	[N/m]
k_s	Stiffness	[N/m]
k	Wave number	[-]
L_e	Element length	[m]
M_e	Mass element matrix	[kg]
P	Contact pressure	[N/mm^2]
t	Time	[s]
u	Vertical deflection	[mm]
v	Vertical direction	[-]
γ_{xy}	Shear strain	[m/m]
Δx	Transverse displacement	[m]
δ_s	Shear correction factor	[-]
ζ_a	Wave amplitude	[m]
θ	Rotation	[deg]
λ	Wavelength	[m]
μ	Friction coefficient	[-]
μ_k	Kinetic friction coefficient	[-]
μ_s	Static friction coefficient	[-]
ρ	Density	[kg/m^3]
τ_{xy}	Shear stress	[N/m^2]
ω	Angular frequency	[rad/s]

Definitions

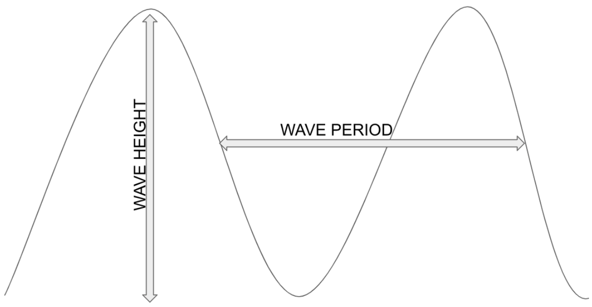

Figure 1: Definition of wave height and period [1]

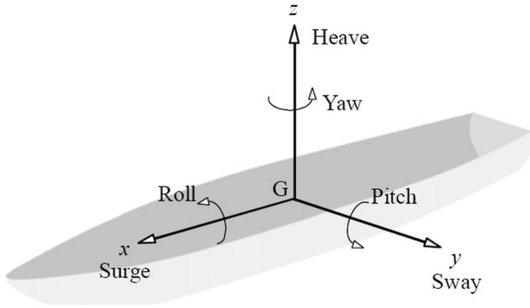

Figure 2: Definition of six degrees of freedom [2]

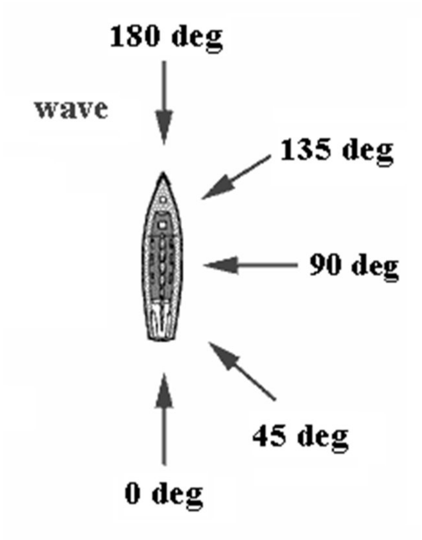

Figure 3: Definition of heading [3]

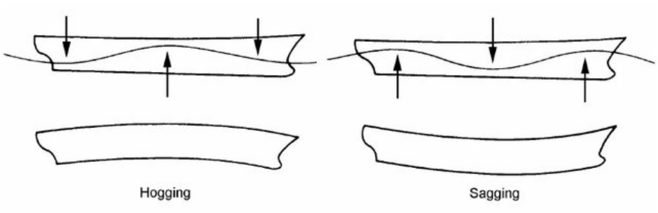

Figure 4: Definition of hogging and sagging [4]

1 Introduction

This research is on behalf of Roll Group. Roll Group takes care of heavy cargo both on land and at sea. Roll Group owns a fleet of unique, highly adaptable vessels to transport heavy cargo. The fleet contains semi-submersible multifunctional dock-type vessels and wide deck carriers, offering three different loading methods – RoRo, LoLo, FloFlo – to serve a wide range of markets, including the offshore wind market.

The offshore wind market continues to grow as the demand for offshore wind energy increases, both as a replacement and as an addition to other energy sources. The growth in offshore wind energy production has accelerated the development of larger and more advanced wind turbines. Over 380 GW of offshore wind capacity is predicted to be added in the next ten years [5]. Larger wind turbines are developed to keep pace with the need for increased offshore wind energy capacity. The diameter of monopiles, the foundation of offshore wind turbines, has increased over the past few years from an average of 5 meters to 10 to 12 meters [6].

The transportation of these large monopiles poses significant challenges. One of the critical aspects of safely transporting these massive structures is ensuring they are securely fastened to the transport vessel. This process, known as seafastening, involves designing systems that can withstand the dynamic forces experienced at sea. Traditionally, seafastening designs for monopiles focus on ensuring a high capacity to resist movement through mechanical means. Saddles are used to support and prevent the motion of the monopile in the transverse direction, and lashing wires are used to prevent relative longitudinal motion [7, 8]. However, due to increasing weights of the monopiles, this often results in overly heavy and costly systems [9].

In the current seafastening designs of Roll Group, friction is not considered to prevent longitudinal motion. There is growing interest in whether accounting for friction between the monopile and the saddles could reduce the required seafastening arrangement, potentially leading to more efficient and cost-effective designs. This research focuses on monopiles as cargo transported by MC-class vessels. Figure 1.1 shows an example of a project in which Roll Group transported monopiles.

Figure 1.1: Monopiles transported by MC-class vessel
(Please note, the colour of this vessel is now blue, as shown on the cover picture)

1.1. Problem definition

While transporting a monopile, the vessel is subjected to waves. These waves cause the vessel to move and deflect. Because the saddles are connected to the vessel, they move with the vessel's deflections. Moreover, the monopile isn't rigidly connected to the vessel; it has separate stiffness properties, resulting in deflections and displacements different from those of the vessel and connected saddles. Due to the different deflections and displacements along the vessel's length, the vertical forces exerted by the monopile on the individual saddles are not distributed equally. In the least favourable conditions, this can result in loss of contact.

Longitudinal vessel acceleration generates forces in the monopile's longitudinal direction. When these forces are applied, the friction remains static as long as there is no relative displacement of the monopile. However, once relative motion occurs in the longitudinal (x) direction, the static friction transitions to kinetic friction between the monopile and its saddles. The existing friction opposes the longitudinal forces caused by the vessel's longitudinal accelerations. Since friction depends on the contact pressure, any reduction of the vertical force, and so the contact force, affects the friction force in the saddles.

The amount of seafastening is determined by the seafastening design loads, which depend on the route, time of shipment and loading conditions. These seafastening design loads are calculated for each shipment and each cargo item onboard. Rules of DNV-ST-N001 [10] give a minimum seafastening capacity as a function of the cargo weight without considering friction. This research investigates whether the required seafastening capacity can be reduced by accounting for friction. A new rule is defined in the latest version (December 2023) of DNV, which allows cargo transport without seafastening if the friction capacity is at least twice the seafastening design loads. However, when the friction capacity is less than twice the design loads, the minimum seafastening capacity is determined by the function based on the cargo weight, which does not consider friction. This means a big disparity exists between the required seafastening capacity depending on the method of seafastening.

Furthermore, the effect of intermittent contact on the total friction capacity is still an ongoing research topic. This uncertainty is relevant when the goal is to reduce seafastening, as varying friction resistance during intermittent contact could impact the design. Next to that unknown, the influence of alternating friction capacities during hogging and sagging is not known. It might be that a sagging wave results in a different total friction capacity compared to a hogging wave.

The research topic *"The effects of dynamic ship deflections on friction in monopile seafastening systems"* addresses this innovative approach by investigating how the combination of friction and intermittent contact can influence the seafastening arrangement. Specifically, it aims to determine if the frictional forces can be used as seafastening, even when the forces exerted by the cargo are unequally distributed or locally intermittent. This results from exposure to forces caused by vessel motions due to waves. When frictional forces can be used for seafastening, it can reduce the need for excessive seafastening capacity.

Relevance & Significance

This research holds extensive relevance in marine transportation and offshore wind energy. As the demand for offshore wind farms continues to develop, so does the need for efficient and cost-effective transportation solutions for monopiles [11, 12]. By investigating the effect of friction and intermittent contact in seafastening, this research could improve seafastening systems by optimising them and making them more economically beneficial. This would reduce the cost of transportation and the amount of materials, making the operation more efficient and sustainable.

Furthermore, the findings from this study could be applied to improve existing seafastening designs for monopiles and other cargo that experiences friction during transport. The potential reduction in material and production costs associated with less over-engineered seafastening arrangements could make offshore wind energy projects more financially viable for Roll Group. This emphasises the need for a thorough understanding of the effects of friction behaviour between monopile and saddles in both constant and intermittent contact situations to apply the suited amount of seafastening.

1.2. Research question

The problem definition can be translated into the following research question:

How does friction between a monopile and its saddles affect the seafastening arrangement of a monopile?

Multiple sub-questions are proposed to answer the main research question systematically. These sub-questions must be answered before the main question can be answered.

1. **Modelling**:
   How can a system of a monopile exposed to longitudinal forces caused by ship motions be modelled to define the effect of friction as seafastening?
2. **Friction**:
   How does the varying contact pressure due to the vessel's deflection affect the friction between the monopile and its saddles?
3. **Number of saddles**:
   How does a varying number of saddles affect the friction capacity?
4. **Practical application**:
   How would the seafastening system be changed in Roll Group's previous monopile transportation projects if friction was considered?

1.3. Objective & scope

The main objective follows from the research question. It is defined as creating a model of the monopile on its saddles, including friction, to determine the friction resistance of the saddles when the vessel is exposed to waves, including instances where intermittent contact occurs in the saddles. The cases where intermittent contact occurs and the forces on the saddles are gathered with the coupled fluid-ship model of [13].

Intermittent contact becomes essential when more than two saddles are used. Losing contact in one saddle can lead to higher pressures in the other saddles, resulting in varying friction resistance. The behaviour of the friction coefficient during varying contact pressures will be determined using experimental data. The case with the lowest friction resistance leads to the determination of the seafastening arrangement.

In this research, it is assumed that:

- The saddle is rigidly connected to the deck of the vessel, so it is assumed that the connection between the deck and saddle is preserved, i.e. the structural integrity of the connection remains.
- The vessel and saddles are not moving as one system. The saddles' stiffness differs from the vessel's, so the saddles can deflect between the monopile and the deck. However, it is assumed that the deflection of the saddles does not influence the friction capacity.
- There is no friction in the transverse (y) direction since the monopile is constrained in the saddle in the transverse direction.
- The lashing wires exert a vertical force on the outer ends of the monopile, which can create an initial moment on the monopile. It is assumed that this bending moment in the monopile is negligible. Furthermore, it is assumed that this vertical force does not contribute to the friction resistance.
- Displacement of the monopile caused by the vertical deflection is neglected.

The research is focused on deep water since DNV states that cargo needs seafastening for at least 0.1g, independent of the wave states, so deep water is the governing case. Besides that, with the deep water condition, all data from the research of [13] can be used as input since deep water is assumed in this research.

Furthermore, quasi-static vessel motions as a result of hogging and sagging are considered in this research. Vibrations affecting the monopile are not considered in this research since the encounter frequency of the waves (0.6 rad/s) is much lower than the first axial natural frequency of the monopile (8.3 rad/s). The result of a lower wave encounter frequency than the first natural frequency of the monopile is that resonance does not occur, reducing the likelihood of significant axial vibrations, which can affect friction. Meanwhile, the frequency of quasi-static vessel motions is lower since the wave period is longer, which can influence friction and intermittent contact.

1.4. Thesis outline

First, a concise overview of the literature review on friction theory is provided in chapter 2. This condensed version highlights only the aspects directly relevant to the research discussed. Chapter 3 first gives the case description on which this research is based, and the model description is given in the second section. The coupled fluid-ship model is described, and the adjustments to this model are highlighted. Next, the longitudinal monopile model is described, which is used to determine the longitudinal motions of the monopile due to ship motions. Sliding friction tests are performed to investigate the relation between the contact pressure and the friction coefficient, and details of these tests are given in chapter 4. The results in chapter 5 consist of the results of the adjustments of the coupled fluid-ship model, the friction coefficient function as a result of the tests and the static and dynamic analyses of the longitudinal motion done with the longitudinal monopile model. Chapter 6 gives the conclusions of this research, and chapter 7 provides a discussion and recommendations.

2 Theory of friction

This chapter summarizes the literature review regarding the theory of friction. The first chapter describes Coulomb's friction model used in this research. The next section describes the fundamentals of Coulomb's friction law and examines static and kinetic friction and the stick-slip phenomenon. The friction force depends on the friction coefficient, so more information is provided about the coefficient of friction. The last section of this chapter covers some factors affecting friction.

2.1. Friction models

Several researchers have studied friction over the centuries. It started with Leonardi Da Vinci's first friction model, which Guillaume Amontons and Charles-Augustion de Coulomb extended. Later, Philip Bowden, David Tabor, Dahl, and LuGrue extended the friction model. The most well-known and widely used model is the Coulomb friction law.

2.1.1. Coulomb's law of friction

Coulomb's law of friction is the Amontons-Coulomb model since Coulomb adds to Amonton's second law of friction; "strength due to friction is proportional to compressive force, although for large bodies friction does not follow exactly this law" [14]. Coulomb also observed that friction is independent of velocity. The following observations on friction were made:

- Friction is proportional to the compressive force
- Friction is independent of the apparent contact area
- Friction is independent of velocity

Based on these observations, equation 2.1 is obtained by Amontons and Coulomb and they formulated the Amontons-Coulomb friction model which is given in equation 2.2 and figure 2.1. The Coulomb friction model is the easiest and most well-known friction model. Though it greatly oversimplifies the frictional phenomena, it is widely used when dynamic effects are unconcerned. The Coulomb friction force is a force of constant magnitude, acting in the direction opposite to motion [15].

$$F_f = \mu F_N \tag{2.1}$$

$$F_f = \begin{cases} \mu_k F_N, & \text{if } v_r < 0 \\ [-\mu_s F_N, \mu_s F_N], & \text{if } v_r = 0 \\ -\mu_k F_N, & \text{if } v_r > 0 \end{cases} \tag{2.2}$$

Where F_N is the force pressing surfaces together and μ is the frictional factor.

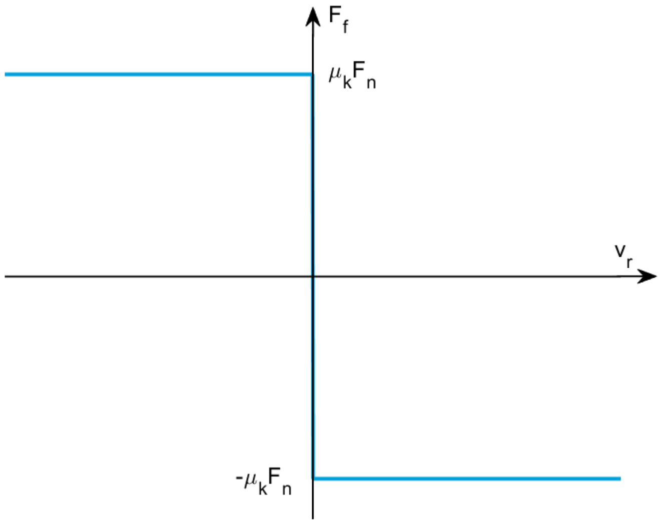

Figure 2.1: Friction force according to Amontons-Coulomb model

One of the biggest problems of the Coulomb model is, that it cannot handle the environment of zero velocity [15].

2.2. Fundamentals of Coulomb's friction law

Friction force restricts the relative motion between the surfaces of two bodies applied by a tangential force (see figure 2.2). Friction is defined as the resisting force tangential to the common boundary between the two bodies when, under the action of an external force, one body moves, or tends to move, relative to the surface of the other [16]. Or shortly defined as the tangential reaction force between two surfaces in contact [17].

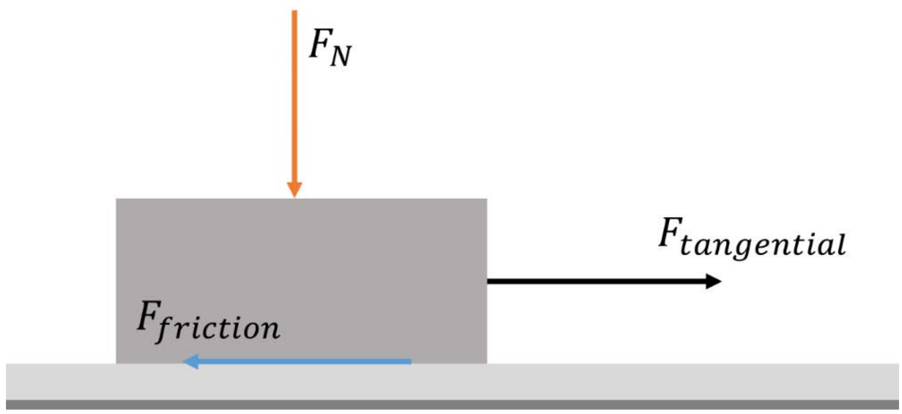

Figure 2.2: Forces acting on a friction interface [9]

Friction can be static or kinetic. It is static when the object is not moving, tending to start moving, or when the object is moving with a pure rolling motion without slip. It is kinetic if the object moves, which is a sliding motion, or when it moves with a pure rolling motion with slip.

2.2.1. Static friction

Static friction is the frictional force that acts between two surfaces at rest relative to each other. It prevents the surfaces from starting to move. Static friction increases with the applied tangential force until it reaches the static friction limit; see figure 2.3.

This static friction limit depends on time, the normal force, and the properties of the surfaces in contact, such as material type, surface roughness, hardness, temperature, etc. The time-dependent increase in static friction is due to the microscopic changes at the contact points over time rather than the macroscopic nature of the surfaces in contact [18]. In addition, the limit can change drastically depending on the loading conditions. For example, fast and rapid impacts like wave motions or vibrations can change the static friction limit [19, 20]. Once the static friction limit is exceeded, the object starts to move, and static friction transitions to kinetic friction [21, 22, 23].

2.2.2. Kinetic friction

Kinetic friction is the frictional force that acts between two surfaces in motion relative to each other. It opposes the direction of motion and tries to slow down or stop the moving object. Kinetic friction remains constant regardless of the speed of the moving surfaces as long as the nature of the surfaces and the normal force remains unchanged. The force of kinetic friction (F_k) is given by $F_k = \mu_k F_N$, where μ_k is the coefficient of kinetic friction, and F_N is the normal force. Kinetic friction does not change with the applied tangential force and is generally lower than static friction due to a lower coefficient of friction. It acts continuously while the objects are in relative motion [22, 23, 21]. The kinetic friction regime is shown in figure 2.3.

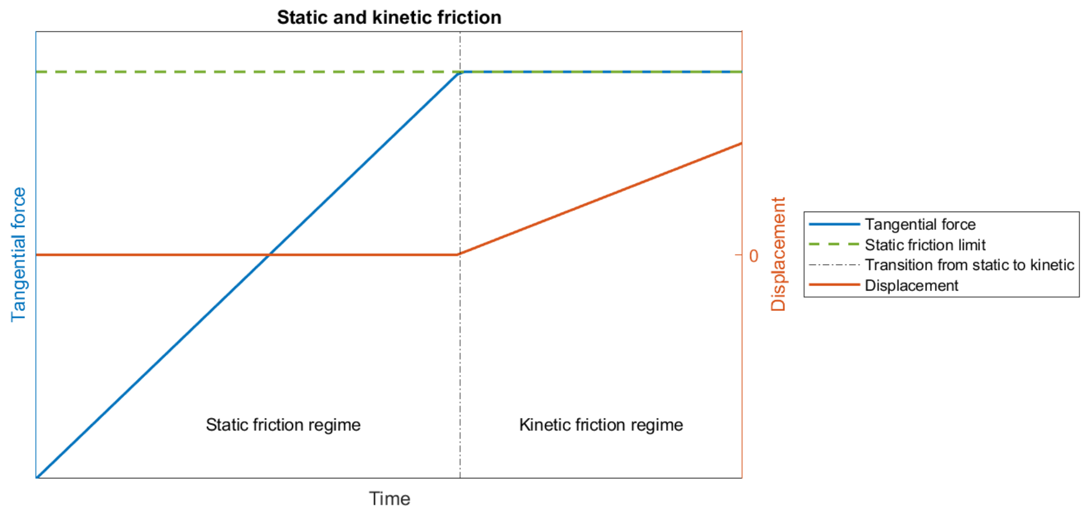

Figure 2.3: Tangential force and displacement against time for the static and kinetic friction regime

Conclusion types of friction on the monopile

Static friction acts before the relative movement starts, preventing the surfaces from starting to move, while kinetic friction acts once two surfaces are in motion relative to each other. Static friction can vary and potentially exceed the magnitude of the tangential kinetic force, which is generally constant and lower than the maximum static friction force. Static friction depends on multiple factors, like the applied tangential force and the properties of the surfaces in contact, but it can also change over time or due to loading conditions. Kinetic friction acts continuously while the objects are in relative motion and is independent of the velocity of the moving objects.

From the findings of this research, which are elaborated on in the next chapters, it can be concluded that for the specific case investigated, static friction governs seafastening and transporting monopiles since Roll Group aims to have a zero relative displacement of the monopile during transport.

2.2.3. Stick slip behaviour

The stick and slip regions during friction refer to two distinct phases in the stick-slip phenomenon:

Stick Region

- In the stick region, the two surfaces remain in contact due to static friction forces holding them in place.
- For rigid bodies, there is no relative motion between the surfaces during this phase.
- The static friction force increases as the applied tangential force increases until it reaches a maximum value called the static friction limit.

It can be concluded that the stick region corresponds to static friction. Pure stick does not occur for elastic surfaces if a tangential force is present.

Slip Region

- Once the applied force exceeds the static friction limit, the surfaces suddenly become unstuck and start sliding relative to each other.
- This rapid sliding motion is called the slip region for rigid bodies.
- During the slip, the friction force can drop to a lower value called the kinetic friction force. Whether or not the friction force is reduced depends on the combination of the materials and their properties.
- The surfaces continue sliding with this kinetic friction until the applied force decreases enough for them to stick again, restarting the cycle.

The friction in the slip region corresponds with the kinetic friction regime. The slip region of elastic surfaces is different from that of rigid bodies since there is a smooth transition region between partial stick, micro-slip, and pure sliding for elastic surfaces. In addition, the stick region involves no relative motion and increasing static friction, while the slip region involves rapid sliding motion and lower kinetic friction [24, 25]. A repeating process of the increasing and decreasing tangential force where the motion starts and stops can be considered repetitive stick-slip motion.

Conclusion stick-slip of the monopile
The friction of the monopile can occur in the stick or slip region depending on the magnitude of the tangential force on the monopile in the longitudinal direction. There is no relative displacement during static friction, so the friction acts in the stick region. The slip region is reached when the tangential force exceeds the static friction limit because the friction becomes kinetic, resulting in a longitudinal motion.

2.3. Friction coefficient

Two types of friction coefficients can be distinguished: one that represents the friction opposing the onset of relative motion, called the static friction coefficient, and one that represents the friction opposing the continuance of relative motion once that motion has started, called the kinetic friction coefficient. In the case of solid-on-solid friction (with or without lubricants), these two types of friction coefficients are conventionally defined as follows:

$$\mu_s = \frac{F_s}{F_N} \tag{2.3}$$

$$\mu_k = \frac{F_k}{F_N} \tag{2.4}$$

F_s is the force sufficient to prevent the relative motion between two bodies, and the static friction coefficient increases until the static friction limit is reached. F_k is the minimum force needed to maintain relative motion once the static friction limit is exceeded. F_N is the force normal to the interface between the sliding bodies. Both μ_s and μ_k are material- and system-dependent [26].

Rubber is used as support material in the current saddle design of Roll Group. Table 2.1 gives the friction coefficients between steel and the support materials used by Roll Group, according to [10].

	Dry	Wet
Rubber	0.3	0.3
Steel	0.1	0.0
Wood	0.3	0.2

Table 2.1: Friction coefficients for rubber, steel and wood against steel in dry and wet conditions [10]

It should be noted that the friction surfaces are free from oil or other lubricating fluids when applying these friction coefficients given by [10].

2.4. Factors affecting friction

There are multiple factors that affect the friction of the monopile seafastening, which can be divided into three categories as shown in figure 2.4 [9]:

1. Support pad factors: material properties and roughness of the support pad
2. Counter material factors: monopile roughness, coating type and coating thickness
3. Environmental, operational and loading factors: applied pressure, lubrication, rate of loading, temperature and consolidation time.

This section focuses on the material properties of the support pad, the normal force, coating and lubrication.

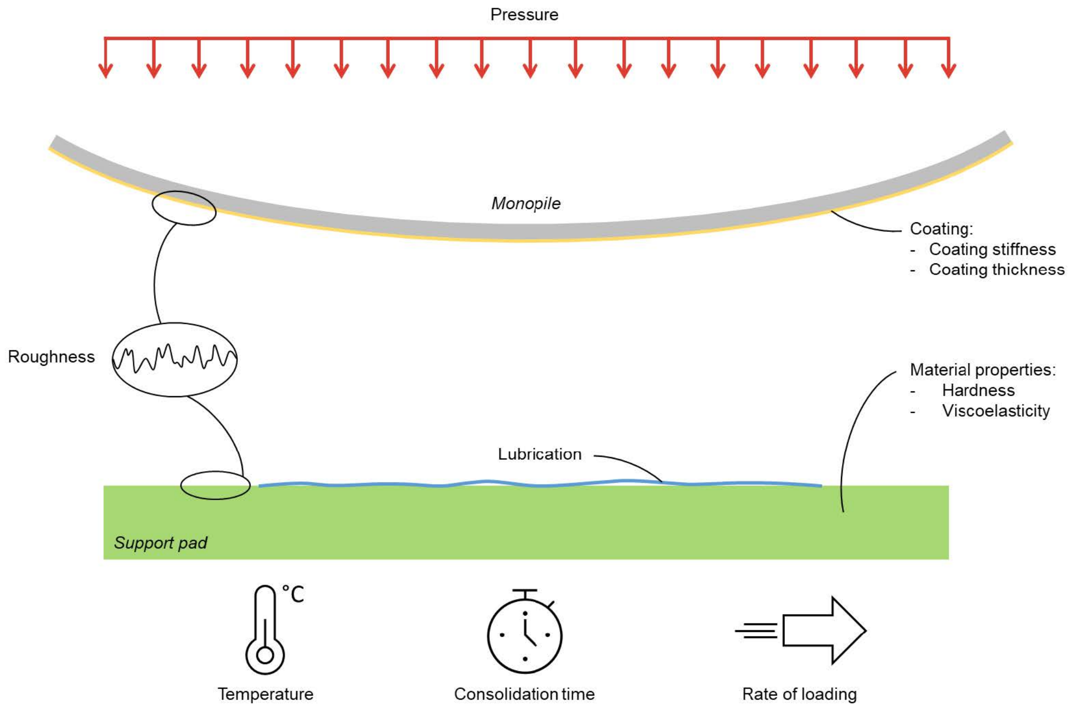

Figure 2.4: Overview of factors that affect friction in monopile sea fastening [9]

2.4.1. Material properties of support pads

Rubbers, polymers, and wood are often used as supporting materials and friction interfaces. Multiple sources investigate the hardness and viscoelasticity of the supporting materials to determine their effect on frictional behaviour.

Hardness

Hardness is a solid's resistance to local (plastic) deformation. The hardness of polymers is often expressed in °*Shore A* and °*Shore D*.

Polymers can exhibit a non-linear relationship between friction and hardness. The static friction coefficient in polymers is strongly influenced by their elastic characteristics, including modulus of elasticity, tensile strength, and yield strength. A polymer with a lower modulus of elasticity tends to have larger relative deformations, leading to a larger actual contact area. Since the friction depends on the pressure, a larger actual contact area potentially results in higher static friction forces. More details about the influence of the pressure on the friction are given in the next paragraph. Due to its structure and elastic properties, the polymer tends to surround the roughness of the metal surface in polymer-metal contact systems. This behaviour differs from metal-metal contact systems and affects the friction characteristics.

For polymers, the relationship between the static friction coefficient and hardness involves complex interactions between hardness, elasticity, surface properties, and material composition. The friction behaviour of polymers is highly dependent on their specific mechanical properties and can vary significantly between different types of polymers [27, 28, 29].

Viscoelasticity
The overall friction coefficient, μ, can be divided into the contributions of adhesive (μ_{adh}) and viscoelastic hysteresis (μ_{hyst}). The viscoelastic hysteresis does depend on the material properties and geometry, meaning that the viscoelasticity of rubber causes variations in the depth, size and geometry of the contact area, resulting in variation of μ_{hyst} [30].

Temperature significantly affects the viscoelastic properties of materials. As temperature increases, the molecular mobility within the material also increases, leading to changes in its mechanical behaviour. An increased temperature generally leads to a decrease in material stiffness and an increase in its ability to deform. A decreased temperature results in increased stiffness and reduced molecular mobility, making the material more elastic and less viscous.

The frictional properties of viscoelastic materials are highly dependent on temperature. This is because friction in these materials is influenced by their stiffness and ability to deform under load. The material becomes softer and more compliant at higher temperatures, increasing the contact area. A larger contact area results in a lower contact pressure and so in a higher friction coefficient (see next paragraph). However, the exact effect can vary depending on the specific material and conditions. The material becomes stiffer and less compliant at lower temperatures, potentially reducing the contact area and friction [31, 32].

2.4.2. Applied force and pressure

Contrary to Amontons' law, which states that the friction coefficient is independent of the apparent contact area, studies have shown that the friction coefficient can change with varying pressure. Depending on the factors affecting friction, the friction coefficient can decrease for an increasing contact pressure until it levels out for higher contact pressures [33, 34]. A theoretical relation between friction coefficient and normal pressure is shown in figure 2.5.

The normal force is relevant to monopile seafastening. The pressure on the friction interface is caused by the weight of the monopile, the area of the supports, and vessel motions. Due to vessel motions and accelerations, the pressure on the interface can increase or decrease, and such a varying contact force can result in a changing friction coefficient. The vessel motions should thus be considered when determining the friction resistance.

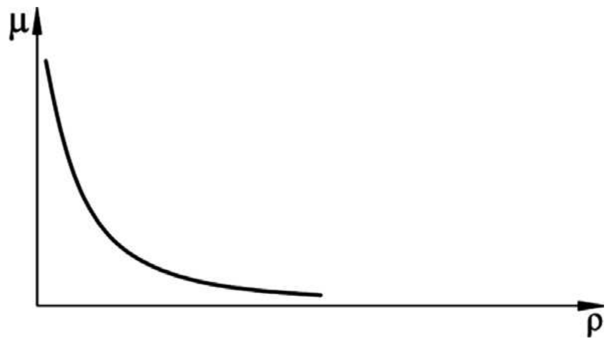

Figure 2.5: Friction coefficient versus contact pressure [33]

2.4.3. Monopile coating

The coating is applied on monopiles to prevent degradation due to environmental conditions. NEN-EN-ISO 12944 prescribes different coating thicknesses for different locations on the monopile. The part in the splash zone needs the most protection since this part is periodically exposed to salt water and oxygen. This often results in a thicker coating layer. The coating thickness, type, and roughness along the monopile can differ. The coating is one of the factors affecting monopile seafastening friction [9].

A study by [35] is done on the tribological behaviour of polymer composite coatings. This study showed some relation between shear strength and friction. Higher coefficients of friction were observed for higher shear-strength coatings. An epoxy coating showed high friction and a low wear rate. Lower friction and more wear were observed for PU coatings. The study states that the performance of the coatings also depends on temperature, load, and velocity.

The effect of coating thickness differs for different support materials. The impact of varying coating thicknesses is minimal for a rougher support material. Increasing coating thickness for a less rough support material increases friction resistance. The difference in effect between two different support materials is caused by the different hardness, roughness or manufacturing processes. The study of B. Schrijvers [9] shows that coating thickness affects friction, but other factors might nullify this effect.

2.4.4. Lubrication

Lubrication has an explicit effect on friction. Compared to dry situations, the friction resistance decreases when lubrication is applied. In wet conditions, thin water films might separate the support material and the rigid solid surface in the contact region, resulting in a smaller real contact area. After forming the thin water film, the adhesion friction component would be reduced due to the important decline of the solid-solid contact area [30].

In rougher surfaces, the lubrication might be in deeper cavities. This will not lead to the separation of the asperities of both surfaces. The friction resistance depends more on the viscous resistance of the fluid than on the material properties [36]. Applying lubrication on the friction interface will reduce the coefficient of friction, which is caused by the reduction in real contact area. The reduction of the coefficient of friction depends on the amount and type of lubrication.

In monopile seafastening, lubricants are not applied on purpose since this would decrease friction resistance. However, seawater and rain are potential fluids that might be present between both surfaces. The environmental conditions can cause this before loading the monopile on the seafastening (due to rain) or by environmental conditions during operations (splashing). The amount of water between the surfaces is hard to quantify, so the only distinction is between dry and wet [9].

2.5. Conclusion on literature review

The fundamentals of friction describe Coulomb's law of friction with static and kinetic friction. Static friction is the frictional force that acts between two surfaces at rest relative to each other, and kinetic friction is the frictional force that acts between two surfaces when they are in motion relative to each other. From the stick-slip information, it can be concluded that the stick region corresponds to static friction, and the slip region corresponds to kinetic/sliding friction. The friction coefficients according to DNV [10] are given. Last, some factors that can affect friction are described. The factors considered are the material properties of the support pads, applied force, monopile coating, and lubrication. The effect of an increasing contact pressure on the friction resistance will be investigated further in this research.

3 Case and model description

The first section of this chapter describes the load case used in this research, consisting of a description of the vessel, cargo, and seafastening. Next, the model description is divided into two parts: the coupled fluid-ship model of [13] and the monopile longitudinal model. For the coupled fluid-ship model, the original model, output and the adjustments made to the model are described. Different types of mass-spring systems are given for the longitudinal monopile model, which are used when setting up the monopile model.

3.1. Case description

This section describes the vessel, cargo, and seafastening of the case considered for this research. These elements are used throughout this research, making the research specific for the used vessel, monopile and seafastening arrangement.

3.1.1. Vessel description

Roll Group operates with a fleet of ten vessels comprised of five semi-submersible dock vessels and five wide deck carriers. The dock vessels are commonly not used to transport monopiles since the decks are not large enough for the length of the monopiles nowadays. Two wide deck carriers of the fleet are part of the MC-class, and these vessels transported monopiles in the past. This research will focus on the vessels of this MC-class. Parameters of the MC-class vessels are given in table 3.1.

Figure 3.1: BigRoll Bering [37]

Parameter		Value	Unit
Length overall	L_{oa}	173	m
Length between perpendiculars	L_{pp}	162.80	m
Breadth	B	42	m
Depth	D	12	m
Draught	T	6.5	m
Deadweight	DWT	$\pm$ 20157	mt
Displacement	∇	$\pm$32958	m^3

Table 3.1: Main particulars MC-class vessels 'BigRoll Bering' & 'BigRoll Beaufort' [38]

3.1.2. Cargo description

The parameters of the monopiles considered in this research are given in table 3.2. Four monopiles are transported in one voyage, so the total mass of four monopiles is considered in the voyage analysis to calculate the deflections and accelerations. Only one monopile is considered to determine the impact of friction on the seafastening arrangement. The results can be applied to all monopiles. For this case, it is assumed that the monopile does not contain a coating at the saddle locations.

Parameter		Value	Unit
Length	L_m	74	m
Diameter	D_m	8	m
Thickness	t_m	80	mm
Moment of inertia	I_m	15.6	m^4
Young's Modulus	E_m	200	GPa [39]
Weight monopile	W_m	11.3	MN
	W_m	1151	mt

Table 3.2: Structural parameters monopile of the considered case [13]

3.1.3. Seafastening description

Seafastening systems for heavy cargo are used to constrain the cargo to the vessel to prevent the cargo from moving. The seafastening system can be seen as the boundary condition between the coupled ship-cargo system. This makes the cargo become part of the vessel with the same accelerations as the vessel.

Figure 3.2 shows a schematic overview of the monopile and seafastening system applied during a previous monopile transportation project of Roll Group. In figure 3.2, it can be observed that the monopile is tapered at one side, meaning the diameter starts decreasing. This research neglects this effect; the monopile is considered to be a cylinder.

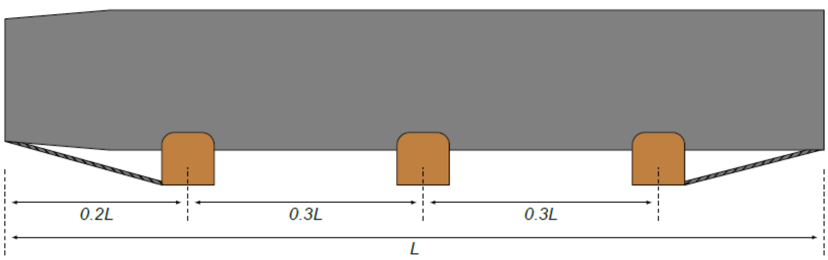

Figure 3.2: Schematic overview seafastening system applied at monopiles [13]

For the seafastening of the monopile, lashing wires and saddles are used, shown in figure 3.2 and 3.3. This research focuses on the contact pressure in the saddles caused by waves for 3 to 7 saddles. The schematic overviews of all saddle configurations are given in Appendix A.

Saddles

The saddles carry the weight of the monopile and prevent movement in the transverse direction. The number of saddles depends on the weight of the monopile and the deck strength. Saddles are designed to suit the properties of the monopile and strong points on the deck. This means that for each new monopile design, a saddle is tailor-made. Figure 3.3a show monopile saddles.

Lashing wires

The seafastening in the longitudinal direction for monopiles can consist of lashings only or of a combination of lashing wires at one side and stoppers at the other. Both configurations prevent movement in the longitudinal direction. The lashing wire can be modelled as a unilateral spring, which allows tension but cannot sustain compression forces [13]. Figure 3.3b shows an outer end of a monopile with lashing wires.

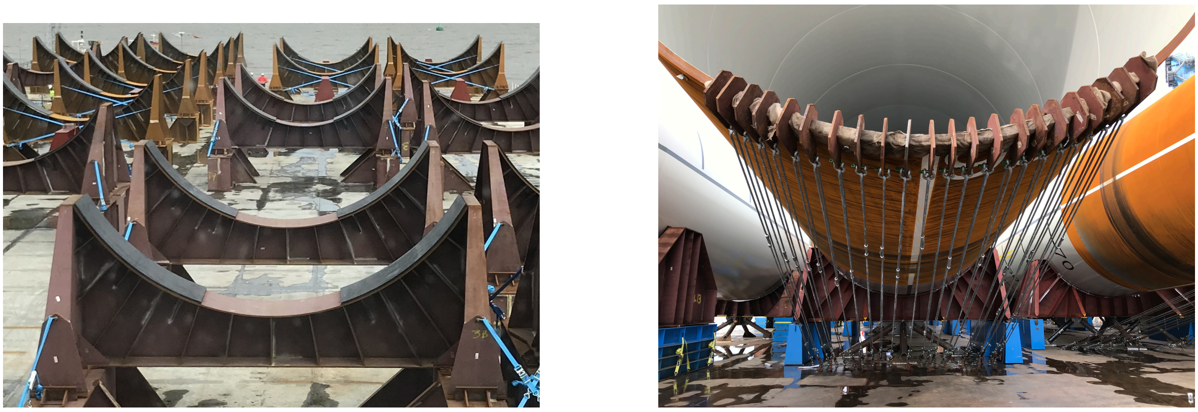

(a) Saddles **(b)** Lashing wires

Figure 3.3: Seafastening system elements [37]

The lashing wires are applied at both ends of the monopile, all in an inward direction. Since the lashings are unilateral springs, only one set is working simultaneously. Due to this effect, it is possible to consider only one side when analysing the number of lashing wires since the same results apply to the other side. The lashing wires all have a capacity of 10 metric tons and are applied with a pre-tension of 1-2 mT, but these forces are counteracting. Therefore, these pre-tension forces are neglected in the analysis.

3.2. Model description

This section describes the two models of this research. The first model is a revised version of the coupled fluid-ship model as input model, made by [13]. The input, set-up and output of this model are given. Next, adjustments are made to this coupled fluid-ship model related to the ballast condition and the dynamic deflection. The revised model calculates the contact forces between the saddles and monopiles for wave heights between 1.0 and 7.0 meters with a wavelength resulting in the maximum vertical displacement. From this, the intermittent contact cases are defined. The output of the revised coupled fluid-ship model is used as input for the second model, called the longitudinal monopile model. This monopile model is specified as a mass-spring system. The main objective of this model is to determine the seafastening arrangement required to prevent the longitudinal displacement of a monopile when friction is included in the seafastening calculations. Figure 3.4 shows a flow diagram of the models described in this section. Figure 3.5 shows a monopile with normal forces as a result of the vessel's deflection and friction forces as a result of the external longitudinal force. The normal forces are the output of the revised coupled fluid-ship model, indicated with the green arrows, and the output of the longitudinal friction model is the friction force, shown with blue arrows.

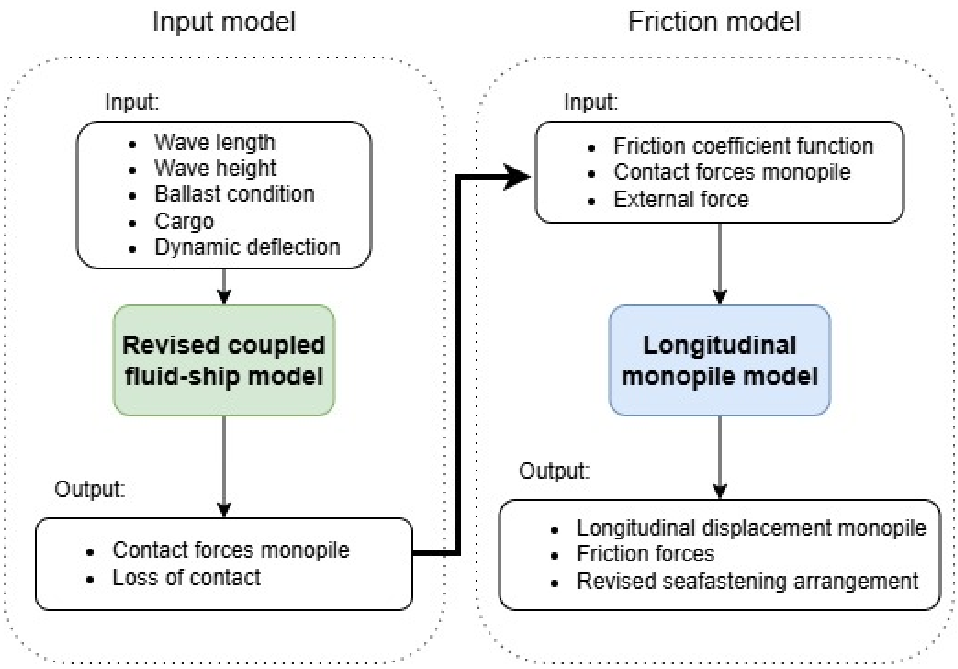

Figure 3.4: Flow diagram of coupled fluid-ship and longitudinal monopile model

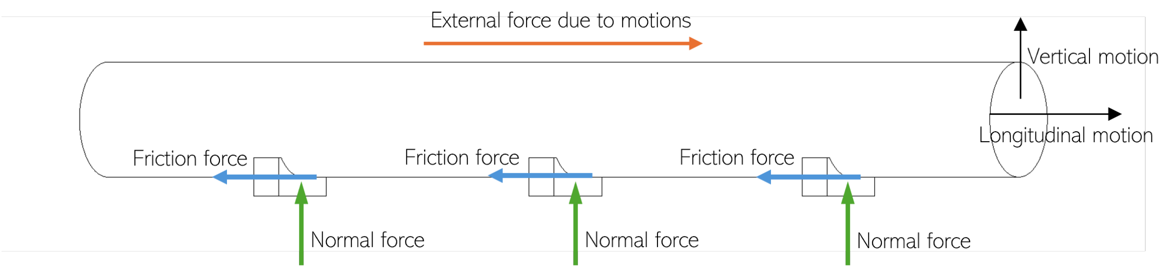

Figure 3.5

3.2.1. Coupled fluid-ship model

A numerical coupled fluid-ship model of [13] is used to find the forces between the saddles and the monopile, the bending moment of the monopile and the magnitude of intermittent contact between the saddle(s) and the monopile. This model is built as a finite element method to extract displacements in the vertical direction and to find the bending moments. The original model of [13] first calculates the dynamic deflection of the vessel as a result of the wave amplitude ζ_a. As a result of these deflections, the forces and bending moments in the monopile are calculated. The forces are translated to displacements in the vertical direction, so the intermittent contact cases are defined. The original model's details are given in this section's first part.

Adjustments are made to the coupled fluid-ship model of [13] to find more accurate deflection results for all wave heights. The second part of this section describes the adjustments made to the original model. As a result, the new deflections give more accurate forces in the monopile, and the intermittent contact cases are more accurate to reality. These forces will be used in the second model, the model of the monopile, to investigate the friction capacity of the saddles, even with intermittent contact.

Original coupled fluid-ship model

The original model of [13] consists of two sub-models: a structural model and a hydrodynamic model in which the ship represents the connection between the two models. The main objective of the hydrodynamic model was to define a load case based on the vessel's hydrodynamic behaviour and to translate this into loads that could serve as input for the structural model. The structural model is the mathematical representation of the cargo and seafastening system and is created in the linear and non-linear domains.

Input

The hydrodynamic model uses the static and dynamic deflections calculated by the stability software GHS (General HydroStatics). The deflection of the vessel depends on the following parameters:

- Wavelength (λ): the deflections become maximal for a wavelength that equals the ship's length.
- Wave height (H_s): a higher wave height results in higher deflections.
- Ballast condition: the fluid in the tanks can make the vessel deflect.
- Cargo: heavy cargo can result in deflections of the vessel.

Based on the deflections of the vessel, the bending moment is calculated with equation 3.1.

$$\text{Bending moment} = EI\frac{\partial^2 y(x)}{\partial x^2} \tag{3.1}$$

The structural model is based on the fundamentals of the finite element method in combination with Timoshenko beam theory. This allows for the calculation of the dynamic displacements in the vertical direction. Beam theory is applied because the monopiles' length is far greater than their diameter. The finite element matrices consist of Young's modulus (E), shear modulus (G), moment of inertia (I) and the element length (L_e). The element mass matrix is multiplied by the weight per unit length (ρA). Since a Timoshenko beam is modelled, the shear correction factor (δ_s) is also included in the element matrices. Equation 3.2 gives the shear correction factor, element stiffness matrix and element mass matrix, respectively, for two degrees of freedom: the vertical direction (v) and rotation (θ).

$$\begin{gathered}
\delta_s = \frac{6}{5}\frac{12 \cdot EI}{GA \cdot {L_{tot}}^2} \\
K_e = \begin{bmatrix}
\frac{12EI}{(1+\delta_s)L_e^3} & \frac{6EI}{(1+\delta_s)L_e^2} & -\frac{12EI}{(1+\delta_s)L_e^3} & \frac{6EI}{(1+\delta_s)L_e^2} \\
\frac{6EI}{(1+\delta_s)L_e^2} & \frac{(4+\delta_s)EI}{(1+\delta_s)L_e} & -\frac{6EI}{(1+\delta_s)L_e^2} & \frac{(2-\delta_s)EI}{(1+\delta_s)L_e} \\
-\frac{12EI}{(1+\delta_s)L_e^3} & -\frac{6EI}{(1+\delta_s)L_e^2} & \frac{12EI}{(1+\delta_s)L_e^3} & -\frac{6EI}{(1+\delta_s)L_e^2} \\
\frac{6EI}{(1+\delta_s)L_e^2} & \frac{(2-\delta_s)EI}{(1+\delta_s)L_e} & -\frac{6EI}{(1+\delta_s)L_e^2} & \frac{(4+\delta_s)EI}{(1+\delta_s)L_e}
\end{bmatrix} \\
M_e = \frac{\rho A \cdot L_e}{420}\begin{bmatrix}
156 & 22L_e & 54 & -13L_e \\
22L_e & 4L_e^2 & 13L_e & -3L_e^2 \\
54 & 13L_e & 156 & -22L_e \\
-13L_e & -3L_e^2 & -22L_e & 4L_e^2
\end{bmatrix}
\end{gathered} \tag{3.2}$$

The global mass matrix (**M**) is constructed from the mass element matrices (M_e) as shown in figure 3.6. The global stiffness matrix (**K**) is assembled similarly to the global mass matrix but using K_e instead of M_e.

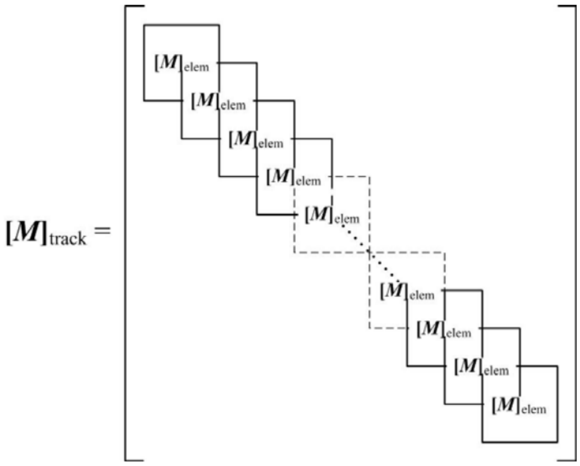

Figure 3.6: The assembly pattern of the global mass matrix [40]

As described in section 3.1, the seafastening system consists of saddles and lashing wires, and both systems act unilaterally, only providing reaction force in compression and tension, respectively. A combination of saddles and lashings are modelled linearly with spring stiffness k_z. In addition, the remaining stiffness of the saddles is modelled as a unilateral spring with stiffness k_s, and the rotational resistance of the lashing wires is modelled as linear rotational springs with stiffness k_θ. Figure 3.7 shows how the seafastening elements are modelled as springs.

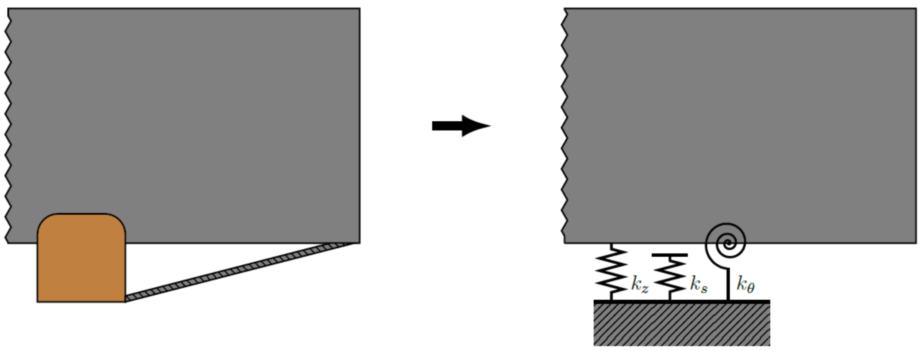

Figure 3.7: Representation of seafastening elements to spring stiffnesses

Output

The original coupled fluid-ship model's output focuses on the structural model since the hydrodynamic output is used as an input for the structural model. The hydrodynamic output is the deflection of the vessel, both static and dynamic. The static deflection is caused by the vessel's weight distribution, including the cargo and the hydrostatic pressure on the hull, called the still water bending moment. The dynamic deflection results from pressure differences caused by the waves, both for in and out-phase waves. The in-phase wave results in sagging, whereas the out-phase wave results in hogging.

The structural output consists of:

- Forces and the bending moment of the monopile
- Forces in the seafastening system
- Loss of contact between the monopile and its saddle(s)

The structural output is given for both the linear and non-linear models. The linear dynamic load case uses a wave amplitude of $\zeta_a = 1\ m$ while the wave amplitude for the non-linear dynamic load case increases to $\zeta_a = 3\ m$. The non-linear dynamic analysis is preferred in dynamic situations with large deflections because non-nonlinearities occur, and the linear approach leads to an overconstrained situation.

Adjustments

Adjustments are made to the hydrodynamic model, resulting in slightly different results in the static output data. The adjustments made are described in this section.

Ballast condition
The stability software GHS defines the ballast condition of the vessel, including the cargo. In this software, the cargo weight distribution is divided over the saddles, which results in a transfer of forces at the saddles' locations into the vessel. The vessel's draft is ballasted to 6.0 m since this is a typical sailing draft for the MC-class vessels. Furthermore, the vessel has no trim or heel angle.

GHS provides the still water deflection of the vessel and the deflection due to waves. The deflection of the vessel is calculated for wave heights ranging from 1.0 and 7.0 meters (ζ_a between 0.5 and 3.5 m). For all wave heights, both the deflection in hogging and sagging conditions are calculated for a wavelength of 169 meters. A wavelength of 169 meters results in the highest deflections during the hogging and sagging cases.

Dynamic deflection
To calculate the dynamic deflections of all wave heights, A. Speksnijder [13] linearised the dynamic deflection of a wave height of 6 meters for all wave heights using equation 3.3.

$$\frac{u_{d,H_s=6m} - u_{sw}}{3} \cdot \zeta_a \tag{3.3}$$

However, an analysis between this linearised deflection and the deflection results of GHS for wave heights from 1.0 to 7.0 meters showed large differences between these two; see appendix B. For this reason, the calculation to linearise the deflections with wave heights is split into three ranges of wave heights:

- Range 1: $0.0m < H_s \leq 2.0m$
- Range 2: $2.0m < H_s \leq 4.5m$
- Range 3: $4.5m < H_s \leq 7.0m$

This resulted in equations equations (3.4) to (3.6).

$$\text{Range 1: } \frac{u_{d,H_s=1m} - u_{sw}}{0.5} \cdot \zeta_a \tag{3.4}$$

$$\text{Range 2: } \frac{u_{d,H_s=4m} - u_{sw}}{2} \cdot \zeta_a \tag{3.5}$$

$$\text{Range 3: } \frac{u_{d,H_s=6m} - u_{sw}}{3} \cdot \zeta_a \tag{3.6}$$

The deflections calculated with these equations show less difference from the deflection calculations of GHS. The differences stay below 7.01%; see appendix B.

Tipping point from linear to non-linear behaviour
With the new equations for the deflection of the vessel, the deflection of the vessel, including the monopiles, can be calculated for wave heights of 1.0 to 7.0 meters. This gives the structural output, consisting of the forces and bending moments of the monopile, forces in the seafastening system and the loss of contact between the monopile and its saddles.

After analysing the forces in the saddles and the loss of contact between the saddles and the monopile for configurations with 3 to 7 saddles, it could be concluded that the tipping point where linear behaviour transitions to non-linear behaviour varies per configuration of saddle numbers. Table 3.3 shows the range of wave heights in which the tipping point from linear to non-linear behaviour is.

No. of saddles:	H_s tipping range [m]
3	6.0 - 7.0
4	3.0 - 4.0
5	2.0 - 3.0
6	1.0 - 2.0
7	<1.0

Table 3.3: Wave height tipping ranges from linear to non-linear behaviour

Contact force and contact pressure

This research focuses mainly on the effect of the contact force between the monopile and its saddles on the friction force. It was decided to focus on the maximum dynamic deflections caused by a hogging wave in arrival ballast condition since this case is considered governing in terms of deflections and forces. More details about the dynamic deflections are given in section 5.1.

The different stiffnesses of the monopile and the vessel result in differences in their deflections, which lead to variations in the load distribution and, consequently, the contact force. Contact is always preserved in all saddles for dynamic cases with linear behaviour. For dynamic cases with non-linear behaviour, contact is lost between the monopile and its saddle(s) after the tipping range. The lost contact pressure is compensated by the saddles which are still in contact. As long as contact is preserved with the saddle, 100% contact area is assumed.

Based on these forces, the contact pressure per saddle is calculated using the contact area of the saddle. To ensure that enough surface area of the monopile is in contact with the saddles, the support material is strategically placed between 30° and 60° on both sides from the centreline, as shown in figure 3.8. The advantages of placing the contact material this way are that it conserves material by avoiding unnecessary placement across the entire saddle, and the structural integrity of the monopile is ensured by preventing local deflections of the monopile. For this specific case, the depth of the contact area is 1.2 meters, so the total contact area of each saddle equals 5.03 m^2; see equation 3.7.

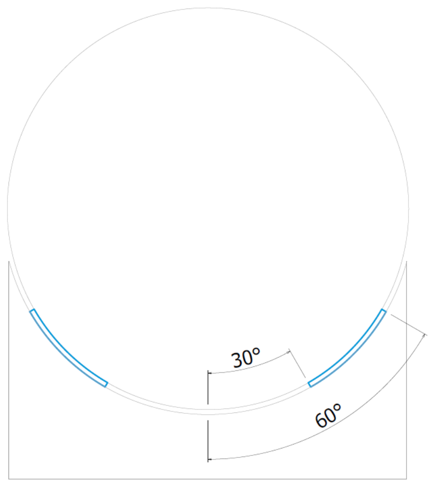

$$\begin{aligned} &\text{Circumference of a circle: } 2\pi \cdot \text{radius} \\ &\text{Circumference of the MP: } 25.1\,\text{m} \\ &\text{Length of 1 support pad: } \tfrac{1}{12} \cdot 25.1 = 2.09\,\text{m} \\ &\text{Total area support pads: } 2 \cdot 2.09 \cdot 1.2 = 5.03\,\text{m}^2 \end{aligned} \tag{3.7}$$

Figure 3.8: Contact area at the saddles

The analysis of the forces in the saddles showed that the sum of the forces in the saddles is less than the static force of 11.3 MN for all saddle configurations. This can be explained by the fact that there is an opposing force of -0.276 MN between the saddles due to gravity according to the results of [13]. So, for the static case with three saddles, the total sum of the forces in the saddles would be 10.47 MN instead of 11.3 MN, and this effect is visible in all configurations. For an increasing number of saddles, the total static force decreases. Table 3.4 shows the total static forces in the saddles per configuration.

No. of saddles:	Opposing force [MN]	Force in saddles [MN]	Deviation [%]
3	$3 \cdot 0.276 = 0.828$	10.47	7.32
4	$4 \cdot 0.276 = 1.104$	10.19	9.77
5	$5 \cdot 0.276 = 1.380$	9.92	12.21
6	$6 \cdot 0.276 = 1.656$	9.64	14.65
7	$7 \cdot 0.276 = 1.932$	9.37	17.10

Table 3.4: Total static force in the saddles per configuration

These results are assumed to be correct for this research phase, even though the total static forces in the saddles for each configuration are expected to remain at 11.3 MN.

Conclusions coupled fluid-ship model

Some adjustments are made to the model of [13] to extract the most realistic forces between the saddles and the monopile. First, a new ballast condition is defined for a draft of 6.0 meters without trim and heel angle. This ballast condition provided the still water bending moment and was the input for the dynamic deflections. The calculation of the dynamic deflections is redefined. Instead of using one linearisation function for all wave heights, three linearisation functions are defined for three ranges of wave heights. This adjustment results in lower differences between the input of the deflections for the research and the deflections calculated by GHS.

The new ballast condition and the more accurate dynamic deflections have defined the tipping point from linear to non-linear behaviour for vertical displacements for three up to seven saddles. Finally, the contact forces and pressures have also changed due to the new ballast condition and dynamic deflections. These contact forces and pressures are the output of the coupled fluid-ship model that will be used as input for the monopile longitudinal model. The contact forces between the saddles and the monopile of the coupled fluid-ship model are assumed to be in phase.

3.2.2. Monopile longitudinal model

A longitudinal numerical model of the monopile is created to find its displacement in the longitudinal direction due to the vessel motions. Initially, the model was set up as a finite element method of a flexible beam model, which will be described in the first section. During the research, this flexible beam model changed into a mass-spring model that behaves as a rigid body. The model's different types of mass-spring systems are described in the second section.

The monopile model is set up such that there is no displacement in the longitudinal direction. This matches the transport conditions of Roll Group. Roll Group calculates the number of lashing wires required to constrain the monopile in the longitudinal direction to prevent longitudinal motion. This calculation does not consider friction forces between the monopile and its saddles. Once the model reaches the steady state for a certain amount of lashing wires, the friction force is considered in the model. This step aims to analyse how the friction force influences the lashing arrangement.

This analysis should first be done for the hydrostatic case, which is the still water bending moment of the vessel. In this case, the pressure in the saddles is evenly distributed because the spacing between the saddles is arranged to be as equal as possible; see appendix A, so each saddle has the same friction capacity. In addition, hydrodynamic cases should be considered for wave heights from 1.0 to 7.0 meters. In these cases, the pressure in the saddle varies, and even loss of contact can occur. This means that the friction capacity fluctuates throughout the wave cycle for different heights, which will be described in the third section. The lashing arrangement can be determined based on the lowest total available friction capacity through the entire wave cycle.

The goal of the longitudinal monopile model is to find the most cost- and material-efficient seafastening arrangement for the monopiles that entirely prevent the longitudinal motion of the monopile throughout the whole wave cycle.

Flexible beam model

First, a flexible beam model was set up to determine the displacement of the monopile for different seafastening configurations. This model was built in the same way as the structural model of [13], so with a global mass matrix **M** and global stiffness matrix **K** as a result of the mass and stiffness element matrices M_e and K_e, respectively. This flexible beam model could not reach a state without axial vibrations, even when a large amount of lashing and friction was applied.

The characteristics of the flexible beam model are attributed to the presence of axial vibrations. Axial vibrations can be induced by impulsive forces, such as wave slamming or resonance. The former is not considered in this research, and the latter is unlikely as the encounter frequency of the waves is much lower than the first natural frequency of the axial vibrations of the monopile. Since this research does not focus on axial vibrations, they were disregarded. Consequently, a rigid body model, which excludes axial vibrations, was deemed more appropriate. For this reason, the model was changed from a flexible beam to a mass-spring system. Although the mass-spring model significantly simplifies reality, it effectively captures the physical phenomena of interest.

Mass-spring model

The mass-spring model aims to find the most time and cost-efficient seafastening system for monopiles considering friction. To reach this goal, the mass-spring model is built in multiple steps, starting with the most basic mass-spring system and extending this until a model is reached that provides results which match the goal. The mass is modelled as a rigid body since no axial vibrations in the longitudinal direction are allowed. This section describes how the accelerations caused by ship motions result in an external force. The six types of mass-spring systems that contribute to the building process of the mass-spring model are listed below. Type 5 is described in detail since it provides results that determine the most time- and cost-efficient seafastening system.

- Type 1: No forces, no motion occurs
- Type 2: External force, motion will occur
- Type 3: External and lashing force, motion will occur
- Type 4: External and lashing force, no motion occurs
- Type 5: External, lashing and friction force, no motion occurs
- Type 6: External, lashing and friction force, motion will occur

Accelerations resulting in external force

The vessel including its cargo is exposed to waves, resulting in vessel motions. The vessel's heave and pitch motions are responsible for the longitudinal motion of the cargo when it is not entirely prevented from motion. The heave and pitch motions exert an external force on the cargo. With the use of Octopus Office, a software based on linear 2D strip theory, the longitudinal accelerations a_x of the vessel, including the cargo, are calculated for wave heights from 1.0 to 7.0 meters at a sailing speed of 12 knots, see table 3.5 and figure 3.9.

The longitudinal acceleration depends on the wave heading and table 3.5 shows maximal accelerations for 30 degrees heading waves. The accelerations in the longitudinal direction for 0 and 30 degrees are plotted for the increasing wave heights, and linear behaviour can be observed. A linear trendline is plotted through the acceleration points of 30 degrees since these are the highest (see figure 3.9), and this trendline is implemented in the longitudinal monopile model to calculate the acceleration that belongs to the wave height. The maximum longitudinal external force as a wave height and time function can be computed using equation 3.8. It should be noted that implementing the trendline of 30 degrees is conservative since the friction in the longitudinal direction is maximum with a heading of 0 degrees, resulting in lower accelerations.

H_s [m]	a_x [g] for heading [deg] 0	30
1.0	0.019	0.019
2.0	0.037	0.038
3.0	0.056	0.057
4.0	0.074	0.076
5.0	0.093	0.095
6.0	0.111	0.114
7.0	0.130	0.133

Table 3.5: Accelerations in the longitudinal direction for 0 and 30 degrees heading

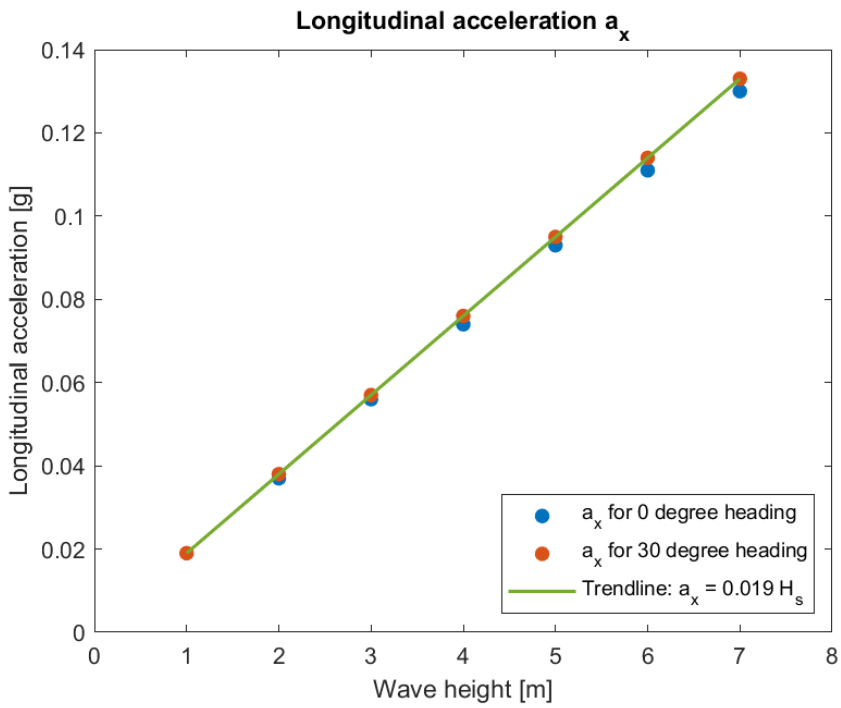

Figure 3.9: Longitudinal acceleration for 12 knots

$$
\begin{aligned}
a_x &= 0.019 \cdot H_s \\
F_{external}(H_s, t) &= M_{MP} \cdot a_x(H_s) \cdot g \cdot \sin(\omega t) \\
\omega &= \sqrt{kg} \\
\text{Wave number: } k &= \frac{2\pi}{\lambda} \\
\text{Wave length: } \lambda &= 169m
\end{aligned}
\tag{3.8}
$$

Type 5: External, lashing and friction force, no motion occurs

Roll Group does not consider friction in the seafastening calculations since DNV-ST-N001 [10] does not allow calculating the required seafastening capacity, including friction. However, there is a friction force between the saddles and the monopile. Once the sum of the friction and lashing forces equals the external force, the monopile is prevented from displacements and accelerations. This type has a force balance, meaning the resulting force is zero. Figure 3.10 shows the mass-spring system for this type, and the equation of motion is given in equation 3.9.

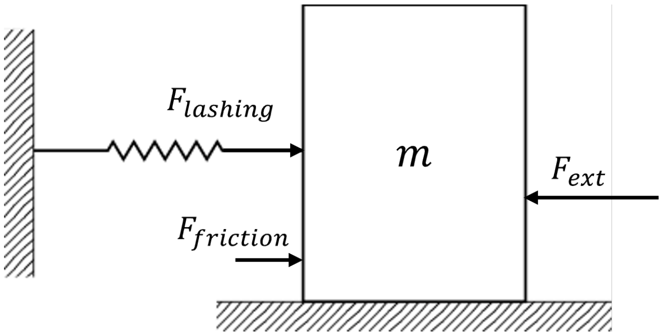

Figure 3.10: Mass-spring system without motion due to a force balance between the external, lashing and friction force

$$\begin{aligned} m\ddot{x} + kx &= F_{external} - F_{friction} \\ \text{Since: } kx &= F_{lashing} \\ m\ddot{x} &= F_{external} - F_{lashing} - F_{friction} \end{aligned} \tag{3.9}$$

The mass-spring system aims to minimize the longitudinal motions, so it is assumed that the inertia term is negligible:

$$m\ddot{x} \approx 0$$

Resulting in the final equation of motion of the mass-spring system of type 5:

$$\begin{aligned} \sum F &= 0 \\ kx &= F_{external} - F_{friction} \\ F_{lashing} &= F_{external} - F_{friction} \end{aligned} \tag{3.10}$$

From equation 3.10, it can be concluded that the amount of available friction capacity determines if lashing wires are required to prevent the longitudinal motion. Once there is sufficient friction capacity, no lashings are needed.

It should be noted that the lashing and friction capacity can be higher than the lashing and friction force. This is shown in three cases in figure 3.11 where the sum of the forces is zero, so no motion will occur. The left battery has precisely enough lashing and friction capacity to get a force balance. The battery in the middle shows a situation with more friction capacity than required to prevent motion, so the friction force is lower than the available friction capacity. In the battery on the right, there is more lashing and friction capacity available than required to prevent motion, so in this situation, only parts of the available capacities are used.

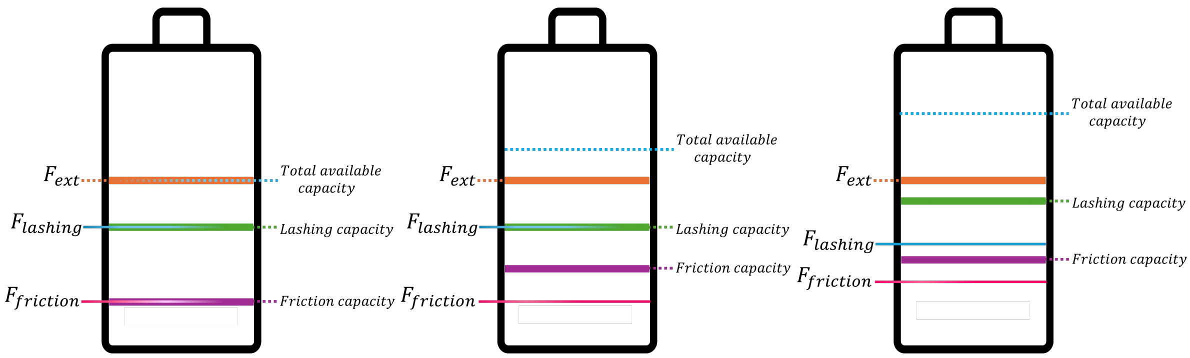

Figure 3.11: 3 Cases with external, lashing and friction forces, all preventing motion

3.2.3. Friction coefficient

In types 5 and 6 of the mass-spring systems, the friction force between the monopile and its saddles is included. In the static case, for example, when the vessel is in the port where there are no waves, the weight of the monopile is divided equally over the saddles, and so is the contact pressure. As a result, the friction force is the same in each saddle.

For dynamic cases, the forces of the revised coupled fluid-ship model of [13] show that the contact forces and contact pressures at the saddles vary over the wave cycle for wave heights from 1.0 to 7.0 meters. A fluctuating contact force leads to varying friction since the normal forces change. Each saddle's friction capacity during the wave cycle depends on the location and the number of saddles. The total friction capacity of the saddles equals the sum of the friction capacity of each saddle. The total friction capacity is used in types 5 and 6 of the mass-spring systems.

It should be noted that the friction force works with the same principle as the lashing force. The friction force opposes the externally applied force and the lashing force. However, cases can occur where more friction capacity is available than required to prevent motion entirely. An example of this can be seen in the middle and right battery of figure 3.11 of type 5. In both cases, more friction capacity is available than is used in the system as $F_{friction}$.

Furthermore, section 2.2 described that the friction of the cargo is static when there is no relative displacement and that the friction is kinetic once the cargo starts to move relative to the saddle. The goal of the seafastening arrangement is to prevent the monopile from relative displacement. The forces opposing the external force work together; when the friction is static, there is no relative displacement, but the lashing wires can already provide a force to prevent displacement caused by the shearing of the material. If the friction becomes kinetic, the force in the lashing wires will increase as they must now resist the relative displacement. Please note that the right battery in figure 3.11 does not correctly show this order since this figure aims to show the principle of the total available capacity. The friction force increases up to the required amount to stop the displacement. If the lashing and friction capacity is insufficient, the monopile will start moving, and no force stops the motion.

Output monopile model

Since the goal of the longitudinal monopile model is to find the most cost- and material-efficient seafastening arrangement for the monopiles that entirely prevents the longitudinal motion of the monopile throughout the whole wave cycle, the model of the monopile should be able to provide the output as described below.

Initially, friction is not considered when performing the same calculations as Roll Group. The model should calculate whether or not the lashing capacity is sufficient to prevent longitudinal motion caused by the external force. This corresponds to the mass-spring system of type 3 or 4, and this analysis should provide the minimum required number of lashing to prevent motion without friction forces entirely.

The same analysis should be done for the next step, but this time, the friction between the monopile and the saddles is included for the static case. This means that the friction force in each saddle is the same. The number of lashing wires is again applied in increasing numbers, corresponding to type 5 or 6. However, this step is only used as a check during the model's building process since the static case won't result in any displacements of the monopile.

As the last step, dynamic cases can replace the static case. The revised coupled fluid-ship model of [13] resulted in normal forces in the saddles, which should be used to calculate the friction capacity per saddle. The results of the friction coefficient tests are included in this part of the longitudinal monopile model. More about the friction coefficient tests will be described in chapter 4. To find the seafastening arrangement that prevents motion through the whole wave cycle, the dynamic case with the lowest friction capacity relative to the external force is selected for this analysis as the governing case. If this case prevents longitudinal motion, other dynamic cases with more friction capacity relative to the external force are also assumed to prevent longitudinal motion. Therefore, only the governing dynamic case is considered, representing the whole wave cycle. The number of lashing wires is again applied with increasing numbers to find the most cost- and material-efficient seafastening arrangement for the monopiles that entirely prevents the longitudinal motion of the monopile during the most extreme dynamic case.

3.3. Conclusions case and model description

For this research, the MC class vessels are considered when transporting four monopiles and seafastening is used to prevent the motion of the monopiles in all directions. The current seafastening arrangement consists of saddles and lashing wires. The longitudinal monopile model is generated to find the displacement of the monopile in the longitudinal direction due to the vessel motions. The initial flexible beam model was unsuitable for this goal since it resulted in axial vibrations. A rigid beam model with a mass-spring system was set up in different steps. The external force on the monopile is applied due to the vessel's heave and pitch motions. The lashing force of the lashing wires is used to prevent this motion. If the lashing force is insufficient to avoid the longitudinal motion entirely, friction forces are also considered part of the longitudinal seafastening arrangement. The application of forces is also considered in the reversed order, so first, friction forces are applied, and lashing forces are considered if the friction capacity is insufficient. Both the lashing and friction forces oppose the external force, and cases can occur where the total capacity of these opposing forces is larger than the required opposing force. In these cases, only the necessary opposing force is applied to the monopile to prevent the longitudinal motion.

The dynamic case with the lowest friction capacity relative to the external force is considered governing and is selected to find the seafastening arrangement that prevents motion. All cases with a higher friction capacity relative to the external force are assumed to prevent motion with the minimum seafastening arrangement of the governing dynamic case. In all dynamic cases, the normal force is different in each saddle, so each saddle has its friction capacity. Using the governing case, the model should provide the most cost- and material-efficient seafastening arrangement for the monopiles that entirely prevents the longitudinal motion of the monopile throughout the whole wave cycle.

4 Sliding friction test

Sliding friction tests are performed in addition to this research. The sliding friction test aims to determine the relation between the contact pressure and the friction coefficient. This is done by increasing normal forces and calculating the friction coefficient with the test data. This chapter consists of the test description and the test results. The results of the tests will be implemented in the numerical monopile model to select the correct friction coefficient for the normal forces in the saddles.

4.1. Test description

This section describes the details of the tests. First, the test method is given, including the way of post-processing the test data. Next, the test set-up is shown, including the limitations of testing. The variation of the normal forces during the tests is described in the next part of this section, followed by the testing parameters. The last paragraph describes the results of the tests.

4.1.1. Test method

The method used for the sliding friction tests is the reciprocating sliding test method. The test material is fixed to the part of the machine that exerts the normal force and does not have a displacement. The normal force is applied as a constant force before the test starts. A specimen of the second material is fixed between the bottom clamps, and this part is displacement-controlled. Once the test begins, the tangential force increases until the static friction limit is reached. From this point, the second material starts to move left and right with a set sliding distance. One cycle is finished when the second material is back at the starting position, meaning zero displacement. The advantage of this method is that all cycles are tested, so the results would show if there is a difference between the beginning and end of the test. The normal force is measured and adjusted during the test through an internal control loop that senses and corrects slight deviations from the normal force. A schematic overview of the reciprocating sliding test method is shown in figure 4.1, and figure 4.2 shows the actual test set-up.

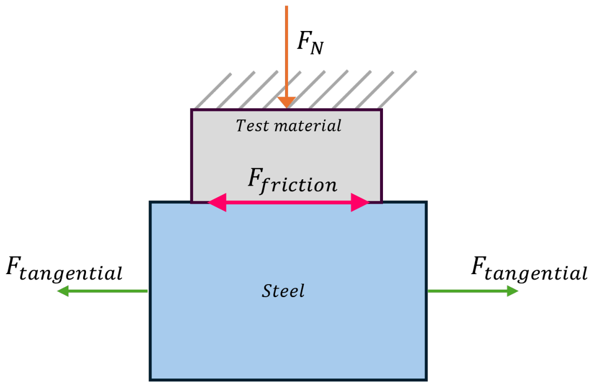

Figure 4.1: Overview reciprocating sliding test method

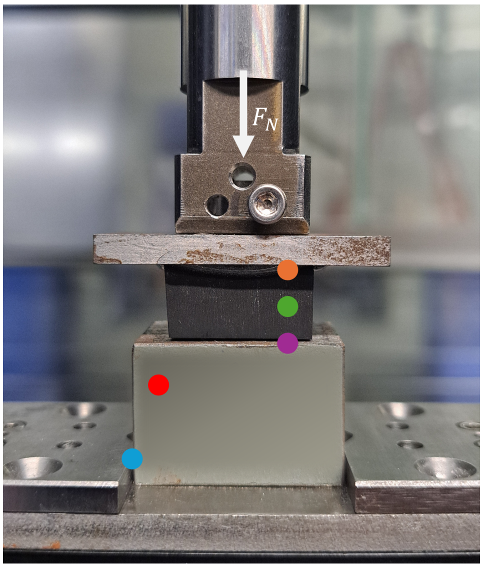

Figure 4.2: Set-up sliding friction test

For post-processing the test data, Coulomb's law of friction is assumed. The equation of Coulomb's friction law is given in equation 4.1. Within this law, the coefficient of friction is assumed to be independent of the normal force. The tests aim to determine the relation between the friction coefficient and the contact pressure. The outputs of the reciprocating sliding tests are the normal force, tangential force and displacement for all time steps. With these outputs, the friction coefficient μ can be calculated for each time step using equation 4.2. To find the relation between the friction coefficient and the contact pressure, tests should be conducted under different normal forces, and the values of μ should be compared.

$$\text{Coulomb's friction law: } F_{friction} = \mu \cdot F_N \tag{4.1}$$

$$\text{Friction coefficient: } \mu(F_N) = \frac{F_{friction}}{F_N} \tag{4.2}$$

Lubrication

Tests with dry, lubricated, and coated friction interfaces are performed. For the dry tests, no lubrication was applied, so the test represents a dry support pad that is clean of oil and dirt. For the lubricated tests, tap water is applied between the specimen and the steel to test the influence of water on the friction coefficient. For each wet test, six drops of water are applied to the centre of the steel material, see figure 4.3.

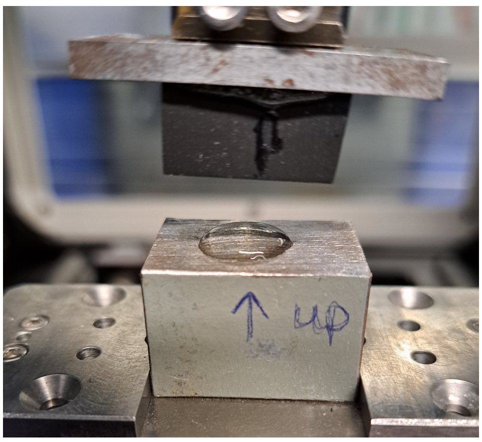

Figure 4.3: Water applied for wet test

Coating

For the first test, the steel specimen did not contain any coating. It was cleaned before testing to test with clean conditions. Later, a steel specimen with a coating is used to investigate the effect of a coating on the friction coefficient with increasing normal forces. The applied coating is 'Interzinc 22' with a thickness of 50-75 microns. This zinc-rich primer is suitable for offshore structures since it provides excellent corrosion protection for properly prepared steel substrates [41]. This means that this coating is well suited for the application of monopile coating.

4.1.2. Test set-up

The test set-up of the sliding friction tests is shown in figure 4.2. The test material (green dot) is glued (orange dot) to the cylinder that is connected with a grip connection to the part of the machine that exerts the normal force. A specimen of the second material (red dot) is fixed between the bottom clamps (blue dot). This part will start to move once the static friction limit is exceeded, resulting in increasing friction between the test material and the second material at the plane of the purple dot, until the static friction limit is overcome.

The testing machine and the materials have the following limitations that need to be taken into account when testing:

- Normal force: the limits of the normal force the machine can apply are 10 to 499 Newtons. Previous tests done by the TU Delft showed that the normal pressure can be relatively low for specific combinations of contact area and low normal loads, which may cause a higher variability of the measured friction force due to an unsteady contact configuration. Tests with a small ball in contact with a flat specimen combine contact area and low normal loads that give reliable results. However, the contact area used for the test specimen, in combination with normal forces lower than 10N, resulted in inaccurate results since the low contact pressure resulted in an unsteady contact configuration.

  According to the machine manufacturer, tests can be done up to 499N. However, previous tests done by the TU Delft with dry conditions did not exceed a normal force of 200N. Due to pronounced stick behaviour, the bottom plate's size needs to be increased to reach the desired displacement for higher forces. Tests with highly lubricated contacts should be able to reach 499N.
- Grip connection: the connection between the cylinder and the horizontal bar should be tightened with a screw; see figure 4.4. There is no check to determine if the grip connection is sufficient for the tests, which can become a problem for higher normal loads since high forces can result in loss of grip. When this happens, the applied force decreases, and the test is invalid.
- Alignment:
  - Horizontal alignment: the horizontal bar should be aligned within the margins of the spirit level (see figure 4.5).
  - Alignment of the test specimen: the test specimen should be aligned with the second material, meaning in the middle in both the longitudinal and transverse direction (see figure 4.2 and 4.6).

  Both alignments are hard to observe with the naked eye to ensure the accuracy of the alignment.
- Area test specimen: the test specimens were ordered with an area of 300 mm^2. The results of this test can be extrapolated to the full size of the saddles. However, the specimens were not fabricated with strict tolerances, as shown in figure 4.6. This means that the geometric surface area was slightly more or less than the assumed value of 300 mm^2. Although this could also be said for support pads in saddles, the deviations are considered smaller because a similar deviation has a proportionally larger impact on the much smaller test specimen.
- Displacement: the displacement of the moving part can be set by loosening a screw using an Allen key and counting the rotations. This step does not ensure high accuracies in the displacement.

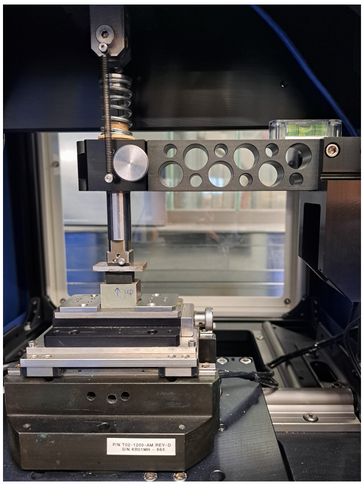

Figure 4.4:
Horizontal bar incl. grip connection

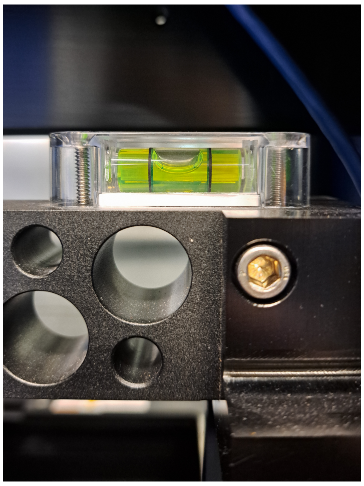

Figure 4.5:
Spirit level

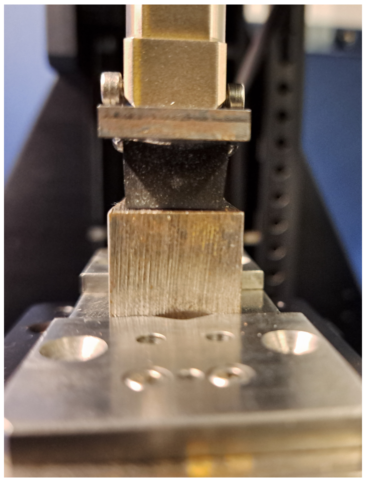

Figure 4.6:
Transverse alignment

4.1.3. Variation of normal forces

The revised numerical model resulted in contact forces between the monopile and the saddles during the entire wave cycle. The lowest normal force is zero when loss of contact occurs. The highest normal force in the saddles is 11.2 MN, which corresponds to 668 Newtons in the test specimen; see table 4.1. This is the preferred range for testing, so the influence of the normal force of the friction coefficient during the entire wave cycle is investigated.

During testing, it turned out that the actual possible test range was between 30 and 210 Newtons. The progressions of the test results below 30N do not correspond to the results of higher normal forces. Presumably, not all contact surfaces are being used for normal forces below 30N. More about this will be described in section 4.1.4. Above a normal force of 210N, the grip connection lost grip, so the horizontal bar started to tilt, and the applied normal force started to decrease. At the end of the test, the margins of the spirit level were exceeded, so the data for tests above 210N was considered invalid.

Table 4.1 shows how the test specimen parameters relate to the saddle parameters.

Parameter		Test specimen	Saddle	Unit
Area	A	300	$5.03{\cdot}10^6$	mm^2
Min. contact force	$F_{N,min}$	0	0	N
Max. contact force	$F_{N,max}$	668	$11.2{\cdot}10^6$	N
Max. contact pressure	P_{max}	2.23	2.23	N/mm^2

Table 4.1: Normal forces in test specimen and saddle

4.1.4. Testing parameters

This paragraph gives all the parameters that are used during testing. It should be noted that the results of the tests are only applicable to this research since all parameters are factors that can influence friction behaviour, as described in section 2.4.

Material properties

The used material for the tests is vulcanised rubber EPDM70. This material is resistant to higher temperatures and diluted acids. Furthermore, the material has an increased resistance to weather conditions and the hardness is Shore A70 [42]. The technical parameters of EPDM70 are given in table C.1 in appendix C.

Area specimen

To test with the maximum normal force that works in the saddles during the whole wave cycle, a test specimen with an area of 100 mm^2 would be sufficient since the maximum normal load for testing with a specimen of 100 mm^2 would be 223N. During the first tests with a test specimen of 100 mm^2, the shearing effects in the specimen were too high for the shear resistance of the glue. As a result, the glue broke, and the test specimen detached from the cylinder; see figure 4.7.

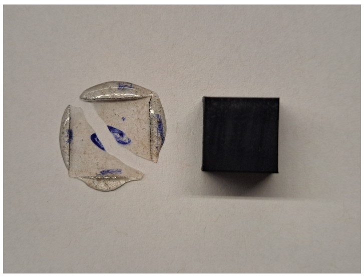

Figure 4.7: Broken glue for the test specimen of 100mm^2

To prevent detachment in the following tests, the area of the test specimen was increased to 300 mm^2. The disadvantage of this area is that the maximum normal force during testing is 668N to convert the results to a saddle scale, and the testing machine cannot apply a normal force above 499N.

As already described in the limitations of the testing, the cutting of the specimens was not done with high accuracy. Still, since the differences are slight, the assumption is that all tested specimens have dimensions of 15 by 20 mm, resulting in a geometric contact area of 300 mm^2. It should be noted that this assumption is conservative since the actual contact area might have been much smaller, and hence, the contact pressure would have been much higher. The actual contact area is qualitatively estimated to be 50% smaller than the geometric contact area, so less than 150 mm^2. However, this is also true for the support pads on the saddle scale, so this qualitative estimate is neglected on both scales, meaning a contact area of 300 mm^2 is used.

Steel

The second material is structural steel S275 without any lubrication or coating. This piece of material represents the monopile.

Displacement

The displacement should stay within the limits of the width of the second material. Once it exceeds these limits, the test material is draped over the edge of the steel, and the normal force can not be equally divided, resulting in unreliable test results. Four complete rotations with the Allen key are applied during the test preparations, corresponding to a maximum displacement of approximately 2.77mm.

Frequency

The frequency used during the test corresponds to the wave frequency of 0.604 rad/s as used in the monopile model (see equation 3.8). This wave frequency equals 0.1 Hz; see equation 4.3.

$$\begin{aligned} \omega &= 0.604 \text{ rad/s} \\ f = \frac{\omega}{2\pi} &= 0.096 \text{ Hz} \end{aligned} \tag{4.3}$$

Others

- Roughness: the roughness of both the steel and rubber specimens is unknown, so this factor's influence can not be investigated.
- Rate of loading normal force: the normal force is applied gradually before the movement starts in 1 minute.
- Rate of loading tangential force: the tangential force is applied gradually since the period of one displacement cycle equals approximately 10.5 seconds. The tangential force is applied to achieve the desired frequency and sliding distance.
- Temperature: the tests are all done at room temperature of 20°C.

- Contact area: the steel and rubber specimens were not perfectly flat. No conclusions can be drawn about the used contact area, especially during the tests with lower values of the normal force.
- Wear: through wear, rubber particles can separate from the main specimen and form a thin layer between the steel and the rubber specimen. If this is true, removing this layer during the test is not realistic because that is also not done during transport.

4.2. Results sliding friction tests

This section gives the test results. First, the results of three regular tests are presented in two parts: the initiation of motion and the steady state motion. The shearing behaviour of the regular tests is given next. Based on these tests, the friction coefficients for increasing normal forces are found, which are scaled to the saddle scale. The coated and lubricated test results are shown in the last two paragraphs.

4.2.1. Regular test

Three regular tests are performed, and the first and last displacement cycles are investigated. The first quarter of the cycle represents the initiation of motion, with the transition from static to kinetic friction. After the first cycle, the progression is getting towards a steady state that is reached fast after the first cycle, so it is assumed that this pattern would not change in any longer test. An example of a test at 90N is shown in figure 4.8. The initiation of motion starts at (0, 0) and changes from static to kinetic friction around (0.6, 0.58). The lines of the steady state are plotted on top of each other, resulting in the thick blue line.

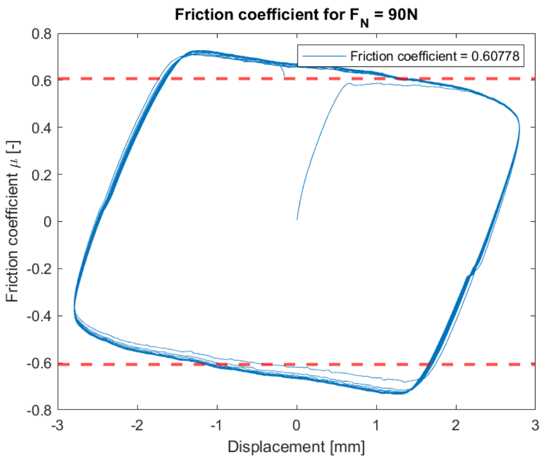

Figure 4.8: Complete test result 90N

The tests were performed for normal forces of 30, 60, 90, 120, 150, 180, and 210 Newtons, and the testing time was 5 minutes. Table 4.2 shows how the normal forces relate to the contact pressure.

	Contact pressure	
Normal force [N]	Testing scale [N/mm^2]	Saddle scale [Pa]
30	0.1	5.96
60	0.2	11.93
90	0.3	17.89
120	0.4	23.86
150	0.5	29.82
180	0.6	35.79
210	0.7	41.75

Table 4.2: Contact pressure in testing and saddle scale

Initiation of motion

At the beginning of the cycle, during the initiation of motion when the tangential loads increase, the three tests with lower normal forces show a clear transition from static to kinetic friction. The transition occurs on the peaks of the friction coefficient; see figure 4.9. First, the material sticks and the coefficient of friction increases until the maximum static friction. Once the behaviour changes from stick to slip, the material starts to move, the coefficient of friction decreases, and the kinetic friction is reached.

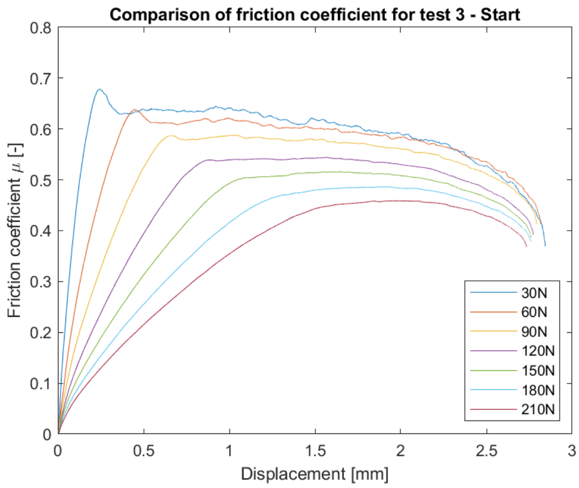

Figure 4.9: Initiation test 3

From the results, it can be seen that the shearing effect is getting more pronounced for higher normal forces. The softening of the material causes this, so the material's flexibility is higher for higher normal forces. For example, when focussing on figure 4.9, the blue line of 30N shows the transition from static to dynamic friction around a displacement of 0.2mm, but the red line of 210N does not have such a clear transition due to the shearing effects. The slope of the shearing effects decreased with increasing normal forces, and the size of the test specimen was a limiting factor during the tests with higher normal loads. In the test set-up, the length of the EPDM70 specimen was 20 mm while the length of the support pads in the saddles was 1.2 m, so it was impossible to test the shearing effect on the saddle scale.

The first and second tests do not show a clear transition from static to kinetic friction (see figure 4.10 and 4.11). The second test results (figure 4.11) show that the lines of the friction coefficient for different normal forces converge already in the first half cycle, which does not happen that fast in the first and third tests.

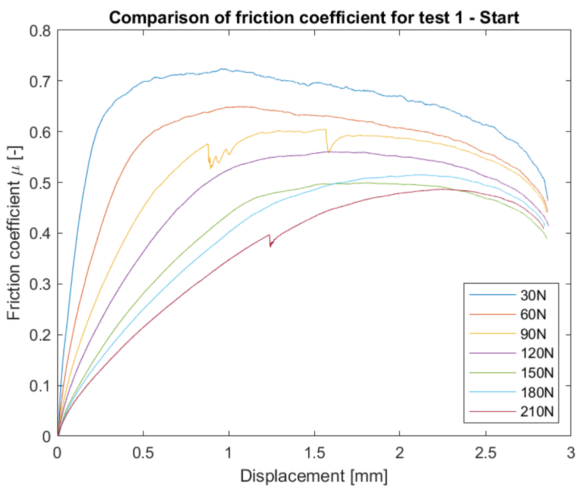

Figure 4.10: Initiation test 1

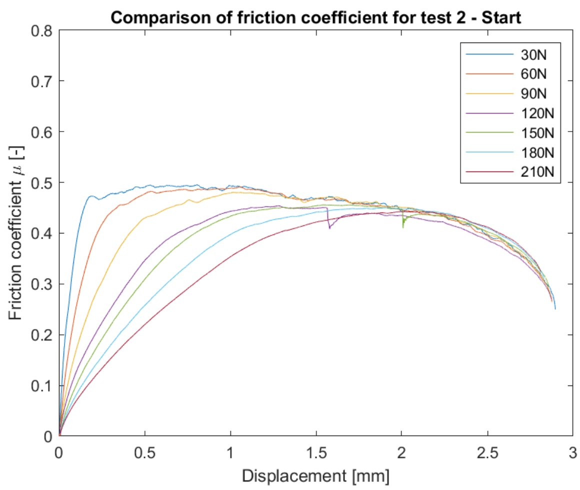

Figure 4.11: Initiation test 2

Steady state motion

After the first cycle, the motion reaches a steady state. One of the last cycles was selected to verify that the grip connection and normal force were consistent throughout the entire test.

The inclined vertical sections of the curves represent the deceleration of the motion, followed by the reversal of the motion direction. It can also be observed that the slope of these inclined vertical sections decreases with increasing normal force, and the slope of these lines corresponds to the shear modulus. During the initiation of motion, it was already clear that the shearing effects increased for increasing normal forces, and this principle remained during the whole time of the tests. The differences became even more apparent since the steady state results show an evident slope change between the lines of different normal forces. Figures 4.12, 4.13, and 4.14 show the steady state results of tests 1, 2 and 3, respectively.

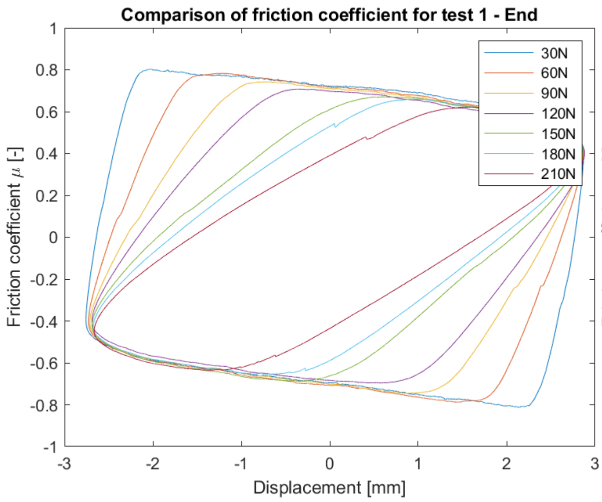

Figure 4.12: Steady state test 1

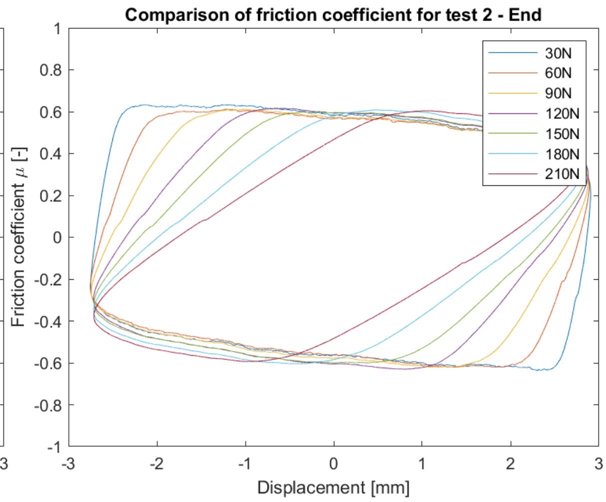

Figure 4.13: Steady state test 2

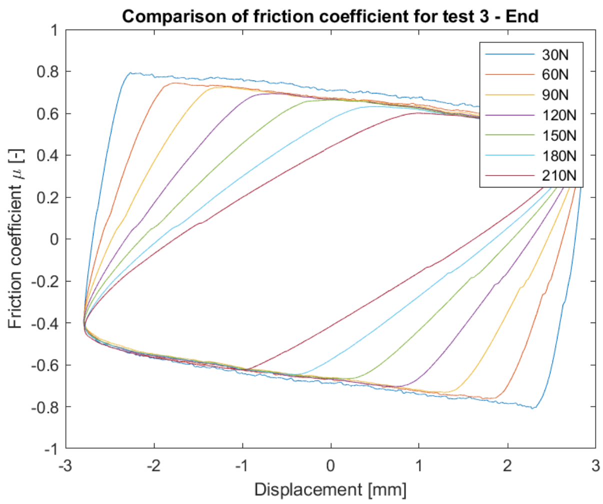

Figure 4.14: Steady state test 3

Shearing effects

The shear modulus of EPDM70 can be calculated based on the steady-state results of the tests. The modulus of rigidity is defined as the ratio of shear stress to the shear strain; see equation 4.4.

$$\begin{aligned} &\text{Shear modulus: } G = \frac{\tau_{xy}}{\gamma_{xy}} = \frac{F \cdot h}{A \cdot \Delta x} \\ &\text{Where:} \\ &\tau_{xy} = \text{Shear stress} \\ &\gamma_{xy} = \text{Shear strain} \\ &F = \text{Friction force} \\ &h = \text{Height of the test specimen} \\ &A = \text{Area of the test specimen} \\ &\Delta x = \text{Transverse displacement} \end{aligned} \tag{4.4}$$

In this investigation, the slope at a small delta around a friction coefficient of zero at both the positive and negative displacement is used to indicate the shearing effects in the test specimens. An average of the two slopes gives the slope for that normal force; see equation 4.5. The steeper the slope, the more shearing effects occur. So, comparing 30N and 210N of figure 4.14, the slope of 30N is much higher compared to the slope of 210N, meaning more shearing effects occur for an increasing normal force.

$$\text{Slope due to shearing effects} = \frac{\Delta \mu}{\Delta x} \tag{4.5}$$

The material's shearing effects can be expressed as a function of normal force. The results of these calculations for all 3 tests are shown in table 4.3 and figure 4.15. The average shearing slope of the tests is plotted in purple in figure 4.15. The equation of the shearing effects of EPDM70 as a function of the normal force based on the average of the tests is given in equation 4.6 and plotted in green in figure 4.15.

	Slope due to shearing			
Normal force [N]	Test 1	Test 2	Test 3	Average
30	2.15	2.91	3.32	2.79
60	1.36	1.83	1.68	1.62
90	0.87	0.85	0.87	0.86
120	0.60	0.65	0.82	0.69
150	0.39	0.48	0.46	0.44
180	0.36	0.34	0.35	0.35
210	0.27	0.26	0.29	0.27

Table 4.3: Slope of the shearing lines for different normal forces

$$\begin{aligned} &\text{Slope of shearing lines for EPDM70:} \\ &\text{Slope}(F_N) = 199.76 \cdot F_N^{-1.214} \end{aligned} \tag{4.6}$$

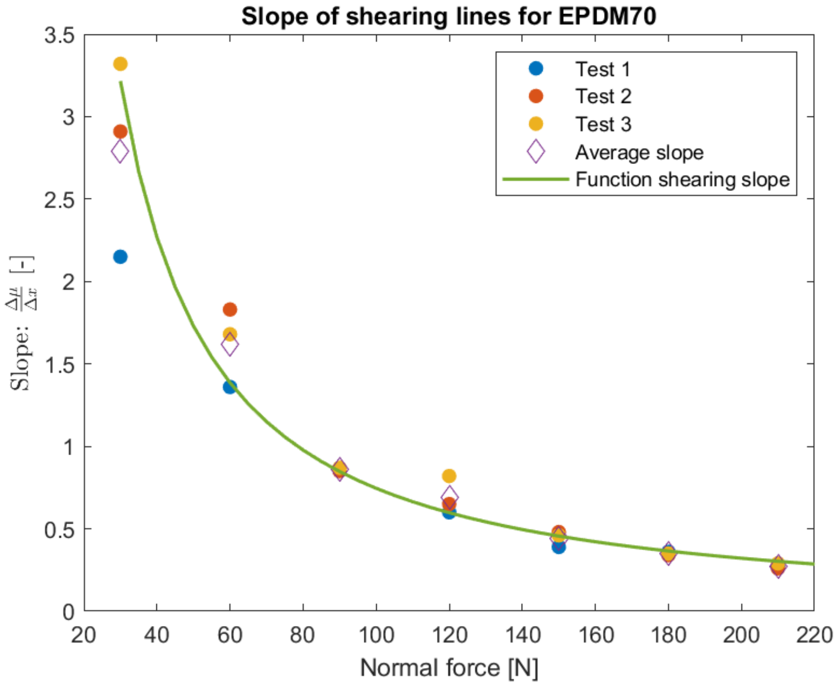

Figure 4.15: Shear modulus EPDM70

Figure 4.15 shows that the slope of the shearing lines decreases for increasing normal forces, meaning there is more stick behaviour at higher forces due to the shearing of the test specimen. The slip behaviour starts sooner for lower normal forces since the test specimen deforms less due to shearing. In this phase, it is not possible to determine the effect of shearing on the saddle scale since the sliding friction test machine limits test specimen size. However, the length-height ratio of the test specimen and saddle support pad are compared; see equation 4.7.

$$\begin{aligned} \text{Test specimen: } \frac{L}{H} &= 2 \\ \text{Saddle support pad: } \frac{L}{H} &= 24 \end{aligned} \tag{4.7}$$

The support pad's L/H ratio is twelve times larger, so the shearing effects are deemed negligible in the longitudinal monopile model.

4.2.2. Regular friction coefficient

Roll Group designs the seafastening arrangement without considering friction to entirely prevent the motion of the monopile in the longitudinal direction. This objective is considered when post-processing the friction coefficients from the results. Since the goal of the seafastening is that no displacement occurs at all, using the steady-state friction results would not match reality since it skips the motion initiation. Once the external force is applied, the friction force first behaves in the static friction regime. For that reason, the results of the tests during the motion initiation are selected for application in the longitudinal monopile model.

After this decision, the motion initiation test results are analysed. The first observation is that the friction coefficients of the second test for all normal forces are lower than tests 1 and 3. This behaviour can be attributed to the fact that the steel specimen was not cleaned before starting the second test. A thin layer of rubber formed on the steel material due to wear caused in the first test. Based on this difference during testing, it is decided not to consider the second test's results when defining a friction coefficient.

When analysing the results of the first test, both 90 and 210 Newtons have some unexplainable peaks in their lines, and the lines of 150 and 180 Newtons cross each other. The results of the third test do not have such small errors in the data. The only remark regarding the third test results is the lack of smoothness for 30, 60 and 90 Newtons in the kinetic friction regime. This is probably caused by the roughness of the test specimen and steel material, which results in a lower contact area. This effect is considered negligible since the pattern is clear, and this bumpy kinetic friction line is no longer visible for normal forces above 90 Newtons. For that reason, the test results of the third test, as shown in figure 4.16, are used to investigate the effect of an increasing normal force on the friction coefficient.

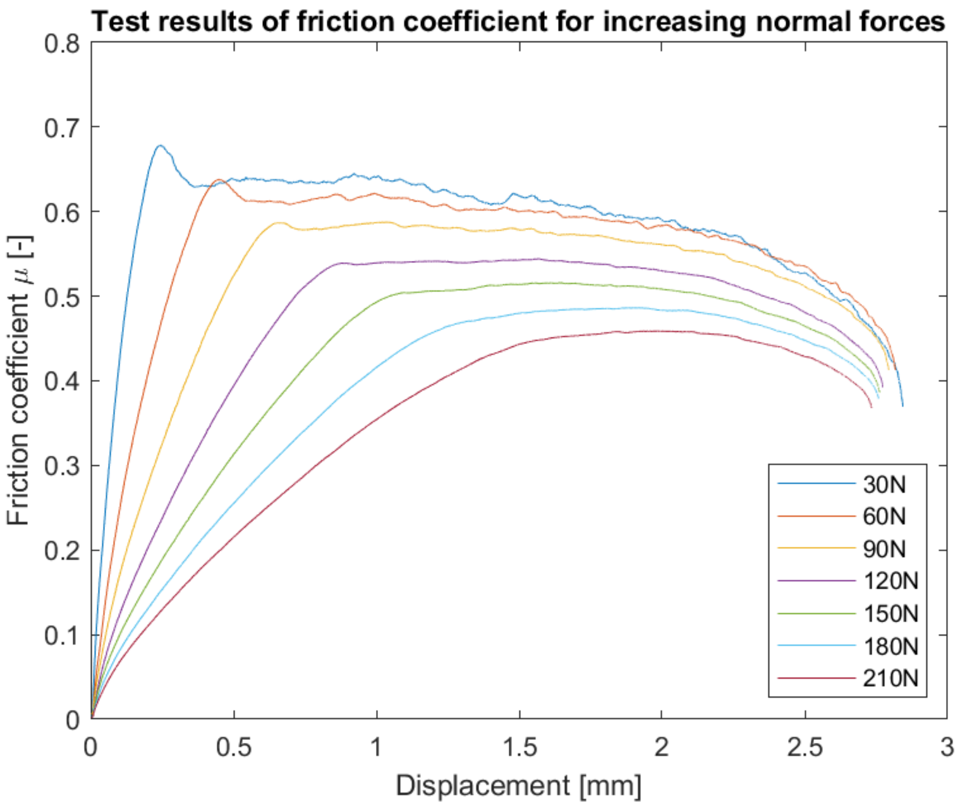

Figure 4.16: Selected test results for investigation

As already stated, the most relevant part of the test results for monopile seafastening is the motion initiation, and within that part, the static regime is the regime of interest. The static regime is easy to determine for the normal forces with a clear transition, see figure 4.17. At the transition from static to kinetic friction changes the sticking phase into the sliding phase. The shear modulus is stiff enough during cases where this transition is clear. In cases without a clear transition, the shear modulus is flexible meaning the support pad shears in the sticking phase, and the movement of the monopile starts when the sticking phase changes in slip. However, as can be seen in figure 4.17, for example with the red line of 210N, it is hard to determine where the stick phase shifts to slip. Table 4.4 shows the maximum static friction coefficient for the cases with a clear transition and all kinetic values of μ. The kinetic friction coefficients are obtained by taking the maximum value of μ in the kinetic region for each normal force.

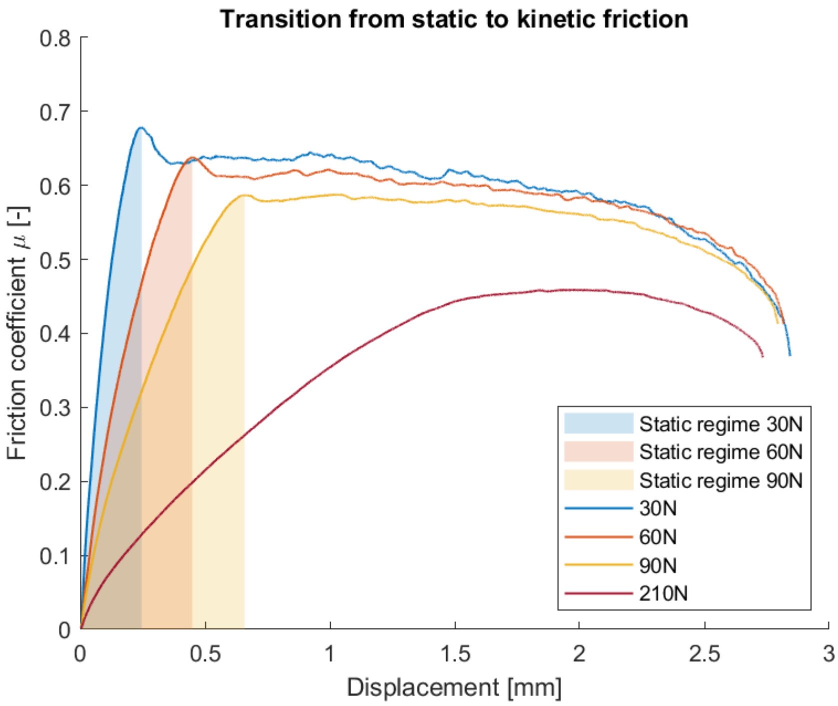

Figure 4.17: Transition from static to kinetic friction for lower normal forces

Normal force [N]	Max. static μ	Kinetic μ	Difference
30	0.678	0.625	7.82%
60	0.638	0.600	5.96%
90	0.587	0.577	1.70%
120	-	0.543	-
150	-	0.515	-
180	-	0.486	-
210	-	0.459	-

Table 4.4: Coefficients of friction

To implement the friction coefficients of the test in the monopile model for varying normal forces, the results of table 4.4 should be extended up to 668N (see table 4.1). When plotting the kinetic friction coefficient, it can be concluded that this behaves almost linear; see the blue marked line in figure 4.18. However, the static friction coefficient is of higher interest but unclear for all normal forces. To be conservative for safety reasons, all static friction coefficients are determined as 90% of the kinetic friction coefficient. With this assumption, there is still a margin for the cases above 90N with a flexible shearing stiffness to prevent the friction from becoming kinetic. The static friction coefficient with the safety margin is plotted in orange in figure 4.18.

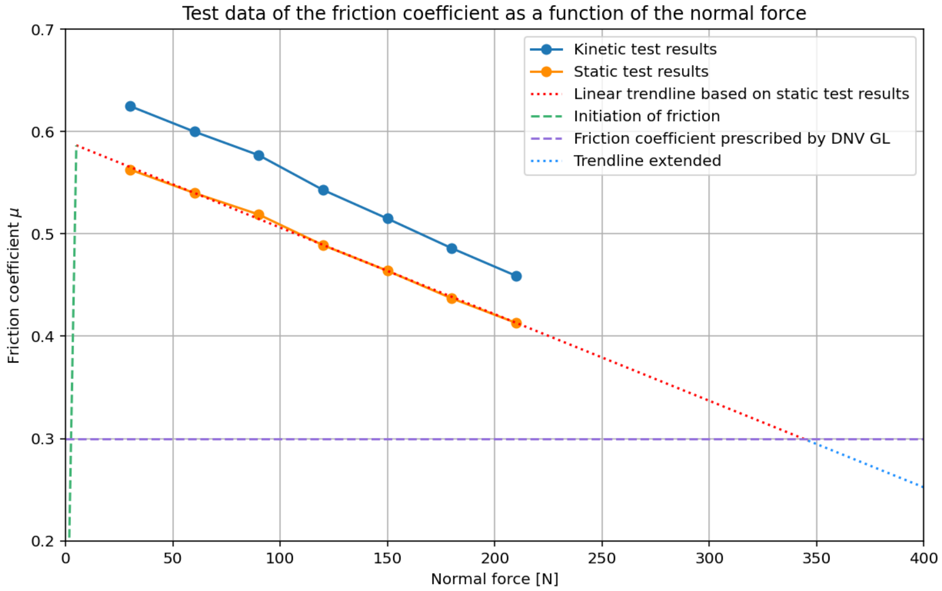

Figure 4.18: Test data including linear trendline of static friction results

A linear trendline can be determined based on the assumed static friction coefficient. However, this relation results in a friction coefficient of zero for normal forces above 700N (see figure 4.19), which does not match reality. In reality, the friction force only equals zero if there is no normal or tangential force.

So, with the testing results, no conclusion can be drawn on the behaviour of the friction coefficient for normal forces above 210N. However, experimental data has shown that the friction coefficient levels out to a steady value for higher normal forces as described in section 2.4.2. For this reason, the assumption is made that the coefficient of friction decreases linearly until a coefficient of friction of 0.3 is reached, and from then on, this value of μ is considered for all normal forces. The value of 0.3 is selected since this is the coefficient of friction between rubber and steel in dry and wet conditions prescribed by DNV [10]. The tested and assumed behaviour of the friction coefficient for varying normal forces is shown in figure 4.19.

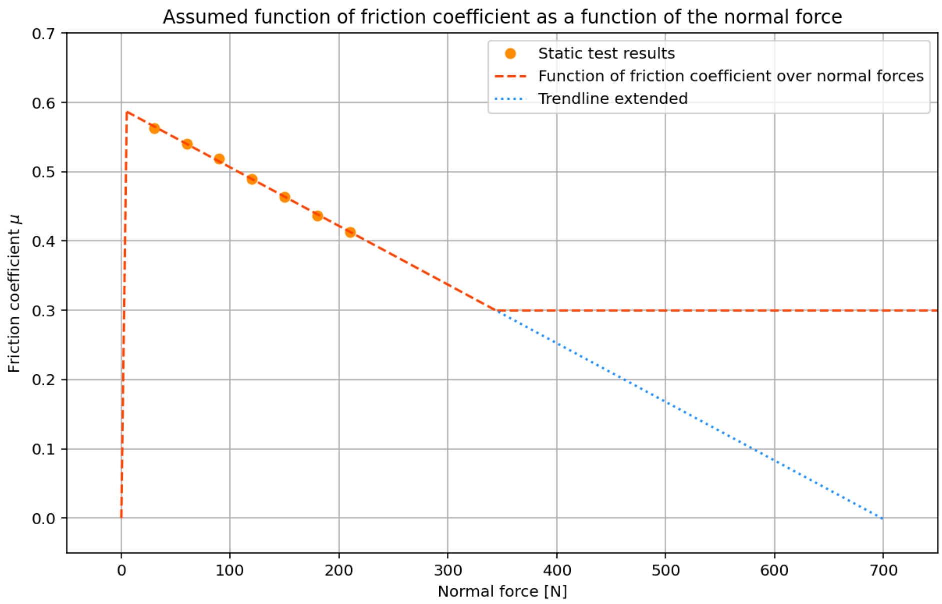

Figure 4.19: Assumed function of μ as function of F_N based on test results

The function of the red dotted line in figure 4.19 is scaled with the use of table 4.1 to the saddle scale; see figure 4.20. This scaled function will be applied in the numerical monopile model to calculate the friction force in the saddles for each wave height and their corresponding normal forces. After this implementation, the total available friction force can be calculated. With this data, the most cost- and material-effective seafastening arrangement can be determined.

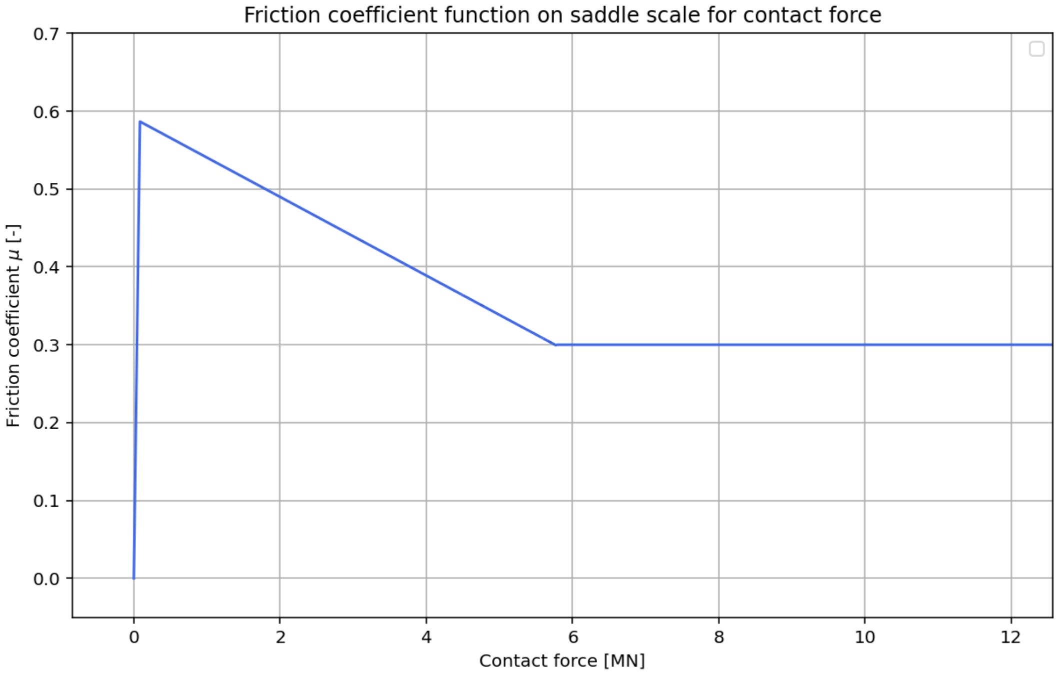

Figure 4.20: Function of μ as function of the contact force on saddle scale

4.2.3. Coated friction coefficient

Previous research showed that a coating between steel and rubber results in a different friction behaviour than cases without coating [43, 44]. However, whether a coated material behaves the same as an uncoated material for increasing normal forces is unknown. A test with a coated steel specimen is performed to investigate the effect of a coating on the relation between the coefficient of friction and the normal force. The used coating is a layer of 50-75 microns of 'Interzinc 22', see figure 4.21. During the tests, the EPDM70 specimen started to wear; see figure 4.23. Comparing the before and after figures of the coating, it can be observed that it also started to wear during testing; see figure 4.22. From these figures, it can be concluded that the coating did not have equal roughness throughout the tests due to wear.

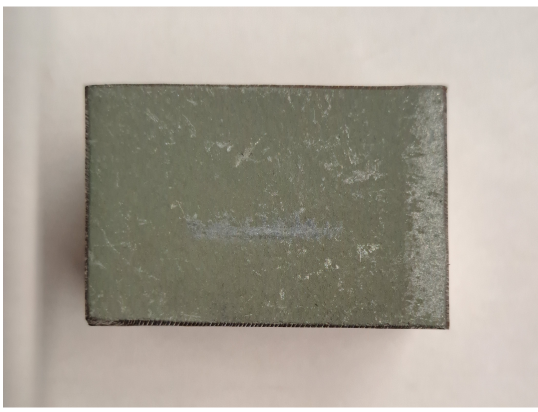

Figure 4.21: Coating before tests

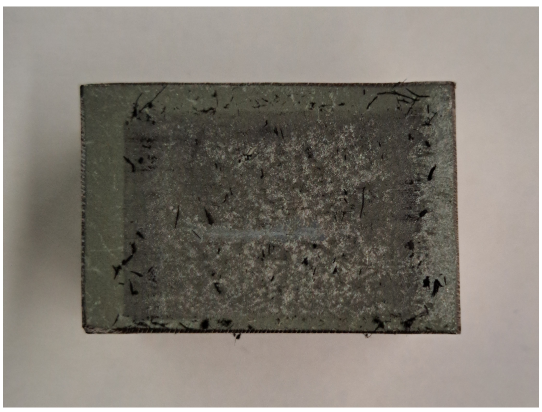

Figure 4.22: Coating after tests

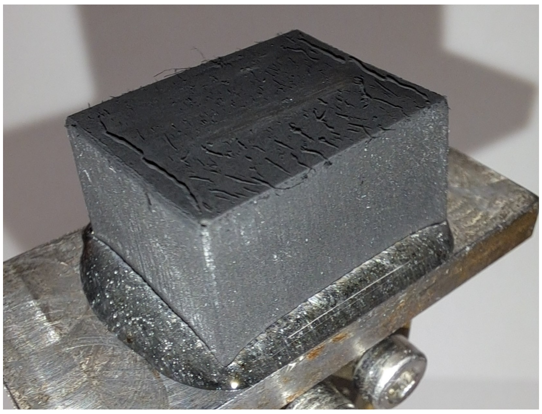

Figure 4.23: Wear after coated test

Before testing the coated steel specimen, an uncoated steel specimen was tested with the same EPDM70 specimen as a comparison for the coated test results. Both these results are plotted in figure 4.24. The coated steel specimen had a higher friction coefficient than the uncoated material, but the behaviour was almost identical. Based on the testing results, the coefficient of friction is expected to increase when a coating is applied since figure 4.24 shows higher friction coefficients for the coated tests. However, it is hard to determine a function of μ as a function of the normal force for coated steel on EPDM70 since many factors can influence this function, for example, the coating thickness or the coating type. Therefore, it is recommended that new tests be performed if any property changes compared to the properties used during testing.

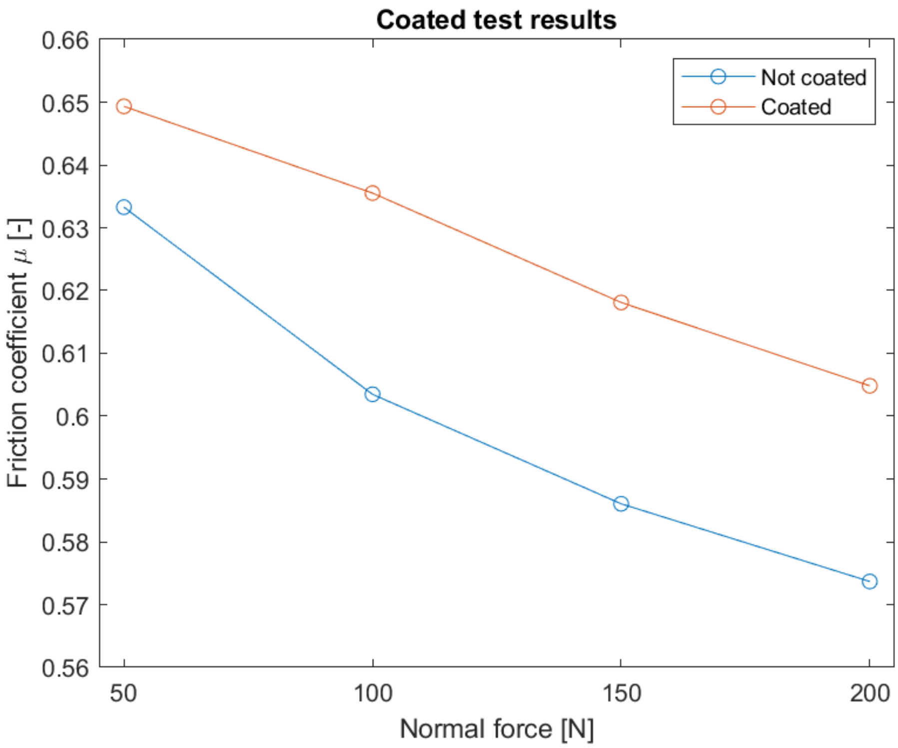

Figure 4.24: Coated test results

4.2.4. Lubricated friction coefficient

Lubricated tests are performed with tap water as contamination. In reality, contamination is present at the support pads in lubricated situations. However, this was impossible in the test set-up, so the water is applied on top of the steel specimen; see figure 4.25. Before the test, when the test specimen is moved to the steel specimen, the water sticks between the two materials due to capillary adhesion, see figure 4.26. Because of this effect, it is assumed that the water is divided equally over the whole surface when the EPDM70 and steel specimen are in touch. The contamination is also located next to the test specimen; see figure 4.27. It is unknown what amount of contamination remains between the two materials, but it is assumed that this is the same amount for all normal forces. Figure 4.28 shows that the contamination is located at the EPDM70 and steel specimen after testing.

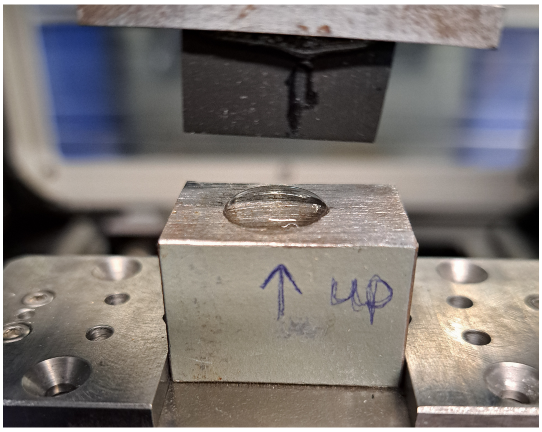

Figure 4.25: Water drops before test

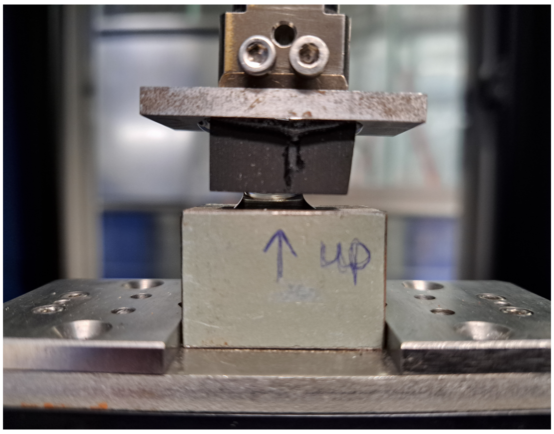

Figure 4.26: Water layer before test

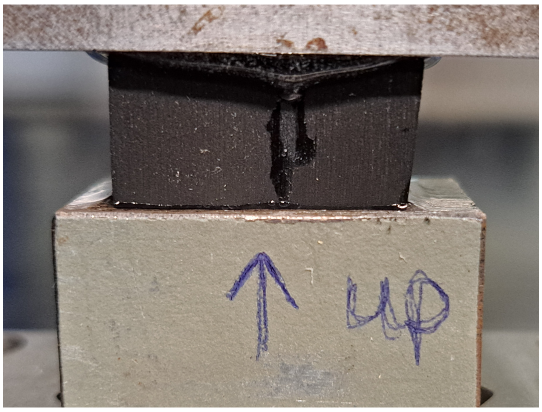

Figure 4.27: Water layer during test

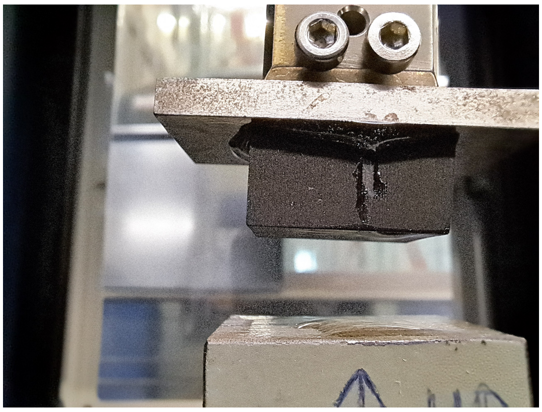

Figure 4.28: Water layer after test

First, dry tests are performed with the same test specimen to compare with the wet tests. The test results of the lubricated tests are shown in figure 4.29. The tests show an increase in the friction coefficient for an increasing normal force, whereas both the regular and the coated tests showed a decrease of μ for an increasing normal force. This behaviour was not expected, especially not for the dry test, but it is hard to find the cause of this opposite behaviour. Examples of possible causes are the imperfect alignment of the test specimen with the steel specimen, the rate of contamination evaporating, and the variability between this specimen and the previously used ones. Significant variability was observed between the specimens regarding the geometric contact area. All test results of the lubricated tests are given in appendix D.

Nevertheless, it can be concluded that the friction coefficient is lower for conditions where the contact area is contaminated with tap water. More contaminated tests are recommended to investigate the behaviour of the friction coefficient at lubricated contact areas. It would be interesting to examine the influence of the test duration on the friction coefficient to see if it increases throughout the test due to the contamination evaporating during the test.

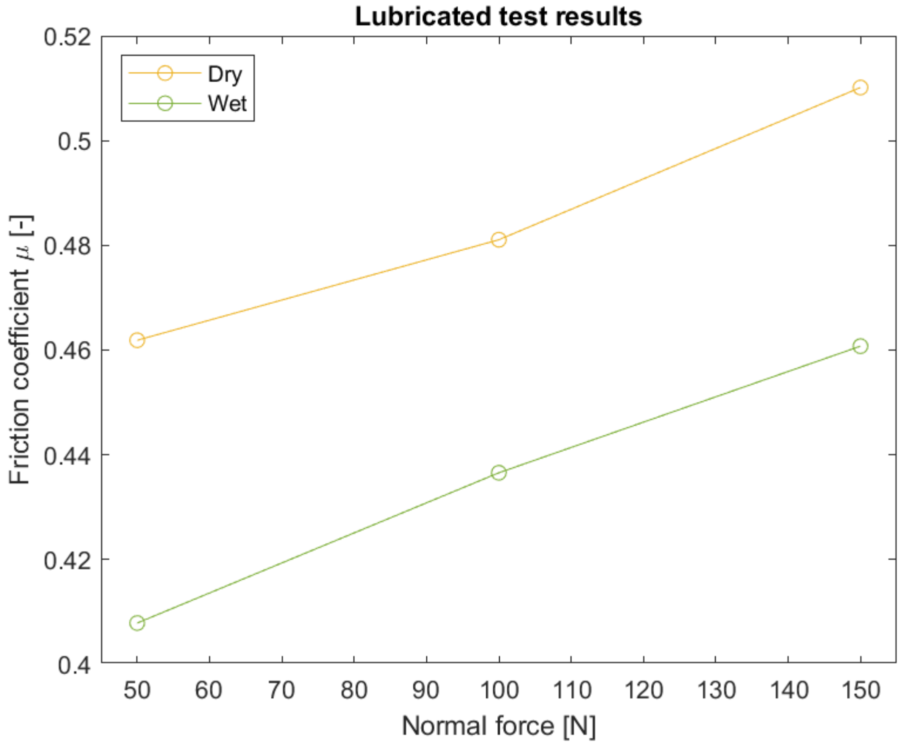

Figure 4.29: Lubricated test results

4.3. Conclusion sliding friction tests

The sliding friction tests are performed for three conditions: dry & uncoated, dry & coated and wet & uncoated conditions. The dry and uncoated conditions were tested three times, and the results showed a relation between the friction coefficient and the contact pressure. The static friction regime during the initiation of motion is considered the most relevant phase, as a monopile restrained from longitudinal motion operates only in the static friction regime without relative displacement. Any displacement observed during the tests within the static regime resulted from the shearing effect, with shearing displacement increasing as normal forces grew. However, the saddle support pad's length-to-height ratio was much higher than the test specimen's. Therefore, this shearing effect is considered negligible in the longitudinal monopile model. To determine the shearing effect on the saddle scale, more sliding friction tests are recommended with test specimens with lower thickness.

The test results indicate a decreasing friction coefficient as normal forces increase, with a linear decline observed within the testing range. Beyond the testing range, the linear trendline is extrapolated until it reaches a friction coefficient of 0.3, which DNV-ST-N001 specifies for rubber-steel friction under wet and dry conditions. This relation between the friction coefficient and normal force is found on the test scale and is scaled to the saddle scale. The function of the friction coefficient μ, depending on the contact pressure, is implemented in the longitudinal monopile model. From the coated and lubricated test results, it can be concluded that the test results only apply to this specific research and the properties used since the coated and lubricated results deviate from the regular test results, so any changed parameter will result in a different friction behaviour.

5

Results

This chapter presents the findings from the research conducted using the longitudinal monopile model, with results derived from a mass-spring system including friction and lashing forces. The first section describes the dynamic deflections used in the coupled fluid-ship model, and the second section gives the normal forces in the saddles as a result of the dynamic deflections. The next section describes the friction forces belonging to the normal forces based on the test results, and it includes the total available friction capacity for all cases.

After these sections, the results of the analyses of the mass-spring systems are given. First, the results of types 3 and 4 are shown where an external and lashing force is applied to calculate the displacement of the monopile for different lashing configurations. Friction based on the test results is included in the system of the next section to calculate the displacement for the static case. The following section gives the mass-spring system type 5 results for the governing dynamic case. These analyses define the most cost- and material-efficient seafastening arrangement for the monopiles that fully prevents the longitudinal motion of the monopile throughout the whole wave cycle, described in the last section.

5.1. Dynamic deflections

The dynamic deflections of the vessel with the new ballast condition are calculated for four cases:

- Departure hogging
- Departure sagging
- Arrival hogging
- Arrival sagging

For the departure condition, the fuel tanks are filled for 90% while the arrival condition calculates with tanks filled for 10%. The vessel is ballasted to have zero trim and heel during the departure conditions. Hence, the vessel may have a small trim and heel angle during arrival. The results of GHS show that the dynamic deflections for hogging waves are larger than those for sagging waves. The GHS deflection lines of the four cases are plotted in 5.1. The deflection of the arrival hogging condition is the largest, so these deflections are considered governing and, for that reason, used in the revised numerical model to calculate the normal forces in the saddles.

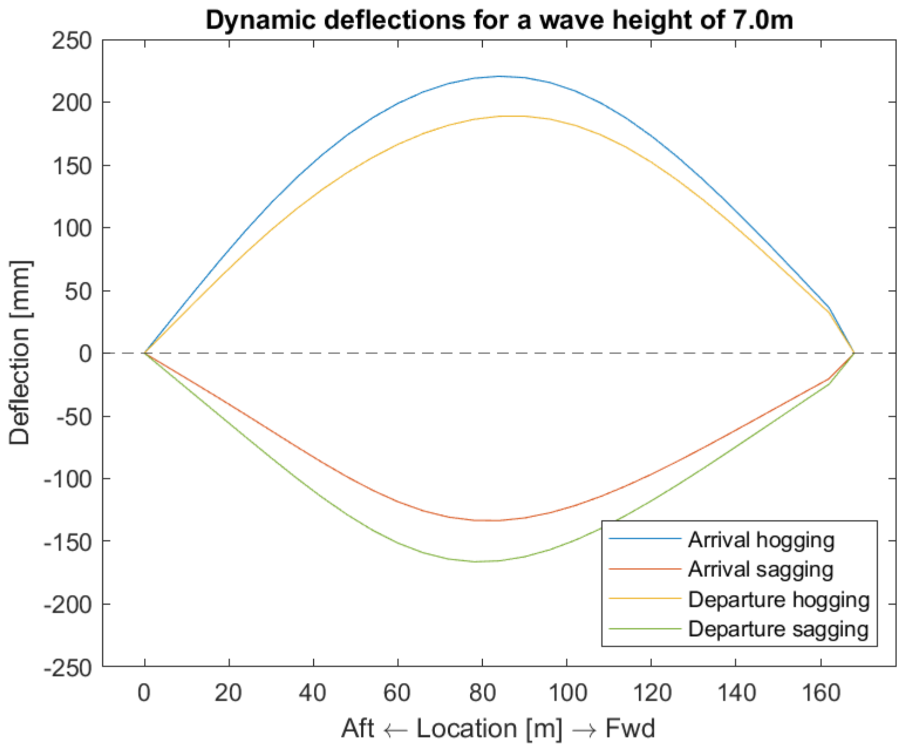

Figure 5.1: Dynamic deflections from GHS for a wave height of 7m and 4 monopiles

5.2. Normal forces in saddles

The normal forces in the saddles for each saddle configuration and wave heights from 1.0 to 7.0 meters are calculated with the revised numerical model; see table 5.1. Loss of contact occurs when the normal force is 0 Newton. As can be seen, intermittent contact occurs for lower wave heights when the number of saddles increases. For cases with loss of contact, the normal force increases in the saddles that are still in contact. The normal forces of table 5.1 are used to calculate the friction force per saddle for each wave height.

Normal force [MN]							
	H_s						
Saddles:	**1.0**	**2.0**	**3.0**	**4.0**	**5.0**	**6.0**	**7.0**
3	2.81	2.22	1.73	1.17	0.74	0.21	0.05
	4.91	6.13	7.15	8.30	9.19	10.29	11.20
	2.74	2.09	1.52	0.90	0.40	0.08	0
4	1.87	1.11	0.48	0.08	0	0	0
	3.18	3.95	4.59	5.31	5.72	6.24	6.66
	3.41	4.21	4.89	5.51	5.11	4.33	3.99
	1.73	0.89	0.17	0	0	0	0
5	0.65	0.04	0	0	0	0	0
	1.74	1.69	3.07	2.79	2.50	2.29	2.16
	3.44	4.54	4.29	4.65	4.99	5.49	5.97
	3.12	3.71	3.18	2.47	2.18	1.89	1.63
	0.65	0.08	0	0	0	0	0
6	0	0	0	0	0	0	0
	1.43	1.99	1.48	0.78	0.42	0.03	0.11
	2.54	3.19	3.68	4.16	4.56	5.05	5.46
	3.48	3.26	3.66	4.19	4.57	4.96	4.97
	2.73	1.79	0.94	0.42	0.03	0	0
	0.01	0	0	0	0	0	0
7	0.03	0	0	0	0	0	0
	1.39	1.13	0.44	0.21	0	0	0
	1.98	2.55	2.83	3.06	3.26	3.54	3.62
	2.10	2.84	3.41	3.97	4.28	4.52	4.78
	2.22	2.60	2.80	2.97	2.75	2.10	1.72
	1.54	0.83	0.01	0	0	0	0
	0	0	0	0	0	0	0

Table 5.1: Normal forces in saddles for different wave heights in the hogging arrival condition

Since the hogging arrival condition is considered to be the governing case based on the dynamic deflections, these normal forces are used in the longitudinal monopile model. Within one wave height, the normal forces are assumed to be in phase.

The hogging case results in the highest forces in the saddles in the middle and loss of contact in the outer saddles. When analysing the sagging case, the normal force in the outer saddles is expected to be the highest and loss of contact occurs in the saddles in the middle. However, where the normal force in a hogging case is the highest in the middle saddle for a wave height of 7.0 meters and a configuration of 3 saddles, the force is expected to be divided over the two outer saddles during a sagging case. By dividing the force over the two outer saddles instead of over a single middle saddle, the contact pressure is lower, resulting in a higher friction coefficient. Therefore, it is expected that sagging cases are not governing since the total friction capacity is expected to be higher than in the arrival hogging case.

5.3. Friction forces

The friction capacity per saddle for each wave height and each saddle configuration can be calculated by using equation 4.1, where the normal forces follow from table 5.1 and the friction coefficient from the friction function of figure 4.20. The friction capacity per saddle and the total friction capacity per wave height for three saddles are shown in figure 5.2. The plots with the friction capacities for all wave heights for the other saddle configurations are in appendix E. Figure 5.3 shows the total friction capacity for each saddle configuration per wave height. A general trend can be observed, showing a decrease in friction capacity with increasing wave heights, though with some exceptions. This aligns with the observation that the friction coefficient decreases with higher normal forces, as higher wave heights lead to larger deflections, resulting in higher normal forces. The lowest available friction capacity is 3.25 MN and is reached with a wave height of 6.0m in a configuration with three saddles.

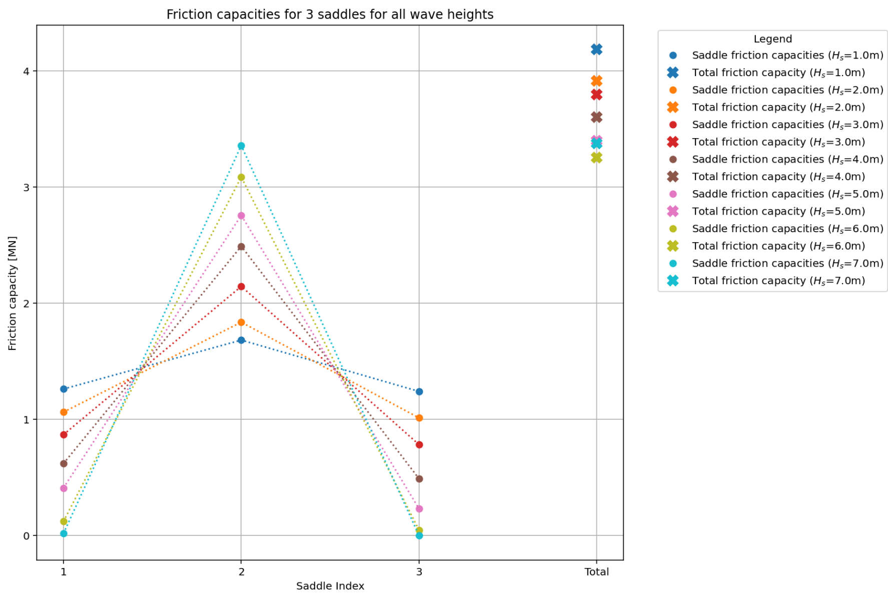

Figure 5.2: Friction capacities in 3 saddles

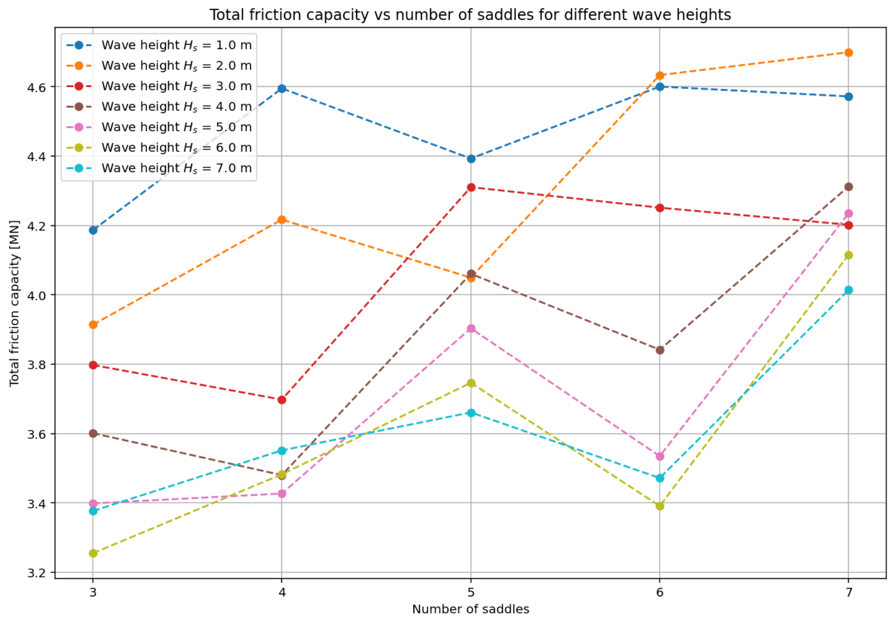

Figure 5.3: Total friction capacity for all saddle configurations

5.4. Dynamic analysis without friction

To simulate the same seafastening calculations as Roll Group does, the monopile model is set up as the mass-spring system types 3 and 4, so including the external force and lashing wires, but without friction force. Figure 5.4 shows the forces in the system for configurations of 2, 8 and 16 lashing wires, three saddles and a wave height of 7.0 meters. It can be seen that the lashing force increases for an increasing number of lashing wires (yellow dotted line). Hence, the resulting force decreases (red line). When 16 lashing wires are applied, the external force is lower than the available lashing capacity, preventing the monopile from motion in the longitudinal direction.

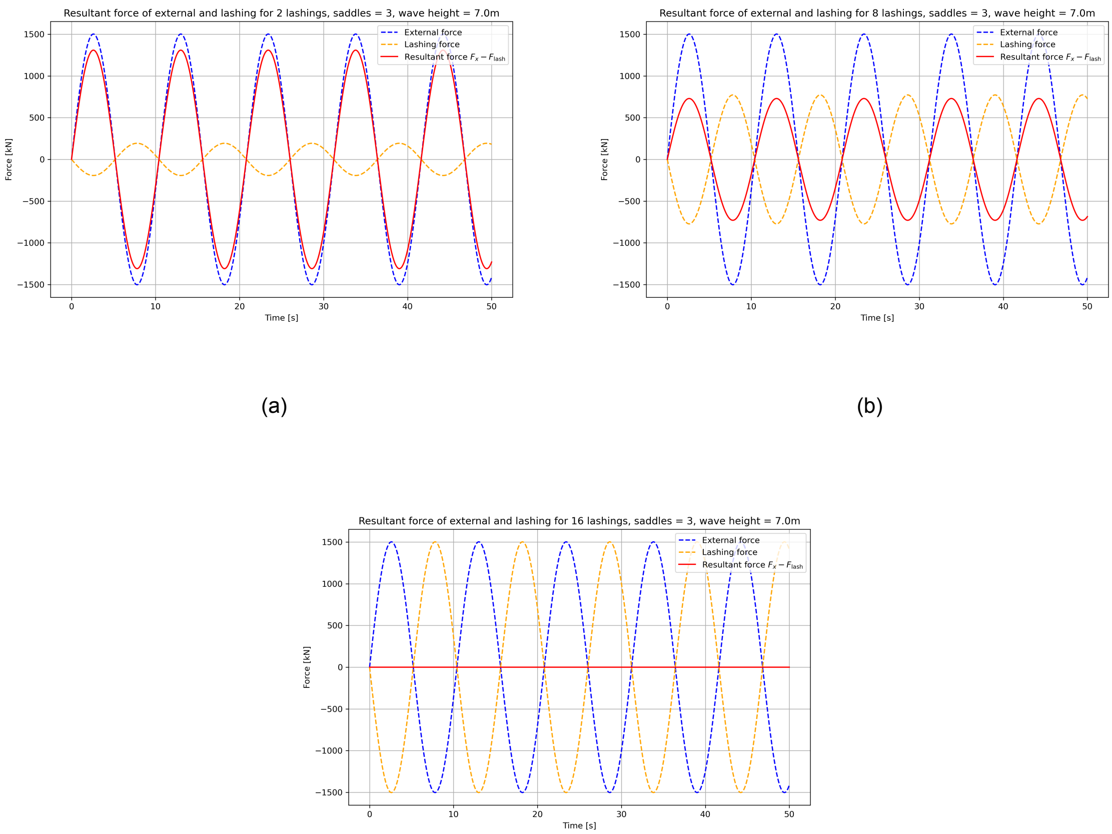

Figure 5.4: (c)
Resultant force for dynamic cases without friction: (a) 2 lashings, (b) 8 lashings, and (c) 16 lashings.

The accelerations in the longitudinal direction are the largest for a wave height of 7.0 meters, as described in section 3.2.2, resulting in lower displacements for all lashing configurations for cases with lower wave heights. The maximum displacement for all wave heights is plotted against the number of lashing wires in figure 5.5. The figure gives a clear overview of the decreasing displacement for increasing lashing wires for all wave heights. The vertical deflections are the largest for a wave height of 7 meters, and so is the displacement of the monopile in the longitudinal direction. If friction is not considered in the seafastening calculations, 16 lashing wires should be applied to prevent motion in the longitudinal direction for all wave heights.

It should be noted that the lashing wires will break once the total lashing capacity is insufficient to counteract the external force. For the maximum displacement of figure 5.5, it is assumed that this displacement occurs because the lashing wires elongate while remaining at capacity before breaking.

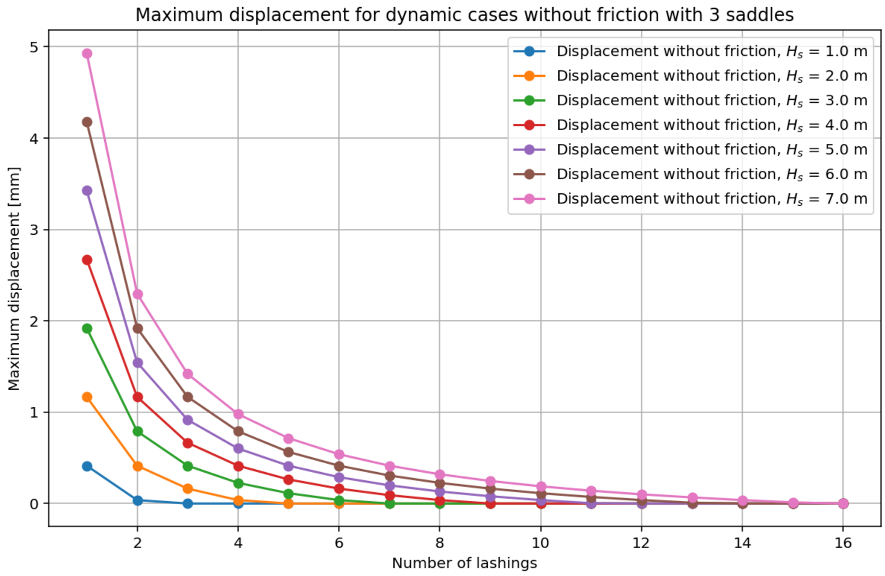

Figure 5.5: Maximum displacement for all lashing configurations for different wave heights without friction

Figure 5.6 gives an overview of the cases with sufficient lashing capacity and when friction is required to prevent the longitudinal motion. For example, for cases with a wave height of 2.0 meters (orange line), friction forces are necessary if less than five lashing wires are used since the lashing capacity is insufficient to prevent the longitudinal motion of the monopile.

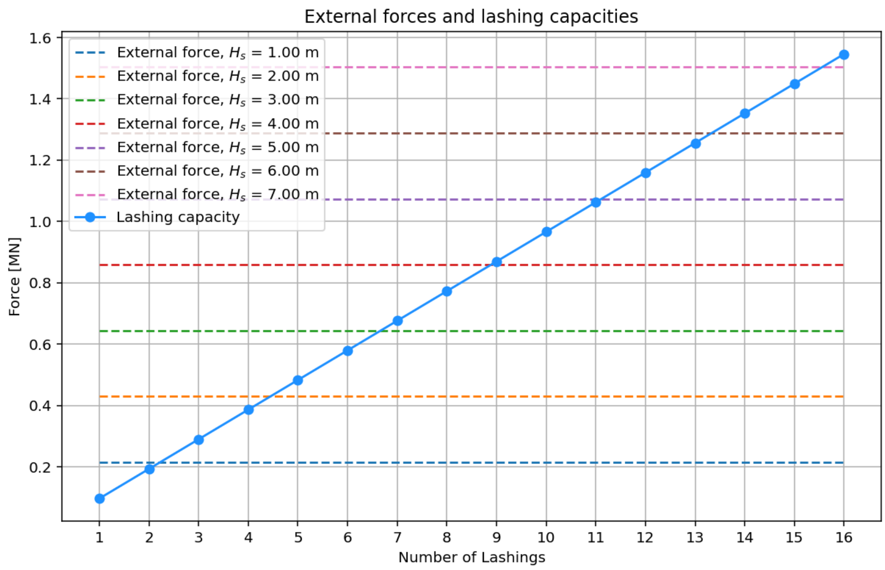

Figure 5.6: Lashing capacity against external forces for all wave heights

5.5. Static analysis with friction

Since no accelerations exist in the static case, the external force F_{ext} is zero. The lashing and friction forces are zero, while the capacity to prevent the longitudinal motion is available. The longitudinal displacement is zero for all static cases. This static analysis showed that the lashing and friction forces are applied correctly; only generating a force if an external force exists.

It should be noted that according to DNV [10], the cargo needs to be sea fastened for $0.1g$ in any direction before moving the vessel to another location at the same site for further seafastening. This is relatable to the static case since the static case only applies in port conditions where no waves occur.

5.6. Dynamic analysis with friction

The dynamic analysis without friction showed that 16 lashing wires are required to prevent motion in the longitudinal direction for all wave heights. This analysis implemented the friction function based on the sliding friction test results to select the friction coefficient that belongs to the normal force for all saddles as given in section 5.2.

Figure 5.7 shows the longitudinal displacement for all combinations of wave heights and number of lashings, including friction. The displacement is zero for all cases when friction is included, which is the defined displacement limit. Zero displacement is ensured by the lashing wires, which are under pre-tension. To maintain this during transport, the crew checks and, if necessary, tightens all chains at least once every 24 hours. Please note that the displacement lines for wave heights lower than 7.0 meters are all plotted behind the pink line with x-markers belonging to a wave height of 7.0 meters.

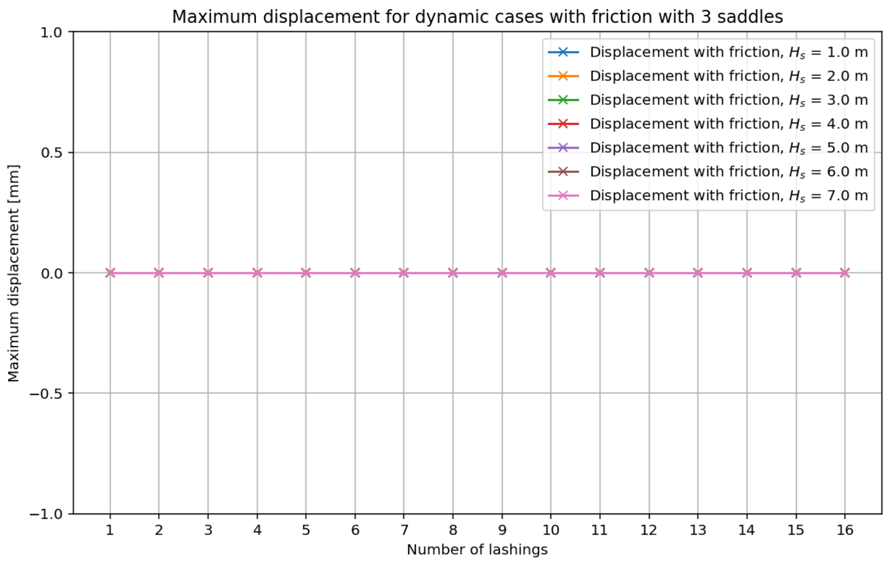

Figure 5.7: Maximum displacement for all lashing configurations for different wave heights with friction

5.7. Revised seafastening arrangement

Figure 5.8 shows the total available friction capacity and the maximum external force on the monopile for all wave heights. This figure shows that 3 saddles provide sufficient friction capacity for all wave heights. Since a configuration with 3 saddles and a wave height of 7.0 meters has the lowest friction capacity relative to the external force (see table 5.2), it can be concluded that other saddle configurations also have sufficient friction capacity. Therefore, no lashing wires have to be applied when friction is considered.

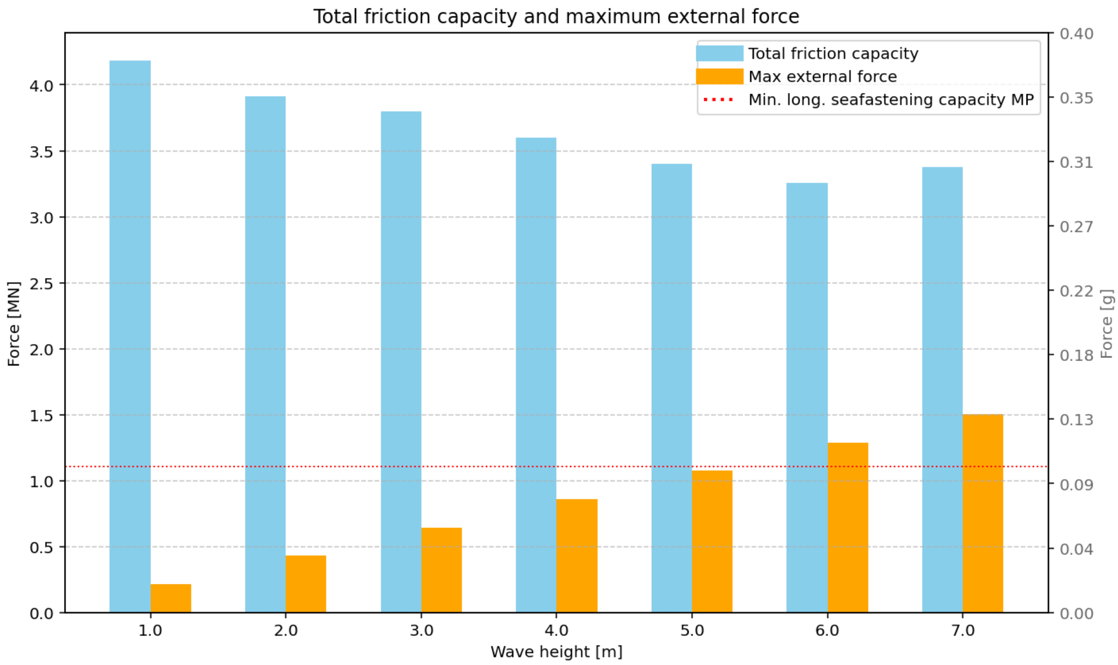

Figure 5.8: Total friction capacity vs the maximum external force for 3 saddles

Wave heigth	Total friction capacity [MN]	Max external force [MN]	UC
1.0	4.186	0.215	0.05
2.0	3.914	0.429	0.11
3.0	3.798	0.644	0.17
4.0	3.601	0.859	0.24
5.0	3.399	1.074	0.32
6.0	3.255	1.288	0.40
7.0	3.377	1.502	0.45

Table 5.2: Unity check between the total friction capacity and the maximum external force for each wave height

5.7.1. Seafastening design loads

Rule [11.9.2.9] of DNV-ST-N001 [10] states that no seafastening is required when the available friction capacity is at least twice the calculated required total seafastening design loads. However, when the friction capacity is less than twice the design loads, the minimum seafastening capacity is determined according to the table of figure 5.9, which gives a function of the design loads based on the cargo weight but does not consider friction. On the right side of figure 5.9, this function is plotted.

Weight:	Longitudinal minimum seafastening capacity
$W < 1000t$	0.10g
$1000t \leq W < 5000t$	Linear
$5000t \leq W < 20000t$	0.05g
$20000t \leq W < 40000t$	Linear
$W \geq 40000t$	0.03g

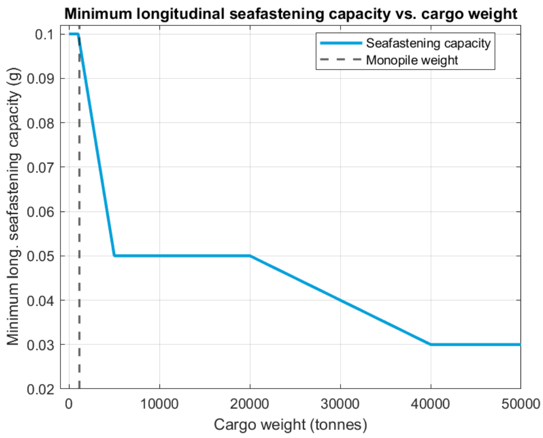

Figure 5.9: Minimum seafastening capacity as a function of cargo weight, W, according to [10]

The minimum longitudinal seafastening capacity for one monopile is given in equation 5.1. This calculation results in the longitudinal force applied on the seafastening. Once the lashing capacity is known, the required number of lashing wires to prevent longitudinal motion can be calculated. In this case, only 12 lashing wires of 10-ton capacity under an angle of 10 degrees are needed to generate enough longitudinal seafastening force. However, according to calculations of Roll Group, 16 lashing wires are required to avoid longitudinal motion caused by the maximum external force if friction is not considered.

$$\begin{aligned} \text{Longitudinal seafastening capacity } &= 0.0981g \\ \text{Longitudinal seafastening force: } F_x &= M_{MP} \cdot a_x \approx 11.3MN \cdot 0.0981g \approx 1.1MN \\ \text{Number of lashings } &= 12 \end{aligned} \tag{5.1}$$

The seafastening design loads are calculated by equation 5.2 and section 5.3 described that the lowest available friction capacity is 3.25 MN. Two times the required calculated total seafastening design load is approximately 3 MN. According to [11.9.2.9] of DNV, no longitudinal seafastening is necessary since the available friction capacity is at least twice the calculated required total seafastening design loads. With this result, the MWS may, on a case-by-case basis, agree to dispense with the minimum seafastening capacity requirements of figure 5.9. In such cases, the entire load path, including the potential sliding surfaces, shall be documented as capable of withstanding twice the larger loadings from the motions analyses and the minimum seafastening capacity requirements.

$$\begin{aligned} \text{Seafastening design loads: } F_x &= M_{MP} \cdot a_x \approx 11.3MN \cdot 0.133g \approx 1.5MN \\ \text{Twice seafastening design loads: } F_x &\approx 3.0MN \\ \text{Available friction capacity } &\geq 3.25MN \end{aligned} \tag{5.2}$$

5.8. Conclusion results

The dynamic deflections of the software GHS showed the most significant deflections for the arrival hogging condition, so these deflections are used in the revised numerical model. This revised numerical model resulted in the normal forces in the saddles for wave heights from 1.0 to 7.0 meters for saddle configurations between 3 and 7 saddles, including loss of contact. Based on the function of the friction coefficient, which depends on the normal force, the friction coefficients in the saddles are calculated, resulting in the friction capacity per saddle. The total friction capacity is calculated by taking the sum of the friction capacities in the saddles.

A dynamic analysis without friction is done to simulate Roll Group's seafastening calculations. Next, a static analysis with friction is done to check if the monopile model worked. For the following analysis, the friction function is included to show the longitudinal displacement of the monopile for the dynamic cases with friction. A last analysis is done to determine the revised seafastening arrangement that entirely prevents the longitudinal displacement of the monopile. DNV states that no seafastening is required when the available friction capacity is at least twice the total required seafastening design loads. Using the calculated accelerations of the software Octopus, it turns out that twice the seafastening design loads are lower than the available friction capacity in the saddles for saddle configurations from 3 up to 7 saddles and wave heights up to 7.0 meters. It can be concluded that the analysis based on the friction theory shows that no seafastening is required to prevent the longitudinal motion of the monopile for all saddle and wave height configurations. However, the rules of DNV state that the marine warranty surveyor may, on a case-by-case basis, agree to dispense with the minimum seafastening capacity requirements. This means that this research does not guarantee that the seafastening arrangement can be reduced.

6 Conclusion

This chapter concludes the research by answering the sub-questions and the main research question.

1. **Modelling:**
How can a system of a monopile exposed to longitudinal forces caused by ship motions be modelled to define the effect of friction as seafastening?

The system of a monopile exposed to longitudinal forces caused by vessel motions can be modelled as a mass-spring system. In this model, the mass acts as a rigid body, to which an external force is applied with a magnitude based on the accelerations caused by the vessel's heave and pitch motion. Friction force counteracts the external force, and its magnitude corresponds with the normal force and friction coefficient. The friction coefficient is related to the contact pressure, which depends on the normal forces and surface areas of the seafastening system. In case the total friction capacity of the saddles is less than the applied external force, additional lashing wires are applied.

2. **Friction:**
How does the varying contact pressure due to the vessel's deflection affect the friction between the monopile and its saddles?

The varying contact pressure affects friction in two ways. First, a varying contact pressure due to dynamic vessel deflections means the normal force varies since the support pad area remains the same, and the total friction capacity depends on the normal force ($F_{friction} = \mu \cdot F_N$). Second, the sliding friction tests showed that the coefficient of friction depends on the contact force, and a friction coefficient function is defined. In this function, the friction coefficient decreases for increasing contact forces until a friction coefficient of 0.3 is reached, and the friction coefficient remains constant at 0.3 for higher normal forces. This means that with a changing contact pressure due to the vessel's deflection, both the normal force and the coefficient of friction change, resulting in a changing friction capacity.

3. **Number of saddles:**
How does a varying number of saddles affect the friction capacity?

The total friction capacity for all wave heights from 1.0 to 7.0 meters and the number of saddles from 3 to 7 is analysed with the longitudinal monopile model, including the friction function and intermittent contact cases. This analysis showed that the total friction capacity for most saddle configurations decreases with increasing wave heights but increases for an increasing number of saddles. Higher wave heights result in larger vertical dynamic deflections of the vessel, resulting in higher normal forces in some saddles and loss of contact in other saddles. Since higher normal forces correspond to lower friction coefficients and loss of contact means no friction capacity, the total friction capacity decreases for higher wave heights. Once the number of saddles increases, the normal force is distributed over more saddles, resulting in higher friction coefficients per saddle, so the total friction capacity is higher when more saddles are used. Despite these findings, the dynamic analysis including friction, showed that the total friction capacity is sufficient to prevent the longitudinal motion caused by vessel motions without applying lashing wires for all dynamic analyses.

In conclusion, an increasing number of saddles increases the total friction capacity since the friction coefficient per saddle is higher. Still, all saddle configurations prevent the longitudinal motion of the monopile for all wave heights. In addition, the case with three saddles and a wave height of 7.0 meters resulted in the lowest available friction capacity relative to the external force. In this case, the first saddle lost contact, and the third saddle almost lost contact, resulting in a high normal force in the middle saddle. Since the friction capacity of this case is sufficient to prevent the longitudinal motion, it is concluded that the monopiles of this research can be seafastened on one friction-based saddle, given that the contact with the saddle is guaranteed and both the saddle and the deck are able to withstand the friction forces.

4. **Practical application:**
How would the seafastening system be changed in Roll Group's previous monopile transportation projects if friction was considered?

The dynamic analysis, including friction, showed that the available friction capacity is sufficient to prevent the monopile from relative longitudinal displacement without lashing wires for all saddle configurations and all wave heights. In other words, the monopiles considered in this specific research can be seafastened solely with friction. This means that, according to theory, all lashing wires applied in previous projects (with the same set-up) were redundant.

However, the minimum longitudinal seafastening capacity should meet the requirements of DNV-ST-N001. This requirement follows a function of the minimum longitudinal seafastening capacity depending on the cargo weight without considering friction, resulting in 12 lashing wires at each side of one monopile. However, calculations of the seafastening design loads, based on the maximum external force, show that 16 lashing wires are required to prevent longitudinal motion without considering friction.

If the calculation does consider friction, the available friction capacity should be at least twice the required total seafastening design loads to make the marine warranty surveyor, on a case-by-case basis, dispense with the minimum seafastening capacity requirements. The case of this research does comply with that requirement, so the monopile can be friction-based sea fastened if the MWS company dispense with the requirements and if the captain of the vessel also agrees with the calculations and the friction-based seafastening. These two parties are expected to be the limiting factor in friction-based seafastening as a new seafastening system for monopile transportation projects.

"How does friction between a monopile and its saddles affect the seafastening arrangement of a monopile?"

In this research case, the friction between the monopile and its saddles affects the seafastening arrangement of a monopile by making the applied lashing wires redundant. For all saddle configurations from 3 to 7 saddles and all wave heights from 1.0 to 7.0 meters, the friction capacity is sufficient to prevent the longitudinal motion of the monopile without considering lashing wires. The limiting factors of this outcome are the marine warranty surveyor and the captain, who both have to agree with the new friction-based seafastening system.

7
Discussion & Recommendations

This chapter represents the discussions on the research, divided into the topics of the sub-questions, and gives recommendations for further research.

1. **Modelling**
    - Normal forces:
      The revised coupled fluid-ship model calculates the normal forces between the saddles and the monopile. However, the results already showed that the total static forces for all saddle configurations do not equal 11.3 MN, which is the mass of the monopile, because a force representing gravity is subtracted for each saddle. The subtraction of the gravity force results in a lower sum of normal forces in the saddles when loss of contact occurs. This research could not trace this subtraction back to the original coupled fluid-ship model, so after consultation, it is decided to assume this is correct in this research.

      For further research, it is recommended that this subtraction be traced back to check if this is correct. Incorrect normal forces would affect the friction capacity for each saddle configuration and wave height, so the revised seafastening arrangement could be affected.
    - Phases of the normal forces:
      This research assumes that the forces between the monopile and the saddles, calculated with the revised coupled fluid-ship model, are in phase. This assumption is made since the forces are calculated during the same dynamic deflection state of the vessel. It is recommended to check if the normal forces in the revised coupled fluid-ship model are real or complex numbers. If they are complex, the imaginary part can trace the phase. This answers the question of whether the correct normal forces are being used.
    - Full wave cycle:
      The arrival hogging case is the governing deflection case, and these deflections are used to find the highest normal forces and the intermittent contact cases. It is assumed that the seafastening arrangement resulting from the governing deflection case also works for all other dynamic deflection cases. With fewer deflections, the forces are more evenly distributed over the saddles, resulting in a higher total friction capacity.

      During the sagging cases, the normal forces are expected to be divided over different saddles with different magnitudes, resulting in a total friction capacity sufficient to prevent longitudinal motions. However, it is recommended that the total friction capacity for the departure sagging case, which is the governing sagging case, is calculated in further research. This would show the variation of normal forces over the entire wave cycle, and based on those normal forces, the friction capacity throughout the whole wave cycle can be calculated. These results could affect the revised seafastening arrangement.

2. **Friction**

- Static friction regime:
The goal of the seafastening of the monopile is to prevent all longitudinal motions of the monopile. This aim led to the selection of the static friction regime of the third test when determining the friction coefficient since these test results have a clear transition from static to kinetic friction for the lower normal forces. However, the static friction limit for the first two tests does not correspond to the values of the third test, which is used. Due to time constraints, only three sets of tests were performed, but for further research, it is recommended that more tests with the same properties be performed to check if the static friction limit of the third test is correct.

  Moreover, the static friction limit for higher normal forces is hard to determine since there is no clear transition from the static to the kinetic regime. Here, assumptions are made by selecting the highest point of the initiation lines as the kinetic friction coefficient and the static friction coefficient is taken as 90% of the kinetic friction coefficient. Finding a solution to reduce the slip process is useful to see a clear transition with a static friction coefficient for higher normal forces. Possible solutions are increasing the test specimen area or decreasing the height of the current specimens. This could provide a more accurate static friction coefficient for higher normal forces.

- Shearing effects:
The discussion item about the static friction regime mentioned the slip process during testing; this results from the shearing effects of the support pad material. Since the length-height ratio of the test specimen is twelve times smaller than the length-height ratio of the saddle support pad, the shearing effects are neglected in the longitudinal monopile model. The solutions provided in the static friction regime item would also result in a better understanding of the shearing effect of EPDM70. With these results, it can be verified whether neglecting the shearing effects is valid. The best solution to investigate the shearing effects on the saddle scale would be to test on full saddle scale, which is a practical challenge.

- Contact area:
The test specimen's geometric contact area is 300 mm^2, and the final friction function is scaled to the saddle scale based on this geometric contact area. Nevertheless, this is a conservative assumption since the actual contact area is expected to be much smaller, resulting in higher contact pressures. It is unclear what the actual contact area on the saddle scale is and how it affects the friction resistance. Once the contact pressure becomes too high, the rubber can start to yield. In this case, the contact area of the saddle should be increased by increasing the size of the saddle-support pad or adding a saddle to decrease the contact pressure. It is recommended that the yield behaviour of the support material and the actual contact area be investigated further. Based on this additional research, the number of saddles should be analysed again, incorporating the maximum allowable saddle pressure.

- Extrapolating test results to saddle scale:
The friction function based on the normal force is created with test results of small normal forces, and this function is scaled to a friction function based on the normal forces in the saddles. However, the validity of this scaling is uncertain since the friction coefficients on the saddle scale are unknown. Nevertheless, the guidelines of DNV-ST-N001 give a friction coefficient of 0.3, and no distinction is made between the normal forces. Investigating the friction capacity if the friction coefficient remains 0.3 for all normal forces is recommended. If the friction capacity remains sufficient to prevent the longitudinal motion of the monopile, it is recommended to investigate until which friction coefficient the friction capacity remains sufficient.

  Moreover, the current friction function is based on one set of test results, and as described in this report, many assumptions are made during this process. Therefore, it is recommended that more tests for the same case be conducted to see if the new test results match the current friction function. Once one parameter changes compared to this research, new tests should be performed, and the results must be implemented in the longitudinal friction model to investigate the revised seafastening arrangement.

3. **Number of saddles**
   - Position of saddles:
     During this research, the deck construction is not considered when determining the distance between the saddles, but the distance is tried to be kept equally divided. For further research, it is recommended always to use saddle locations that match the strong points of the vessel's deck when analysing the total friction capacity. The normal forces in the saddles depend on the location, and so does the friction capacity of the saddle. Changing the location of the saddles can affect the total friction capacity, so it should be analysed if this affects the seafastening arrangement.
4. **Practical application**
   - Seafastening to prevent up-lift:
     This research showed that the available friction capacity remains sufficient for all wave heights to prevent longitudinal motion, and the cases with intermittent contact were defined. Since the focus was on the longitudinal seafastening, no checks were done on the vertical seafastening. It is recommended that further research be conducted to determine if the mass of the monopile is sufficient to prevent up-lift forces or if the monopile should be seafastened in the vertical direction.

References

[1] Billy Leibundgut. “Wave height predictions using ARIMA, Prophet, and XGBoost”. In: *Towards-DataScience* (Nov. 2020). URL: https://towardsdatascience.com/wave-height-prediction-using-arima-prophet-and-xgboost-b7ddc8a1bdd.

[2] Yutaka Tanaka. “Active vibration compensator on moving vessel by hydraulic parallel mechanism”. In: *International Journal of Hydromechatronics* 1 (Dec. 2018), p. 350. DOI: 10.1504/IJHM.2018.094887.

[3] Nurman Firdaus and Baharuddin Ali. “Experimental Study of the Probability Distributions on the Seakeeping Performance of Monohull and Catamaran Design”. In: (Dec. 2017), pp. 1–5.

[4] Linus Fagerberg. “Wrinkling in sandwich panels for marine applications”. In: (Dec. 2003).

[5] Rebecca Williams and Feng Zhao. *Global offshore wind report 2023*. Tech. rep. Brussels: Global Wind Energy Council, Aug. 2023. URL: www.gwec.net.

[6] Anke Marij and) Elzinga. *Operational limits of 2XL monopile installation A comparative analysis of side and stern installation*. Tech. rep. Delft: University of Technology Delft, Mar. 2024. URL: https://repository.tudelft.nl/.

[7] CJ George, C Varghese, and F Kamal. “Offshore WTG Monopile Installation–Crane Vessel Preparation”. In: *Abu Dhabi International Petroleum Exhibition and Conference* (Oct. 2023).

[8] D Mikail and M Teunis. *Ship-cargo Interaction for Vessels Carrying Large Wind Turbine Monopiles*. Tech. rep. 2022.

[9] Bart Schrijvers. *Friction-based monopile sea fastening*. Tech. rep. Rotterdam: Delft University of Technology, 2022.

[10] DNV AS. *DNV-ST-N001 Marine operations and marine warranty*. Tech. rep. 2023, pp. 307–309.

[11] Alexandre Mathern, Christoph von der Haar, and Steffen Marx. *Concrete support structures for offshore wind turbines: Current status, challenges, and future trends*. Apr. 2021. DOI: 10.3390/en14071995.

[12] Ki Yong Oh et al. *A review of foundations of offshore wind energy convertors: Current status and future perspectives*. May 2018. DOI: 10.1016/j.rser.2018.02.005.

[13] A D Speksnijder. “Ship-cargo interaction for large and stiff cargo”. PhD thesis. Delft: Delft University of Technology, Dec. 2023. URL: http://repository.tudelft.nl/.

[14] Tribology ABC. *History of science friction*. URL: https://www.tribology-abc.com/abc/history.htm.

[15] Peter Dr. Korondi et al. *Robot Applications - Models of Friction*. 2014. URL: https://mogi.bme.hu/TAMOP/robot_applications/ch07.html.

[16] Klaus Friedrich. *Friction and wear of polymer composites*. Hamburg: Elsevier, 1986.

[17] H. Olsson et al. “Friction models and friction compensation”. In: *European Journal of Control* (1998), pp. 176–195.

[18] James H Dieterich. *Time-Dependent Friction and the Mechanics of Stick-Slip*. Tech. rep. 1978.

[19] Chris Marone. *The effect of loading rate on static friction and the rate of fault healing during the earthquake cycle*. Tech. rep. 1998.

[20] Q Jane Wang and Yip-Wah Chung. *Encyclopedia of Tribology*. Tech. rep.

[21] Andrei Tudor et al. “Dynamic friction in coulombian rubber damper at low velocities”. In: *U.P.B. Sci. Bull., Series D* 80.1 (2018). ISSN: 1454-2358. URL: https://www.researchgate.net/publication/323720268.

[22] Circuit Globe. *Difference between static and kinetic friction*. Nov. 2020. URL: https://circuitglobe.com/difference-between-static-and-kinetic-friction.html.

[23] GeeksforGeeks. *Factors Affecting Friction*. Jan. 2022. URL: https://www.geeksforgeeks.org/factors-affecting-friction/.

[24] Santiago Casado. “Studying friction while playing the violin: Exploring the stick-slip phenomenon”. In: *Beilstein Journal of Nanotechnology* 8.1 (2017), pp. 159–166. ISSN: 21904286. DOI: 10.3762/bjnano.8.16.

[25] Caishan Yan et al. “Statistical laws of stick-slip friction at mesoscale”. In: *Nature Communications* 14.1 (Dec. 2023). ISSN: 20411723. DOI: 10.1038/s41467-023-41850-1.

[26] Peter J Blau. *The significance and use of the friction coefficient*. Tech. rep. Oak Ridge: Oak Ridge National Laboratory, 2001, pp. 585–591. URL: www.elsevier.com/locate/triboint.

[27] R.T. Spurr. “THE FRICTION OF POLYMERS”. In: *Wear*. Vol. 79. Elsevier Sequoia, Dec. 1981. Chap. 79, pp. 301–310.

[28] Nikolay Stoimenov et al. “Static and Kinetic Friction of 3D Printed Polymers and Composites”. In: *Tribology in Industry* 46.1 (Mar. 2024), pp. 97–106. ISSN: 03548996. DOI: 10.24874/ti.1546.08.23.10.

[29] Joel Voyer et al. “Static and dynamic friction of pure and friction-modified PA6 polymers in contact with steel surfaces: Influence of surface roughness and environmental conditions”. In: *Lubricants* 7.2 (2019). ISSN: 20754442. DOI: 10.3390/lubricants7020017.

[30] Guibin Tan et al. “Frictional behaviors of rough soft contact on wet and dry pipeline surfaces: With application to deepwater pipelaying”. In: *Science China Technological Sciences* 56.12 (Oct. 2013), pp. 3024–3032. ISSN: 18691900. DOI: 10.1007/s11431-013-5398-8.

[31] C. Putignano, T. Reddyhoff, and D. Dini. “The influence of temperature on viscoelastic friction properties”. In: *Tribology International* 100 (Aug. 2016), pp. 338–343. ISSN: 0301-679X. DOI: 10.1016/J.TRIBOINT.2016.03.018.

[32] Labthink. *Influence of Temperature on Coefficient of Friction*. Jan. 2013. URL: https://en.labthink.com/en-us/literatures/material-friction-coefficient-and-temperature.html.

[33] M. Stembalski, P. Preś, and W. Skoczyński. “Determination of the friction coefficient as a function of sliding speed and normal pressure for steel C45 and steel 40HM”. In: *Archives of Civil and Mechanical Engineering* 13.4 (Dec. 2013), pp. 444–448. ISSN: 16449665. DOI: 10.1016/j.acme.2013.04.010.

[34] D. M. Neto et al. “Study of the frictional contact conditions in the hole expansion test”. In: *Journal of Physics: Conference Series*. Vol. 1063. 1. Institute of Physics Publishing, Aug. 2018. DOI: 10.1088/1742-6596/1063/1/012139.

[35] Yilong Ren et al. *A review on tribology of polymer composite coatings*. June 2021. DOI: 10.1007/s40544-020-0446-4.

[36] F P Bowden and D Tabor. “Friction, lubrication and wear: a survey of work during the last decade”. In: *British Journal of Applied Physics* 17.12 (July 1996).

[37] Roll Group. *Pictures monopile transport*. Capelle a.d. IJssel.

[38] Roll Group. *MC-class vessel specifications*.

[39] Xiaoyang Cheng et al. “3d fe-informed laboratory soil testing for the design of offshore wind turbine monopiles”. In: *Journal of Marine Science and Engineering* 9.1 (Jan. 2021), pp. 1–15. ISSN: 20771312. DOI: 10.3390/jmse9010101.

[40] Dan Dumitriu, Tudor Sireteanu, and Daniel Baldovin. *NUMERICAL SIMULATION OF THE VERTICAL INTERACTION BETWEEN RAILWAY VEHICLE AND TRACK*. Tech. rep. URL: https://www.researchgate.net/publication/267202466.

[41] AkzoNobel. *Interzinc ® 22 Anorganische Zinkrijke Silicaat*. Tech. rep. URL: www.international-pc.com,.

[42] Gumalit-Haas. “Rubber plate EPDM 70 - Material parameters”. In: ().

[43] World Steel Association AISBL. *Coating friction*. Mar. 2021. URL: https://ahssinsights.org/coatings/coating-friction/.

[44] Sheng Dong et al. *Experimental Characterization and Modeling Application*. Tech. rep. June 2016.

A

Appendix A

No. of saddles:	Saddle location:						
3	$\frac{L}{5}$	$\frac{L}{2}$	$\frac{4L}{5}$				
4	$\frac{L}{5}$	$\frac{2L}{5}$	$\frac{3L}{5}$	$\frac{4L}{5}$			
5	$\frac{L}{6}$	$\frac{2L}{6}$	$\frac{L}{2}$	$\frac{4L}{6}$	$\frac{5L}{6}$		
6	$\frac{L}{8}$	$\frac{2L}{7}$	$\frac{3L}{7}$	$\frac{4L}{7}$	$\frac{5L}{7}$	$\frac{7L}{8}$	
7	$\frac{L}{8}$	$\frac{2L}{8}$	$\frac{3L}{8}$	$\frac{L}{2}$	$\frac{5L}{8}$	$\frac{6L}{8}$	$\frac{7L}{8}$

Table A.1: Saddle locations for all configurations

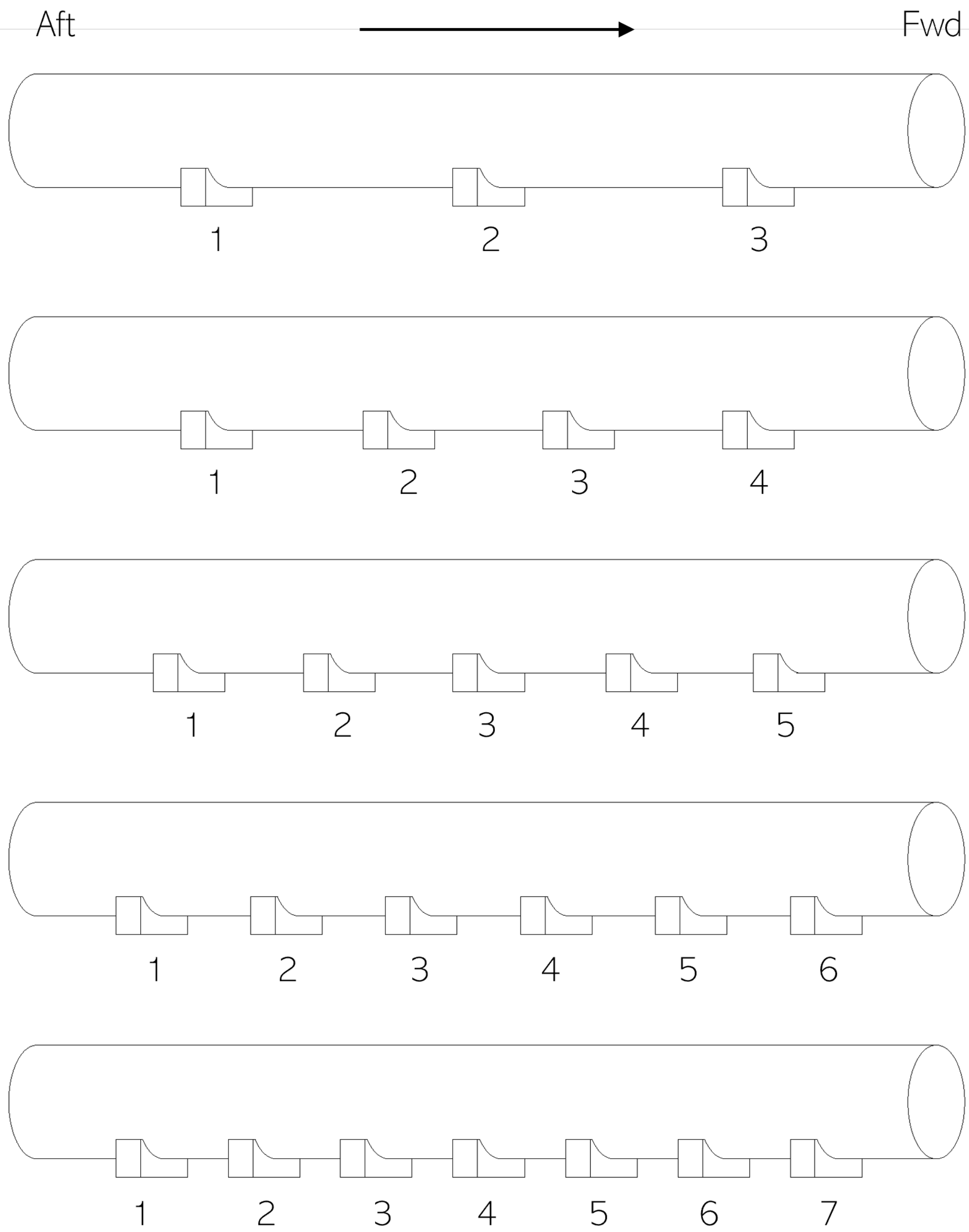

Figure A.1: Schemtic overview of saddle configurations from 3 to 7 saddles

B

Appendix B

The differences expressed in percentages between the deflection results of GHS and the linearization with the use of equation 3.3 are shown in figure B.1. After defining 3 ranges for the wave height, and generating equations (3.4) to (3.6), the differences became smaller compared to the original calculation with 1 linearization function. The results of the differences between the deflection of GHS and the equations (3.4) to (3.6) are shown in figure B.2. All differences below or equal to 5% are green, and all differences larger than 5% are red. From these results, it can be concluded it is more accurate to use 3 ranges when calculating the deflections of the vessel since there are only three differences which are larger than 5%, and these differences are still small compared to the original calculation.

	Difference between deflections GHS and linearization with one equation													
Hs	0.5	1.0	1.5	2.0	2.5	3.0	3.5	4.0	4.5	5.0	5.5	6.0	6.5	7.0
ζ_a	0.25	0.50	0.75	1.00	1.25	1.50	1.75	2	2.25	2.50	2.75	3	3.25	3.5
FR0	0%	0%	0%	0%	0%	0%	0%	0%	0%	0%	0%	0%	0%	0%
FR10	26%	22%	21%	20%	20%	19%	18%	17%	16%	14%	13%	11%	10%	8%
FR20	23%	19%	18%	17%	16%	16%	15%	14%	12%	11%	9%	8%	6%	5%
FR30	22%	18%	16%	16%	15%	15%	14%	12%	11%	10%	8%	6%	5%	3%
FR40	22%	18%	17%	16%	16%	15%	14%	13%	12%	10%	9%	7%	6%	4%
FR50	21%	17%	15%	14%	14%	13%	13%	11%	10%	8%	7%	5%	4%	2%
FR60	21%	17%	16%	15%	14%	14%	13%	12%	10%	9%	7%	6%	4%	3%
FR70	21%	17%	16%	15%	15%	14%	13%	12%	11%	9%	8%	7%	5%	3%
FR80	20%	17%	15%	14%	14%	14%	13%	12%	10%	9%	7%	6%	5%	3%
FR90	20%	16%	14%	14%	13%	13%	12%	11%	9%	8%	7%	5%	4%	2%
FR100	19%	16%	14%	13%	13%	13%	12%	11%	9%	8%	7%	5%	4%	2%
FR110	19%	16%	14%	14%	13%	13%	12%	11%	9%	8%	7%	6%	4%	3%
FR120	18%	15%	13%	12%	12%	12%	11%	10%	8%	7%	6%	4%	3%	2%
FR130	19%	15%	13%	13%	12%	12%	11%	10%	9%	8%	6%	5%	4%	2%
FR140	18%	15%	13%	13%	12%	12%	11%	10%	9%	7%	6%	5%	3%	2%
FR150	18%	14%	13%	12%	12%	12%	11%	10%	8%	7%	6%	5%	3%	2%
FR160	18%	14%	13%	12%	12%	12%	11%	10%	8%	7%	6%	4%	3%	2%
FR170	18%	14%	13%	12%	12%	12%	11%	10%	8%	7%	6%	5%	3%	2%
FR180	18%	15%	13%	13%	13%	12%	12%	10%	9%	8%	6%	5%	4%	2%
FR190	18%	14%	13%	12%	12%	12%	11%	10%	8%	7%	6%	4%	3%	1%
FR200	19%	16%	14%	14%	14%	14%	13%	12%	10%	8%	7%	6%	5%	3%
FR210	20%	16%	15%	14%	14%	14%	13%	12%	10%	9%	7%	6%	5%	3%
FR220	21%	17%	16%	16%	16%	15%	15%	13%	11%	10%	9%	7%	6%	5%
FR230	23%	20%	19%	18%	18%	18%	17%	16%	14%	12%	11%	10%	9%	7%
FR240	25%	21%	20%	20%	20%	19%	19%	17%	15%	13%	12%	11%	10%	8%
FR250	30%	27%	25%	25%	25%	25%	24%	22%	20%	18%	17%	16%	15%	14%
FR260	36%	33%	32%	32%	32%	31%	30%	28%	25%	24%	23%	22%	21%	20%
FR270	52%	50%	49%	49%	49%	49%	48%	45%	42%	41%	40%	39%	39%	38%
FR280	0%	0%	0%	0%	0%	0%	0%	0%	0%	0%	0%	0%	0%	0%

Figure B.1: Differences between GHS and linearization with 1 range

	Difference between deflections GHS and linearization in three ranges													
Hs	0.5	1.0	1.5	2.0	2.5	3.0	3.5	4.0	4.5	5.0	5.5	6.0	6.5	7.0
ζ_a	0.25	0.50	0.75	1.00	1.25	1.50	1.75	2	2.25	2.5	2.75	3	3.25	3.5
FR0	0%	0%	0%	0%	0%	0%	0%	0%	0%	0%	0%	0%	0%	0%
FR10	4%	0%	-2%	-3%	3%	2%	1%	0%	-2%	3%	2%	0%	-2%	-4%
FR20	5%	0%	-2%	-3%	3%	2%	1%	0%	-2%	3%	2%	0%	-2%	-4%
FR30	5%	0%	-2%	-3%	3%	2%	1%	0%	-2%	3%	2%	0%	-2%	-4%
FR40	5%	0%	-2%	-3%	3%	2%	1%	0%	-2%	3%	2%	0%	-2%	-3%
FR50	5%	0%	-2%	-3%	3%	2%	1%	0%	-2%	3%	2%	0%	-2%	-3%
FR60	5%	0%	-2%	-3%	3%	2%	1%	0%	-2%	3%	2%	0%	-2%	-3%
FR70	5%	0%	-2%	-3%	3%	2%	1%	0%	-2%	3%	2%	0%	-2%	-3%
FR80	5%	0%	-2%	-3%	3%	2%	1%	0%	-2%	3%	1%	0%	-2%	-3%
FR90	5%	0%	-2%	-3%	3%	2%	1%	0%	-2%	3%	1%	0%	-1%	-3%
FR100	4%	0%	-2%	-3%	3%	2%	1%	0%	-2%	3%	1%	0%	-1%	-3%
FR110	4%	0%	-2%	-3%	3%	2%	1%	0%	-2%	3%	1%	0%	-1%	-3%
FR120	4%	0%	-2%	-3%	3%	2%	1%	0%	-2%	3%	1%	0%	-1%	-3%
FR130	4%	0%	-2%	-2%	2%	2%	1%	0%	-2%	3%	1%	0%	-1%	-3%
FR140	4%	0%	-2%	-2%	2%	2%	1%	0%	-2%	3%	1%	0%	-1%	-3%
FR150	4%	0%	-2%	-2%	2%	2%	1%	0%	-2%	3%	1%	0%	-1%	-3%
FR160	4%	0%	-2%	-2%	2%	2%	1%	0%	-2%	3%	1%	0%	-1%	-3%
FR170	4%	0%	-2%	-2%	2%	2%	1%	0%	-2%	3%	1%	0%	-1%	-3%
FR180	4%	0%	-2%	-2%	2%	2%	1%	0%	-2%	3%	1%	0%	-1%	-3%
FR190	4%	0%	-2%	-2%	3%	2%	1%	0%	-2%	3%	1%	0%	-1%	-3%
FR200	4%	0%	-2%	-2%	3%	2%	1%	0%	-2%	3%	1%	0%	-1%	-3%
FR210	4%	0%	-2%	-2%	3%	2%	2%	0%	-2%	3%	1%	0%	-1%	-3%
FR220	4%	0%	-2%	-2%	3%	3%	2%	0%	-2%	3%	1%	0%	-1%	-3%
FR230	4%	0%	-2%	-2%	3%	3%	2%	0%	-2%	3%	1%	0%	-1%	-3%
FR240	4%	0%	-2%	-2%	3%	3%	2%	0%	-3%	3%	1%	0%	-1%	-3%
FR250	4%	0%	-2%	-2%	4%	4%	2%	0%	-3%	3%	1%	0%	-1%	-3%
FR260	4%	0%	-2%	-2%	5%	4%	3%	0%	-4%	3%	1%	0%	-1%	-3%
FR270	4%	0%	-2%	-2%	7%	6%	4%	0%	-6%	2%	1%	0%	-1%	-3%
FR280	0%	0%	0%	0%	0%	0%	0%	0%	0%	0%	0%	0%	0%	0%

Figure B.2: Differences between GHS and linearization with 3 ranges

C

Appendix C

	Characteristic	Unit	Value	Test method
1	Material	-	EPDM	-
2	Colour	-	black	-
3	Hardness	°ShA	70 +/- 5	PN-C-04238:1980
4	Density	g/cm^3	Max. 1,25-1,30	PN-ISO 2781
5	Elongation at break	%	min. 200-250	PN-ISO 37
6	Tensile strength	MPa	min. 5	PN-ISO 37
7	Compression set at 100°C / 24h	%	60	PN-ISO 815
8	Heat aging in air at 100°C / 72 h ΔTSb ΔEb ΔH	-	 +/- 30 - 50 +/- 10	PN-ISO 188
9	Brittle temperature	°C	-40	PN-ISO 812

Table C.1: Technical parameters EPDM 70 [42]

D
Appendix D

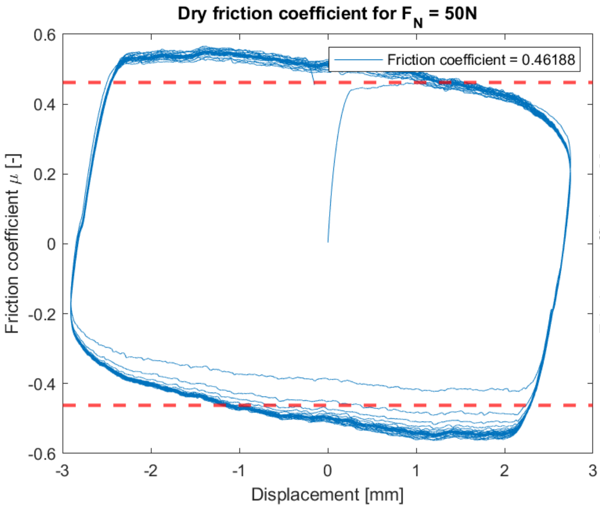

Figure D.1: Dry friction F_N = 50 N

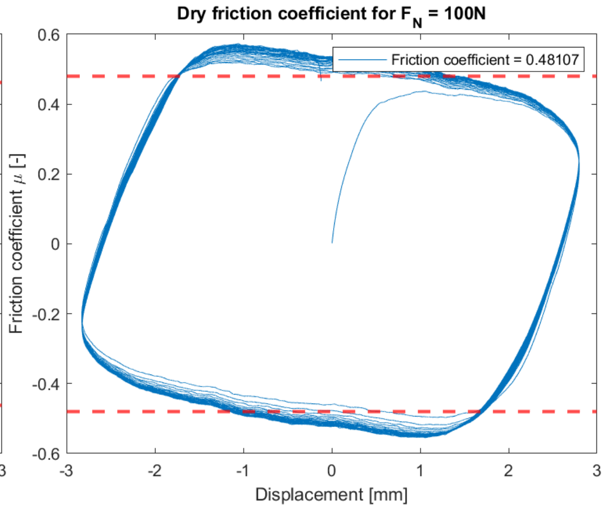

Figure D.2: Dry friction F_N = 100 N

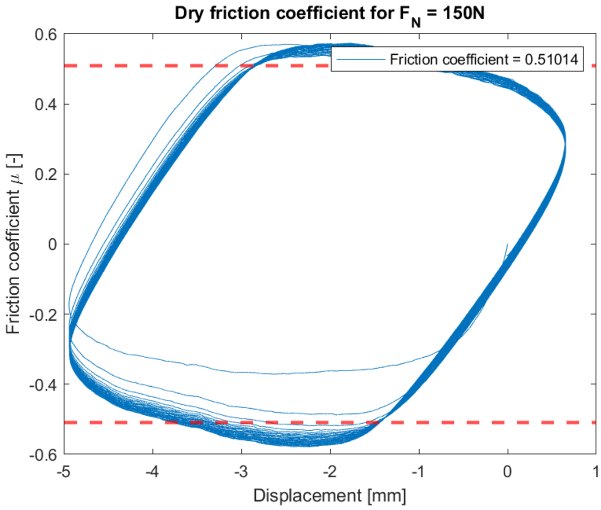

Figure D.3: Dry friction F_N = 150 N

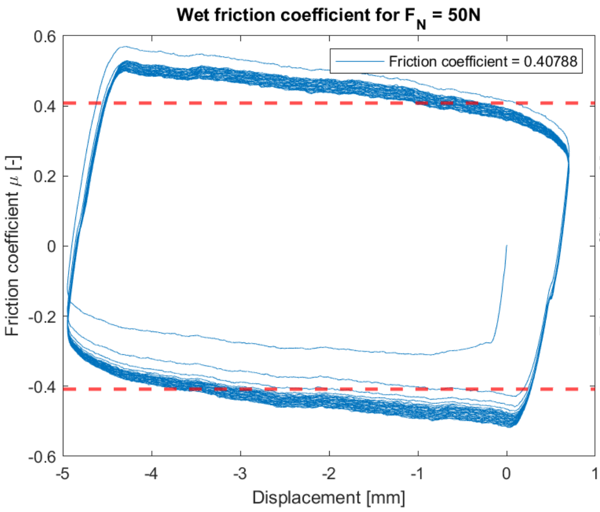

Figure D.4: Wet friction F_N = 50 N

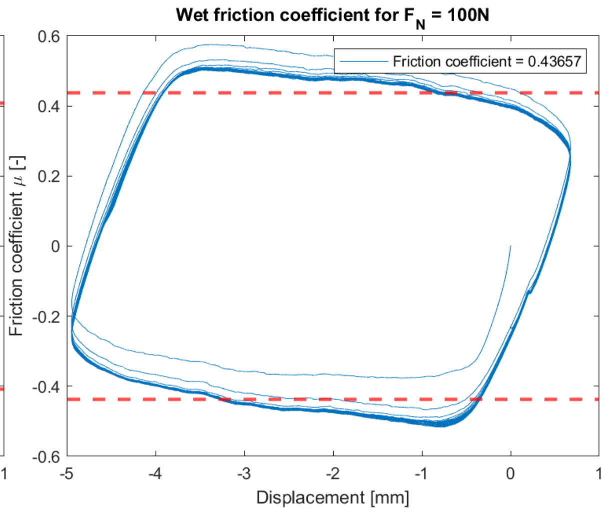

Figure D.5: Wet friction F_N = 100 N

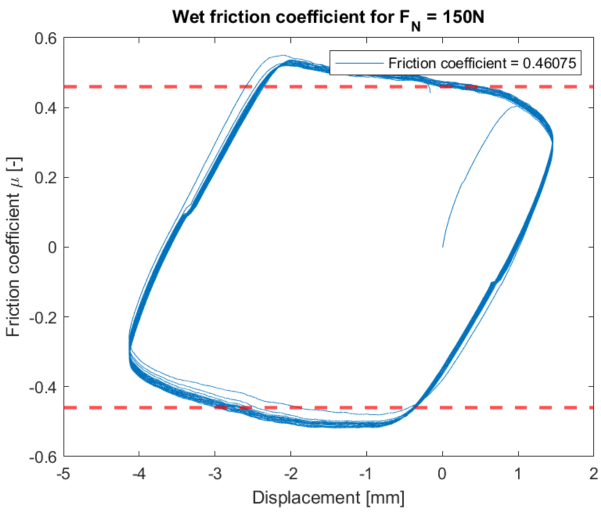

Figure D.6: Wet friction F_N = 150 N

E
Appendix E

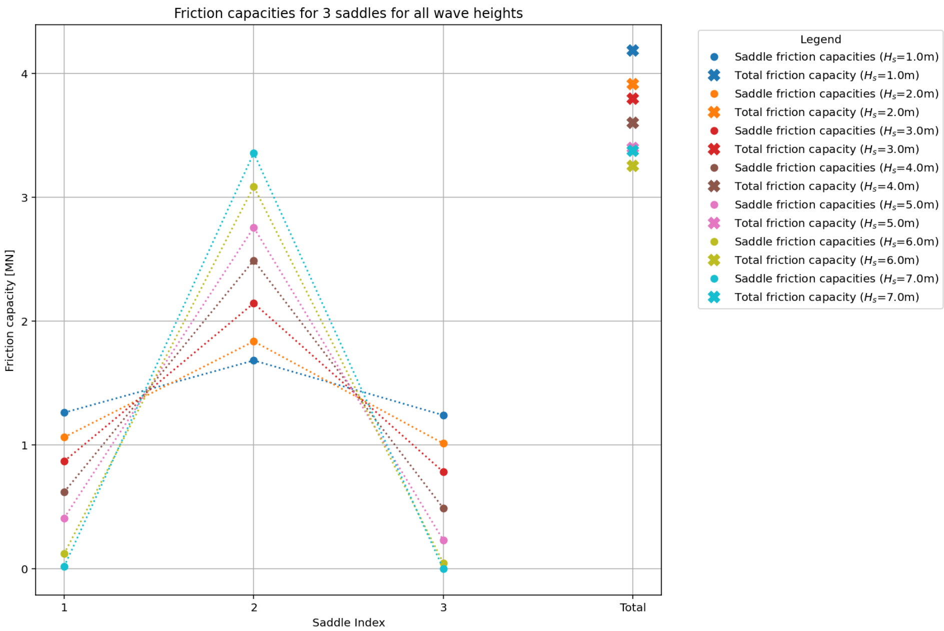

Figure E.1: Friction forces in 3 saddles

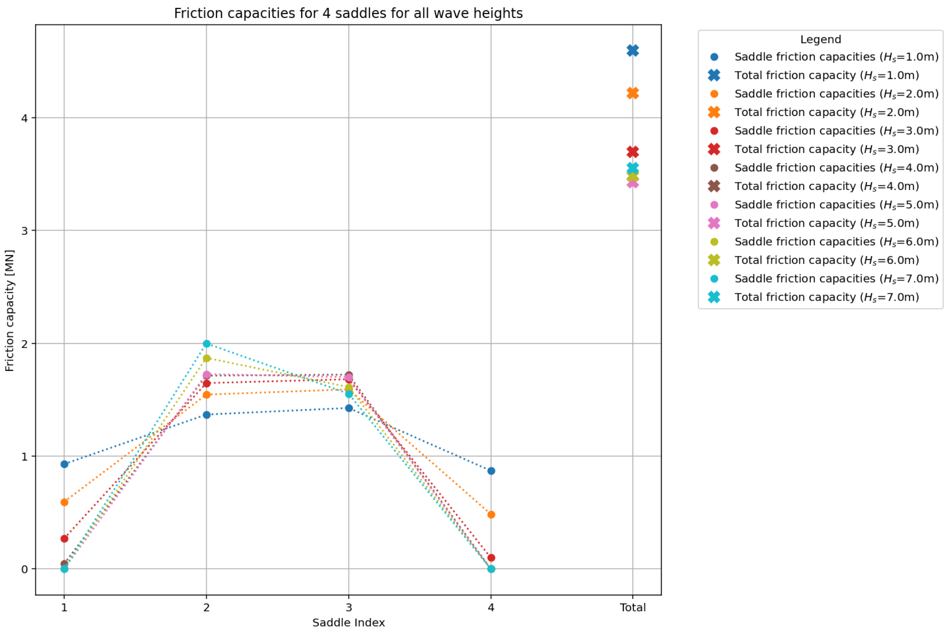

Figure E.2: Friction forces in 4 saddles

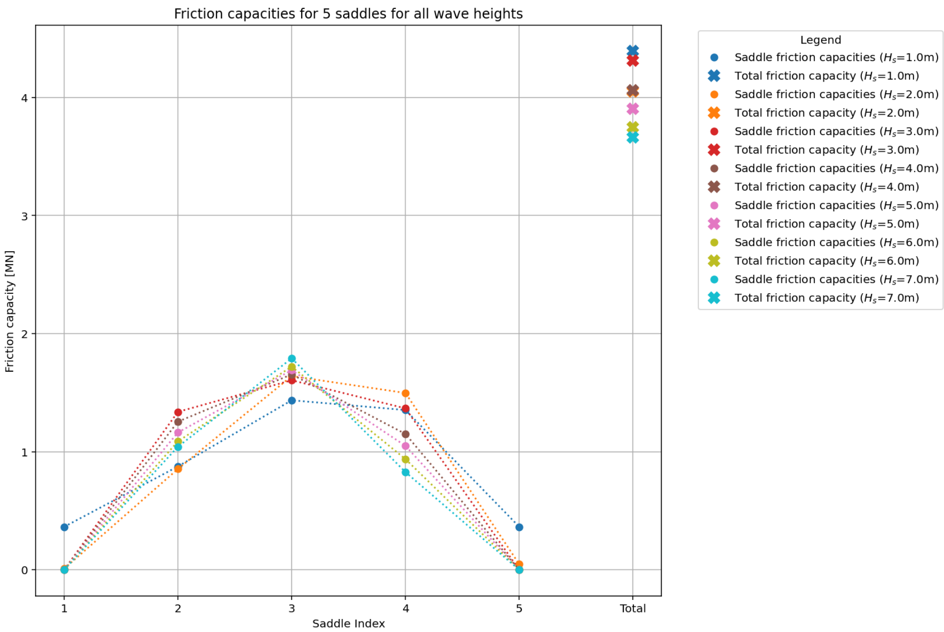

Figure E.3: Friction forces in 5 saddles

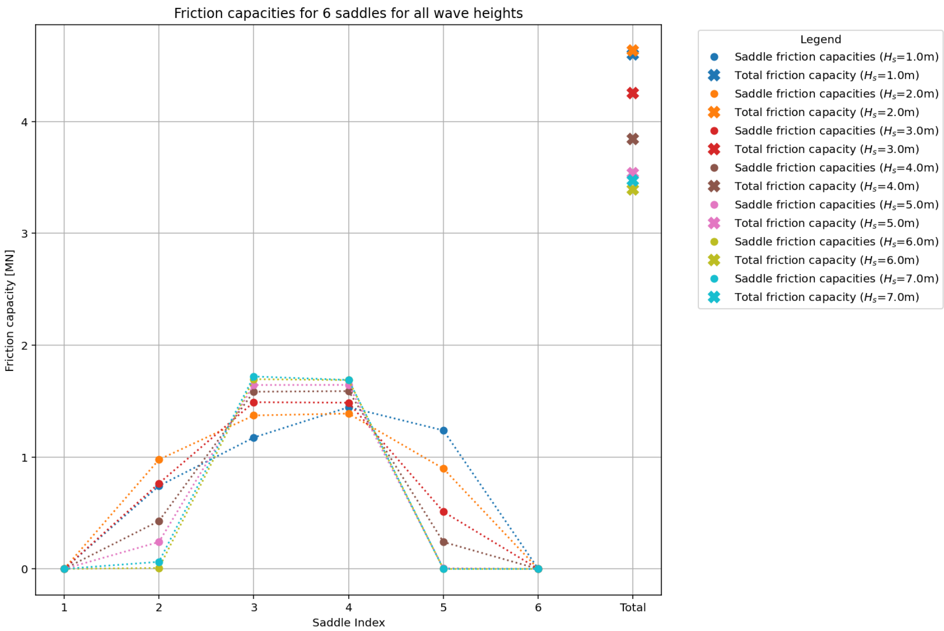

Figure E.4: Friction forces in 6 saddles

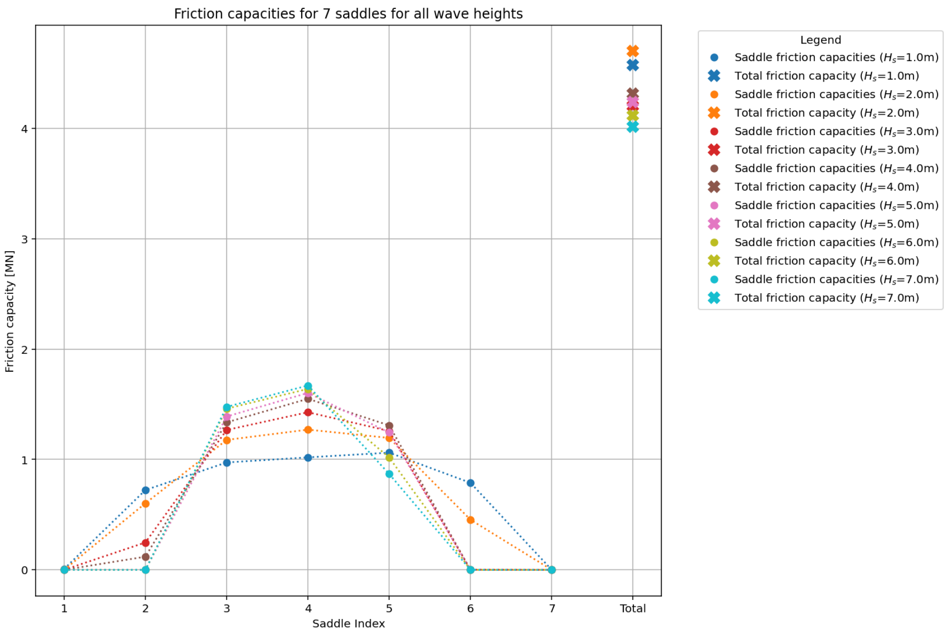

Figure E.5: Friction forces in 7 saddles

F

Appendix F: Additional research

This appendix contains the additional research results on the friction coefficient function.

F.1. Friction coefficient function

Regarding the friction topic, a recommendation is given for extending the test results to the saddle scale. It was recommended to investigate whether the friction capacity remains sufficient to prevent the longitudinal motion of the monopile when the friction function is simplified to a single friction coefficient for all normal forces.

This analysis started with a friction coefficient of 0.3 for all normal forces since this is the friction coefficient given by DNV-ST-N001 for rubber-steel friction in dry and wet conditions. However, it became clear that the total available friction capacity was lower than twice the required total seafastening design loads (2.78 MN < 3.0 MN); see figure F.1.

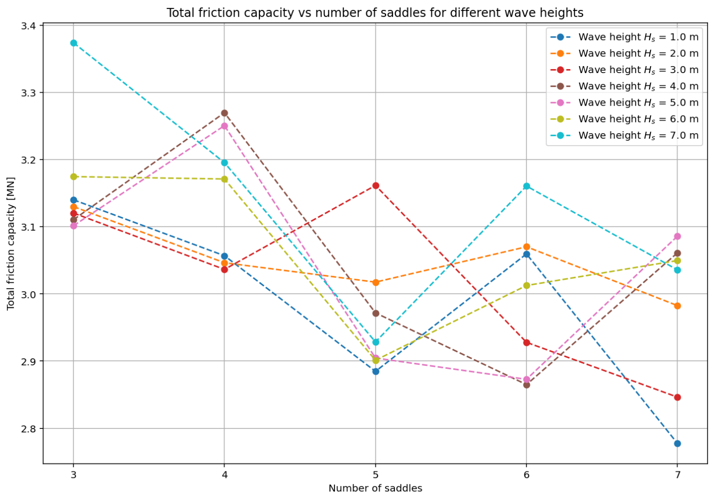

Figure F.1: Total friction capacity for $\mu = 0.3$

From this result, the friction coefficient is checked to determine when the total available friction capacity is at least twice the required seafastening design loads. This analysis showed that a friction coefficient of 0.33 meets this requirement for all cases; see figure F.2.

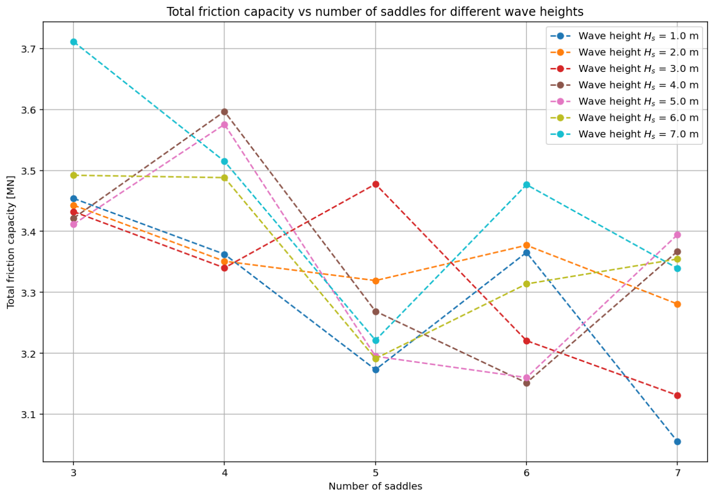

Figure F.2: Total friction capacity for $\mu = 0.33$

In addition, it is checked for which μ there is theoretically enough available friction capacity to prevent motion without applying lashing wires when the requirements of DNV are ignored. The results are shown in table F.1 and figure F.3. To prevent the motion of the monopile in the longitudinal direction for all wave heights and all saddle configurations, the minimum friction coefficient is 0.154. It should be noted that the position of the saddles was not checked with the deck construction during this analysis.

No. of saddles:	Friction coefficient:
3	0.134
4	0.142
5	0.154
6	0.143
7	0.149

Table F.1: Minimum friction coefficient to prevent longitudinal motion

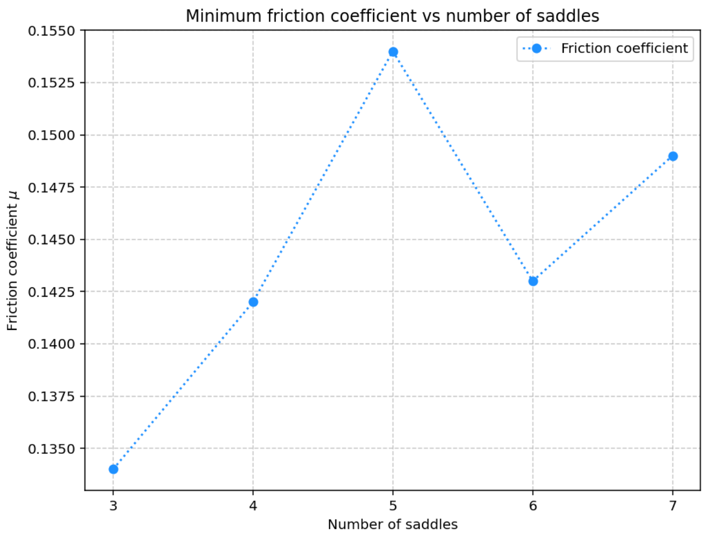

Figure F.3: Minimum friction coefficient for each saddle configuration

Figures F.4 to F.8 show the sub-friction forces in the saddles, the friction capacities per saddle and the resulting force of the external force and the opposing friction force for all saddle configurations. A wave height of 7.0 meters is selected since this results in the largest external force. All these figures are generated with the minimum friction coefficient of table F.1.

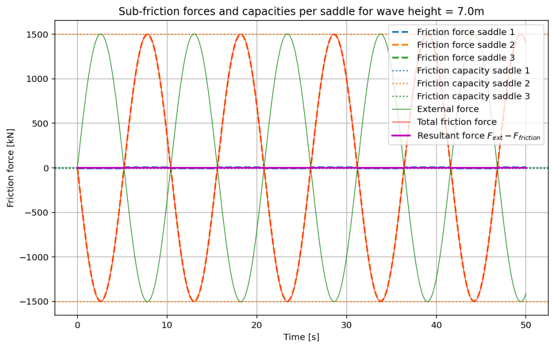

Figure F.4: Friction capacities 3 saddles

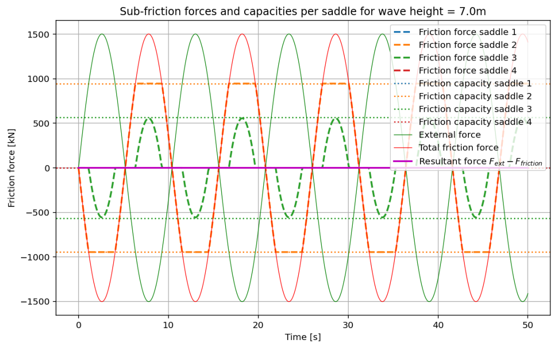

Figure F.5: Friction capacities 4 saddles

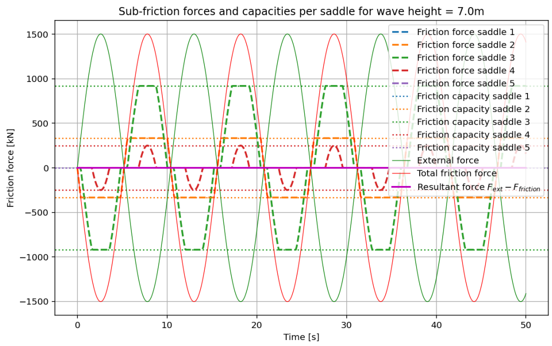

Figure F.6: Friction capacities 5 saddles

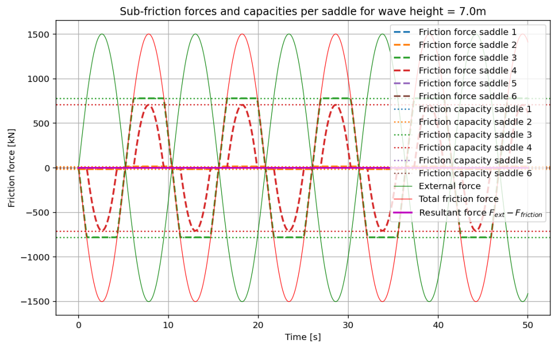

Figure F.7: Friction capacities 6 saddles

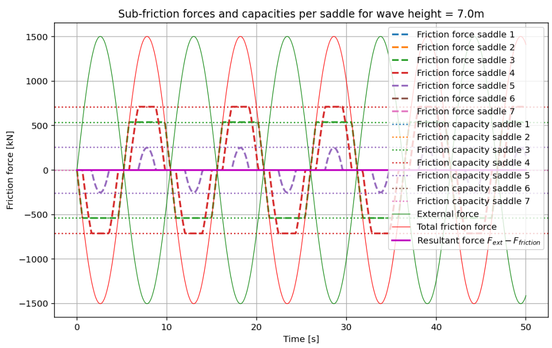

Figure F.8: Friction capacities 7 saddles

From this additional research, it can be concluded that a friction function with higher coefficients of friction for the lower normal forces and a decrease to 0.3 for higher normal forces is required to prevent longitudinal motion. Using a single value as the friction coefficient for all normal forces does not match reality, so question marks can be drawn by the friction coefficient as a single value that DNV provides.

DNV's value of 0.3 does not provide sufficient friction capacity to meet the requirements to sea-fasten the monopile friction-based; this is reached with friction coefficients above 0.33. Still, it is conservative as a friction coefficient between steel and rubber since the sliding friction tests showed higher friction coefficients.